Polymer-zirconia based ceramic composites produced by 3D-printing

Presented by Ľudmila Hodásová

Supervisors: Prof. Dr. Elaine Armelin and Prof. Gemma Fargas

Thesis submitted to obtain the degree of Doctor of Philosophy in Chemical Engineering at the Universitat Politècnica de Catalunya

Barcelona, 2022

Departament d'Enginyeria Química
and
Departament de Ciència i Enginyeria de Materials

Grup d'Innovació en Materials i Enginyeria Molecular
and
Centre d'Integritat Estructural, Fiabilitat i Micromecànica dels Materials

UNIVERSITAT POLITÈCNICA
DE CATALUNYA
UPC BARCELONATECH

IMEM

CIEFMA

Acknowledgments

I'd like to show my great gratitude to my supervisor Elaine Armelin Diggroc, for allowing me to be a part of the amazing IMEM team and grow in my professional career, for always being there, and for having great insights into my work. Also, for enormous help with finishing this thesis, which would be impossible without her help.

I'd like to extend my thanks to my other supervisor Gemma Fargas Ribas for supporting my exploration of the world of materials in the CIEFMA group. I appreciate all the opportunities in form of going to congresses and secondments abroad and for listening to my struggles even if they were not related to work.

I also would like to acknowledge Dr. Roberto Quintana from the Luxembourg Institute of Science and Technology (LIST), for a great collaboration and sharing the knowledge, which ended up being a successful project.

My next thank you goes to Prof. Tzanko Tzanov and A. Gala Morena from Molecular and Industrial Biotechnology Group (GMBI, UPC) for taking my research to the next step and for a great collaboration.

My gratitude goes to the Barcelona Research Center in Multiscale Science and Engineering for funding my research in the first 3 years of my Ph.D. studies and to Santander Scholarships for making my life easier in my final year.

After many years spent in the labs of IMEM and PSEP groups, I'd like to thank Dr. Luis Javier del Valle for always being patient and helpful, even when I didn't speak a word in Spanish. To Georgina and MariCruz I'd like to thank for making me love science as much as I do. Moreover, I can't imagine finishing my thesis without meeting and sharing my work and free time with Max, Hamidreza K., Anna, Guillem, Omid, Neudys, Angy, Didac, Julia, Helena, and Adrian. My special thanks go to all those people that I share my life with here, namely Hamidreza E. for being always helpful and for keeping the photo library always full, to Brenda for being a great listener and so much fun, to Raman master Jordi

for being always bringing fun together with Marc, to Samu and Agustina for always being the source of the most positive energy, to Sofia for being a safe harbor every time I needed it, to Matteo for being the best support in any life situation and making the best pasta around, and to Sonia for having the right answers for any question and the most important for kicking me out of the lab to finish this thesis.

Next, my greatest gratitude goes to Vitor for being the best quarantine mate, for always being so calm, and for keeping the rock'n'roll culture alive. To Ina, for being the greatest friend and support, endless game nights, keeping me sane, and just being there. I am thankful for both because from workmates to friends, they have become more than that, they have become family. I could not have done it without them.

I cannot start to express my thanks to MariCarmen, from explaining to me even the smallest details of dentistry, sorry stomatology, to listening to my every complaint, all the way to becoming like a sister to me at the Christmas table, together with memorable May 4th.

I would also like to thank my weekend crew, for being an amazing support and fan club throughout my Ph.D., namely Saša, Kika and Sergi, and Halle and William. Other thanks go to two people who set me in my academic career, Michal Jablonský and Aleš Ház. I'd like to thank my amazing cousin Filip Hodas, for making the most incredible cover for this thesis and for everything else we went through together.

With all my heart I'd love to thank my parents, Janka and Palo, for always supporting me, for giving me opportunities to study, for going with me through everything from hard exams to graduation celebrations, and for being also friends I turn to, even though I live abroad.

Other thanks go to my sister Siska, for always being the realist when I needed a sober point of view, for being a best friend throughout my academic

journey, and for just being her. And to Logan, for always being a rock and so understandable.

Finally, I would like to award the greatest thank you to my partner Filip, for being the greatest support, for never giving up on any challenge, for being anything I needed him to be every second of this journey, and for being so patient and always with a joke up his sleeve to make me laugh to make my day.

Abstract

Zirconia ceramic is widely used in numerous fields, such as electronics, machinery, energetic industry, and biomedical applications, due to its excellent properties such as chemical resistance, low conductivity at high temperatures, thermal stability, electrical resistance, toughness, hardness, but also inertness towards chemicals and good biocompatibility.

The 3D-printing technology has opened new doors for possible applications of zirconia and also allows for higher complexity of the shapes and structures, even for specimens with designed porosity, which would be until now unimaginable with traditional manufacturing methods like in the case of gel casting, a process where the ceramic particles are mixed with polymeric resin to obtain the product by the means of polymerization; or cold isostatic pressing, a mechanical process where the ceramic particles are compacted under pressure. The biocompatibility, inertness, and excellent aesthetic aspects of this ceramic make it also a preferred material for biomedical applications, more specifically in dentistry. However, application in the biomedical field has had some shortcomings, where the high hardness and brittleness of the material could cause discomfort or excessive wear. One of the aims of this thesis was to develop a new hybrid material that would complement the above-mentioned properties of zirconia and at the same time try to mimic the mechanical properties and biocompatibility of natural teeth using a combination of zirconia and acrylate polymer materials, while using additive manufacturing.

The first part of this study was focused on the development and manufacturing of such material. The idea of polymer-infiltrated ceramic networks (PICN), where a porous sintered ceramic structure is interpenetrated with a polymer matrix, was followed. The innovation of this technology was based on the 3D-printing of ceramic zirconia (3Y-TZP) scaffolds with designed porosity, thus, it could be controlled and adjusted according to the

requirements of the potential application. After the optimization of the printing process, the 50% zirconia infill was chosen as the most appropriate porosity of the scaffold that was subsequently infiltrated with bisphenol A glycerolate dimethacrylate (Bis-GMA) and triethylene glycol dimethacrylate (TEGDMA) copolymer.

After the successful manufacturing of 3D-printed PICN and the proper infiltration of the copolymer, the physical-chemistry properties of the new material were characterized, as well as its mechanical properties. The bacterial adhesion was evaluated against Gram-negative *Escherichia coli* and Gram-positive *Streptococcus salivarius* bacteria lines, revealing, that although such samples do not have antimicrobial properties, they do not promote excessive bacterial growth either. Regarding biocompatibility, the cell assay using human osteoblasts (MG-63) was carried out showing good cell viability.

To improve the antimicrobial properties of manufactured PICN, the surface was modified with the adhesion of silver nanoparticles, which were embedded in an enzymatically modified phenolated lignin matrix (Ag@PL NPs), obtained from renewable resources, to avoid metal particle oxidation. The functionalization of the surface of the ceramic-polymer hybrid material with such Ag NPs allowed the reduction of bacterial growth by 90% on the modified surface.

The last part of this thesis focused on the improvement of osseointegration of zirconia surface in vitro. Although it is an inert material, surface modification is required to avoid possible failures of zirconia once implanted in vivo. A polydopamine methacrylate copolymer, which also has proved antibiofilm formation properties, was applied to the surface of zirconia. Characterization of the modified surfaces has proven good viability of the MG-63 cell line and also a great adhesion of the polymeric nanofilm, produced by cold plasma to the surface of zirconia discs. This enhanced biocompatibility is attributed to the dopamine-derived polymer, a highly biocompatible material.

Overall, this thesis describes the 3D printing process of PICN structures, which have a macroporous structure for the correct infiltration of the copolymer that acts as an adhesion promoter. The synergy and good adhesion between these different materials have given rise to a prototype whose mechanical properties simulate those described for natural teeth. In addition, the modifications of the zirconia surface (flat or 3D-printed filaments structures) in order to improve the properties of the composite, have been satisfactory to deepen this research in the dental field, opening new ways to broaden the spectrum of applications of said hybrid materials in other biomedical fields.

Resumen

La zirconia es un material ampliamente utilizado en electrónica, en la industria energética y en la biomedicina debido a su estabilidad química, baja conductividad a altas temperaturas, excelente estabilidad térmica, resistencia eléctrica, dureza, alta tenacidad, y buena biocompatibilidad debido a su naturaleza inerte.

Con el desarrollo de la tecnología de fabricación aditiva (o *3D-printing*), se han propuesto nuevas aplicaciones para la zirconia hasta ahora inimagibles empleando métodos de producción convencionales, como es el caso del *gel casting*, proceso por el cual se mezclan las partículas cerámicas con una resina polimérica para obtención del producto tras la reacción de polimerización; o el prensado isostático en frío, que consiste en un proceso mecánico de compactación de las partículas cerámicas. Con la fabricación 3D se consiguen estructuras más complejas, con geometrías más variables y con un mayor control de la de porosidad. Estas características , a la par de su propiedad inerte y su excelente aspecto estético, convierten esta cerámica en uno de los materiales predilectos para aplicaciones biomédicas, especialmente en la odontología. No obstante, la dureza y fragilidad del material son dos limitaciones para su aplicación en la producción de biomateriales, debido a que pueden llevar al desgate de las estructuras y generar discomfort en el paciente. Uno de los objetivos de esta tesis fue el desarrollo por fabricación aditiva de nuevos materiales híbridos a base de zirconia y polímeros acrilatos para simular las propiedades mecánicas y la buena biocompatiblidad características de los dientes naturales.

La primera parte de esta tesis estuvo enfocada en el desarrollo de dichos materiales, con la elaboración de redes cerámicas infiltradas por polímeros (PICN, por sus siglas en inglés), en las cuales una estructura cerámica porosa sinterizada es interprenetada por una matriz de polímero. La innovación en este

proceso fue el diseño de andamios de zirconia cerámica (3Y-TZP), impresas tridimensionalmente por impresión 3D y con porosidad controlada y ajustada de acuerdo a los requerimientos condicionados por su potencial aplicación. Después de la optimización del proceso de impresión, se decidió trabajar con un porcentaje de relleno del 50 % de zirconia para obtener la porosidad adecuada de la matriz, la misma que fue después infiltrada con dimetacrilato de glicerolato de bisfenol A y trietilenglicol dimetacrilato (Bis-GMA y TEGDMA, por sus siglas en inglés, respectivamente).

Tras la producción de las estructuras PICN y la infiltración del copolímero, los materiales generados fueron completamente caracterizados por técnicas físico-químicas y las propiedades mecánicas fueron analizadas. Ensayos de adhesión bacteriana fueron llevados a cabo con las bacterias *Escherichia coli* (Gram-negativa) y *Stretoccocus salivarius* (Gram-positiva) concluyendo que, a pesar de la ausencia de efecto antibacteriano del material híbrido, tampoco existe una promoción del crecimiento bacteriano en dicha superficie. Respecto a la biocompatibilidad, experimentos con la línea celular osteoblástica humana MG-63 mostraron altos porcentajes de viabilidad celular.

Con el objetivo de mejorar las propiedades antimicrobianas de las PICN, la superficie fue modificada con nanopartículas de plata, las cuales fueron embebidas en una matriz de lignina modificada enzimáticamente con fenolatos provenientes de fuentes renovables (Ag@PL NPs) para evitar su oxidación. La funcionalización de la superficie del material híbrido cerámica-polímero con dichas nanopartículas permitió reducir el crecimiento bacteriano en un 90 %, respecto a la superficie no modificada.

La última parte de la tesis estuvo enfocada en realizar mejoras en la capacidad de oseointegración de la zirconia in vitro. Apesar de que es un material inerte, funcionalización de su superficie es recommendable para evitar futuros rechazos de la zirconia una vez implantada in vivo. Un copolímero de metacrilato de polidopamina, el cual también previene la formación de

biopelículas bacterianas, fue escogido para recubrir la superficie de zirconia. La caracterización de las estructuras modificadas demostró una gran adhesión del nuevo polímero, generado por plasma frío, a la superficie plana de discos de zirconia, además de una buena viabilidad de las células de la línea MG-63, en principio atribuída a la presencia de la polidopamina, un compuesto altamente biocompatible.

En conclusión, esta tesis describe el proceso de impresión 3D de estructuras PICN, las cuales tienen una estructura macroporosa para la correcta infiltración del copolímero que actúa como promotor de adherencia. La sinergia y la buena adherencia entre estos distintos materiales ha dado origen a un prototipo cuyas propiedades mecánicas simulan aquellas descritas para los dientes naturales. Además, las modificaciones de la superficie de la zirconia (plana o en format 3D filamentoso) con el fin de mejorar las propiedades del composite, ha resultado sactisfactoria para profundizar dicha investigación en el campo odontológico, permitiendo nuevas vías para ampliar el espectro de aplicaciones de dichos materiales híbridos en otros campos biomédicos.

List of Abbreviations

Abbreviation	Meaning
3Y-TZP	Yttria-stabilized zirconia polycrystal
AFM	Atomic force microscopy
Ag@PL NPs	Silver nanoparticles embedded in a phenolated lignin matrix
AM	Additive manufacturing
APDMES	3-amino- propyldimethylethoxy silane
ASTM	American society for testing and materials
ATCC	American type culture collection
ATR	Attenuated total reflection
BIC	Bone-to-implant contact
BIOMAT	An Open Innovation Test Bed for Nano-Enabled Bio-Based PUR Foams and Composites
Bis-DMA	Bisphenol A dimethacrylate
Bis-EMA	Ethoxylated bisphenol A glycol dimethacrylate
Bis-GMA	Bisphenol A glycerolate dimethacrylate
BJ-5ta	Human fibroblast
BPO	Benzoyl peroxide
CAD	Computer-aided design
CAM	Computer-aided manufacture
CFU	Colony-forming units
CLIP	Continuous liquid interface production
D3MA	1,10-decanediol dimethacrylate
DAPI	40 ,6-diamidino-2-phenylindole
DBD	Dielectric barrier discharge
DED	Direct energy deposition

DGEBA	Diglycidylether of bisphenol A
DIW	Direct ink writing
DLP	Direct light processing
DMEM	Dulbecco's modified Eagle's medium
DMLS	Direct metal laser sintering
DMP	Direct metal printing
DOMAm	Monomer methyl-DOPA methacrylamide
DP	Double power
DT	Double time
E	Young's modulus
EDX	Energy-dispersive X-ray
EGDMA	Ethylene glycol dimethacrylate
ERDF	European regional development fund
FBS	Fetal bovine serum
FDM	Fused deposition modeling
FFF	Fused filament fabrication
FSZ	Fully- stabilized zirconia
FTIR	Fourier-transform infrared spectroscopy
HA	Hydroxyapatite
HaCaT	Keratinocytes
HEMA	2- hydroxyethyl methacrylate
HV	Vickers hardness
HV5	Hardness
InLenw	Immersion lens detector
KIC	Fracture toughness
L-DOPA	3,4-dihydroxy-L-phenylalanine
LA-APPiP	Liquid-assisted atmospheric-pressure plasma-induced polymerization

LB	Luria-bertani
LbL	Layer-by-layer
LIST	Luxembourg Institute of Science and Technology
LSM	Laser scanning microscope
micro- CT	Microtomography
MTT	3-(4,5-dimethylthiazol-2-yl)-2,5-diphenyltetrazolium bromide
NB	Nutrient Broth
NiTi	Nickel-titanium
PBF	Powder bed fusion
PEEK	Sulfonated poly(ether-ether-ketone
PICN	Polymer-infiltrated ceramic networks
PLA	Polylactic acid
PMMA	Poly(methyl methacrylates)
PSZ	Partially-stabilized zirconia
Ra	Roughness average
ROP	Ring-opening polymerization
SE	Electrons detector
SEM	Scanning electron microscopy
SLA	Stereolithography
SLM	Selective laser melting
SLS	Selective laser sintering
SOFTAL	Sinusoidal electrical exci- tation
spinel	Mgal2o4
STL	Standard tessellation language format
TCD-DI-HEA	Bis(acryloyloxymethyl) tricyclo [5.2.1.02,6] decane
TCPs	Tissue culture plates
TEC	Thermal expansion coefficient

TEGDMA	Triethylene glycol dimethacrylate
TEM	Transmission electron microscopy
TZP	Tetragonal zirconia polycrystals
UDMA	Urethane dimethacrylate
Vitallium	Cobalt-chrome alloy composed of 65% Co, 30% Cr, and 5% Mo
VITO	Venturi-based nebulization system
WCA	Water contact angle
XPS	X-ray photoelectron spectroscopy
XRD	X-ray powder diffraction
YSZ	Yttrium-stabilized zirconia
γ-MPS	3-(trimethoxysilyl)propyl methacrylate

Table of Contents

List of figures

01

Introduction

1. Introduction

The first chapter discusses the state of the art of materials used, as well as processes to obtain our final product, polymer-infiltrated ceramic networks (PICN). First, the base material, 3 mol% yttria-stabilized zirconia polycrystal (3Y-TZP), is characterized. Summing the development of the material, basic mechanical and chemical properties, and also recent advances in additive manufacturing of ceramic materials are described. This is followed by a brief description of various additive manufacturing techniques and their applications, whereas direct ink writing (DIW), as the main method used in this work, is described in more detail in further sections. Acrylate polymers and their polymerization are described and characterized as materials for use in dental applications. In the present thesis, bisphenol A glycerolate dimethacrylate (Bis-GMA) and triethylene glycol dimethacrylate (TEGDMA) acrylate copolymer was chosen for use. Then, they will be approached in deeper detail in this introduction section. The final part discusses the combination of these materials to produce polymer-infiltrated ceramic networks (PICN), which are porous, produced by additive manufacturing and designed to allow the infiltration with the above-mentioned copolymer.

As part of this thesis was based on collaborations, another acrylate-based copolymer (ethylene glycol dimethacrylate, EGDMA) was used in Chapter 6. However, as it was developed and extensively characterized by Plasma Process Engineering Group (Luxembourg Institute of Science and Technology, LIST), the properties description can be found in the corresponding chapter.

1.1   Zirconia-based ceramics

Zirconia dioxide (ZrO_2), also more commonly known as zirconia, was discovered by German chemist Martin Heinrich Klaproth in 1789. He classified it as crystalline ceramic material and it can be found in nature as baddeleyite, a monoclinic translucent mineral [1].

Zirconia is stable at room temperature in its monoclinic phase (*m*) up to 1170 °C when it changes to the tetragonal phase (*t*), followed by cubic phase (*c*) in the range of 2370 °C to 2680 °C [2]. Different phases are shown in Figure 1-1. Tetragonal to monoclinic transformation is reversible, athermal, and diffusionless, and it includes 4% volume expansion, which can cause cracking due to the internal stress of the material. Those were the limitations of potential applications of zirconia as a pure material [3], [4].
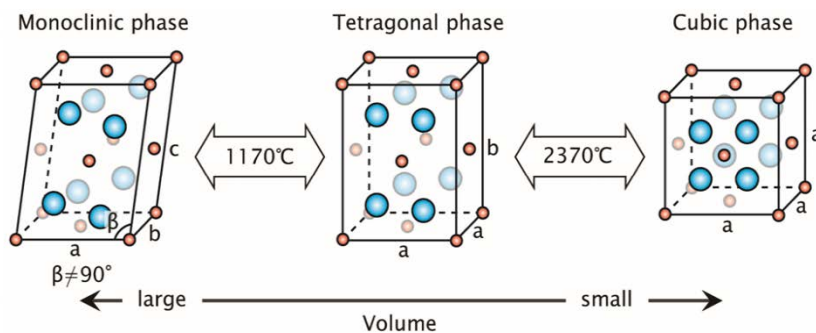
Figure 1-1: Different zirconia polymorphic phases and their crystalline structures [127]

Decades later, stabilization of pure zirconia in its cubic phase at lower temperatures was achieved by adding various oxides, such as Y_2O_3, CeO_2, SrO, La_2O_3, CaO, or MgO [4]. Complete stabilization of the cubic phase at room temperature was achieved by adding excessive amounts (16 to 30 mol%) of magnesia (MgO) or calcia (CaO) and this material is commonly known as fully-stabilized zirconia (FSZ) [5]. This type of zirconia, formed by large cubic grains, is used for its heat stability as solid electrolytes, heat exchangers, or fuel cells. Single FSZ crystals are used as diamond substitutes in the jewelry industry [6].

Further observation of the calcia and magnesia-stabilized cubic zirconia lead Garvie *et al*. [7] to a conclusion that mechanical properties are improved if nanometric monoclinic or tetragonal precipitates are included. The strength of the material was significantly improved if the tetragonal precipitates were included due to the t to m transformation which includes an increase in volume and therefore closes the crack tip before potential propagation through the material. This type of zirconia is classified as partially-stabilized zirconia (PSZ) [7], [8]. It has applications in numerous fields, such as the automotive industry, where it is used to monitor air-fuel-ratio in cars. It is also very often used to measure a wide range of temperatures or their rapid change [9].

In the second half of the 1970s first PSZ containing only a tetragonal phase was produced and characterized by Rieth *et al.* [10] and Gupta *et al.* [11], this modification was named tetragonal zirconia polycrystals (TZP). The stabilization of TZP is provided by yttrium oxide (Y_2O_3) [10], [11]. This modification is also an objective of this work and will be further discussed and characterized, as it is a material with excellent mechanical properties, chemical inertness, and biocompatibility. Stabilization of zirconia with Y_2O_3 can be observed in Figure 1-2.
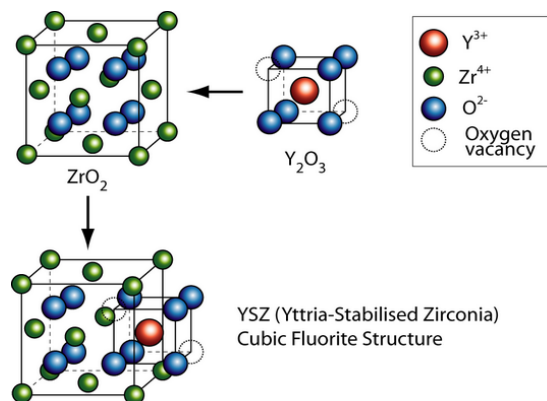
Figure 1-2: Stabilization of zirconia with Y_2O_3 [128]

As high-temperature phases of pure zirconia are preferred due to their properties, doping with aliovalent ions is required to keep those phases stable at room temperature. There are two main approaches to stabilizing zirconia:

1. by creating oxygen vacancies using doping with oversized trivalent ions, like Y^{3+}

2. by stabilization of cation network using undersized trivalent ions, or tetravalent ions, such as Ce^{4+} [4], [12]

As this work is focused on yttria-stabilized zirconia, more information about lather stabilization can be found elsewhere [12]–[14]. The stabilization with yttria stands on substituting very small Zr^{4+} ions with slightly bigger Y^{3+} ions to reduce oxygen overcrowding and introduce oxygen vacancies in order to maintain a neutral charge (Figure 1-2). For every two yttrium ions, one vacancy is created. Lower valence Y_2O_3 together with oxygen vacancies disfavor monoclinic phase to more symmetric tetragonal and cubic phases. The amount of dopant affects the transformation phase starting from tetragonal and moving to cubic, where the minimum amount of yttria to achieve cubic phase is 8 mol% [15]. This understanding of zirconia stabilization is based on Kröger-Vink notation [16], as we mentioned above, the tetragonal phase can be also stabilized by smaller cations (Fe^{3+}, Al^{3+}, and Ga^{3+}) with higher valences, which would require different notations, to explain the mechanism of stabilization [12]. Zirconia doping with yttria is based on a phase diagram (Figure 1-3), which has been modified multiple times in history, as the transformations need a long time to reach homogeneity of the material. At a sintering temperature of 1500 °C, it can be weeks before equilibrium is achieved. As reported elsewhere the diagram in Figure 1-3 was developed by Scott in 1975 [17].
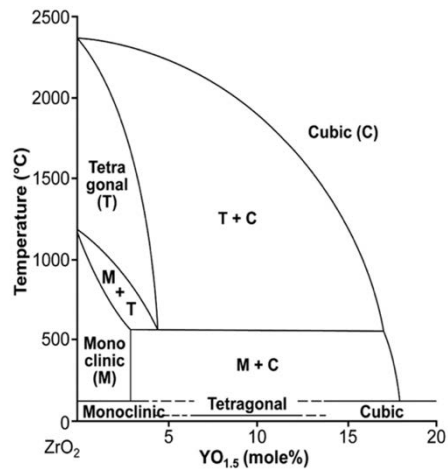
Figure 1-4: Phase diagram developed by Scott [17]

As can be seen in Figure 1-4, during the crack forming, the tetragonal phase under stress converts to the monoclinic phase, which is accompanied by ∼4% volume expansion. This phenomenon, also known as transformation toughening, causes closure of the tip of the crack and stops its further propagation. The volume expansion causes compressive stress at the tip of the crack; therefore, more energy is required for the crack expansion.
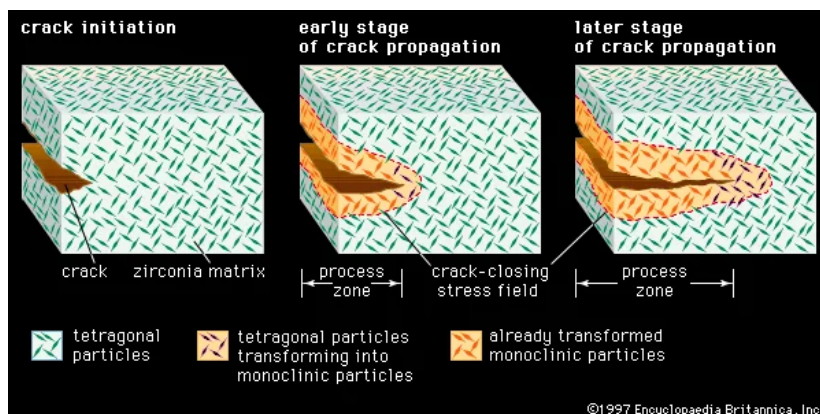
Figure 1-3: Crack propagation and transformation toughening of Y-TZP [129]

This is a very important parameter for ceramic fracture toughness, as the energy associated with crack propagation spreads throughout the material and therefore increases the overall toughness of the Y-TZP [18].

Mechanical properties of zirconia depend on the grain size, where spontaneous *t-m* transformation can occur if the critical size is overcome. Whereas, below a grain size of 0.2 μm the transformation is not possible, resulting in a reduction of fracture toughness. As the grain size is determined by the sintering process, it plays a key role in the final mechanical properties of zirconia [19]. A summary of the properties of commercially available 3Y-TZP can be found in Table 1-1.

Table 1-1: Properties of 3Y-TZP [20]

Specification	Value
Density (ρ)	6.05 g/cm^3
Thermal expansion coefficient (TEC)	10×10^{-6} K^{-1}
Flexural strength	1200 MPa
Fracture toughness (KIC)	8MN/m$^{(1/2)}$
Young's modulus (E)	210 GPa
Vickers hardness (HV 10)	1200 HV
Melting point	2680 °C
Shrinkage after sintering	20.8 %

All the above-mentioned properties make zirconia a suitable material for multidisciplinary applications in hostile environments. The thermal and electrical resistance makes it suitable for electronics, but other industrial uses

also include corrosion and heat-resistant parts, valves, cutting tools, oxygen sensors, various coatings, wear-resistant components, and solid electrolytes in fuel cells, among others [21].

A newer field, which started emerging in the 1960s is biomedical applications of zirconia, especially 3 mol% Y-TZP, for its high biocompatibility and improved fracture toughness compared to other ceramic compounds. The most common application of zirconia in the biomedical field is the manufacturing of ball heads for total hip replacement or total hip arthroplasty [18]. It replaced previously used alumina because due to the improved properties the ball heads could be smaller and easily implanted in comparison with alumina. Even though, its use for hip replacement has been postponed due to the numerous failures of these ball heads [22], [23].

In dentistry, pure zirconia was not widely used until the 1990s, but with a still stronger position of computer-aided design and computer-aided manufacturing (CAD/CAM), it was introduced as a suitable material. The production still mostly stands on subtracting methods, where based on the CAD model, the desired implant is cut out from a block of material. Medical grade 3Y-TZP is used in dentistry, due to its aesthetics and easy color modifications, to manufacture dental implants, crowns, or bridges [19] It is very chemically stable, so it protects surrounding tissues from any release of toxic materials, it also supports osseointegration and some studies state a reduction of biofilm to the surface, therefore avoiding rejection of the implant or inflammations. With these results and osseointegration index in the same ratio as titanium implants, zirconia-based materials have an advantage of a tooth-like appearance, which makes them preferable for implantation [24].

Although zirconia is widely accepted as a dental material, its mechanical properties are nowhere close to natural dentin. An important parameter representing these differences is Young's modulus, where for natural dentin it

varies between 10-30 GPa, but for zirconia, it is roughly 10 times more (~200 GPa) [20], [25] Vicker's hardness of zirconia also surpasses one of natural teeth, the hardness of enamel varies from 250 HV to 380 HV and for dentin it is only ~50 HV, whereas the hardness of zirconia ceramic is ~1200 HV [25], [26]. These differences can cause an early failure of implants and are a reason behind the wear of surrounding natural teeth. These limitations have been a challenge for the current market and the development of new and modern materials for dental applications [27].

1.2   Additive manufacturing

American society for testing and materials (ASTM) defines additive manufacturing (AM) as "a process of joining materials to make objects from 3D model data, usually layer upon layer, as opposed to subtractive manufacturing methodologies." This manufacturing technique, also known as 3D-printing, is usually based on computer-aided design (CAD), which is later sliced into layers by suitable software and introduced to a 3D printer to proceed to computer-aided manufacture (CAM) [28]. Layer-by-layer production allows for the creation of complex shapes and significantly reduces material waste in comparison with more traditional subtractive manufacturing, where the desired shape based on the CAD model is cut from a block of material [29].

Many believe that with the development of additive manufacturing we have entered a new stage of industrial revolutions, also that AM can surpass traditional ways of manufacturing and its challenges and keep up with the fast development of the current generation [30].

The first patent for the 3D-printing machine was registered by Charles W. Hull on August 8th, 1984 [31], although it was called an *Apparatus for the production of three-dimensional objects by stereolithography* [29]. His idea

came from long production times of prototypes, and he continued to obtain multiple patents related to additive manufacturing, including one for standard tessellation language format (STL), which connects the CAD with the 3D printer [32]. Since then, additive manufacturing went through numerous transformations and many new types of printers have been developed, with stereolithography being still the most used technique [33]. In 1992 Scott Crump [34] patented the fused deposition modeling and the world was set for a manufacturing revolution, as commented previously. But it wasn't until 1993 that the "3D-printer", which was able to print plastic, metal, and ceramic parts, was patented by two professors from the Massachusetts Institute of Technology, Michael Cima and Emanuel Sachs [35]. Nowadays, additive manufacturing occupies numerous fields including anything from the automotive industry to living human tissue [32].

Additive manufacturing production techniques can be categorized based on the type of curing, and deposition of the type of material used. Constantly new approaches to AM are being developed and new combinations of techniques are being investigated.

The main categories of additive manufacturing are:

1.   Vat polymerization

This category is based on selective curing of photopolymer resins, usually with UV light. The manufactured part is submerged in a tank with liquid resin, and the light is selectively directed through it, curing one layer at a time. Vat polymerization includes multiple printing techniques, but 3 most commonly used are (i) stereolithography (SLA), which uses a single beam light source; (ii) direct light processing (DLP), which is based on a digital projection of the entire layer; and (iii) continuous liquid interface production (CLIP), what is similar as

DLP, but in addition, the whole platform moves continuously, what makes the printing process faster than the other two techniques [36], [37].

2.   Material extrusion

This category can be divided into two smaller categories:

a) Filament based, where already prepared polymer filament is remelted to be extruded in the desired shape and then it rapidly solidifies. These 3D printers are commercially available at low prices and are also a popular choice for home or small companies. The technical term for filament-based additive manufacturing is fused deposition modeling (FDM), or it can also be found as fused filament fabrication (FFF) [36], [38].

b) Direct ink writing (DIW), where the "ink", usually is in a paste-like composition and is extruded through a nozzle under pressure [36]. This technique will be further discussed in Section 1.2.1, as it was used as a manufacturing method in this thesis.

3.   Powder bed fusion (PBF)

In PBF powders are melted or sintered selectively using an energy source to produce parts. After sintering one layer, the next layer of powder is evenly distributed over the powder bed and a new layer is sintered. The unsintered material is used as a support for the printed piece. These 3 techniques are the most common in the PBF category: (i) selective laser sintering (SLS), which is used for plastic; (ii) direct metal laser sintering (DMLS), used for metals, including alloys; and (iii) selective laser melting (SLM), which is also used for metals, but as it also melts and sinters the metal material, only single metals can be used [36], [39].

4. Material jetting

Printed parts are produced by deposition of droplets of liquid material on the printing bed and subsequently followed by curing with heat or UV light. This process allows multiple materials, including photopolymers, waxes, metals, and ceramics [36], [40].

5. Binder jetting

Binder jetting manufacturing is a combination of PBF and material jetting, the powdered material is deposited in a single layer on the printing bed and then the liquid binder is deposited in the places of curing. This method is mostly used for sands, ceramics, and metals [36], [40].

6. Direct energy deposition (DED)

This technology, also known as direct metal deposition, works similarly to FDM, but with metal materials. Metal in the form of powder or wire is melted in the printer head, either with a laser beam or with an electron beam, and then extruded and cooled [36], [41].

7. Sheet lamination

Layers of the manufactured piece are stacked together and then cut to the shape or sheets of the material are first cut to the shape and then stacked. It was originally developed for paper models in architecture, but nowadays it can be used in a variety of materials, even metals [36], [42].

More detailed information and other printing techniques including materials used, including ceramics [43], [44], for each individual technology can be seen in Figure 1-5. For an easier understanding of the figure, the abbreviations used are listed in the Table 1-2.
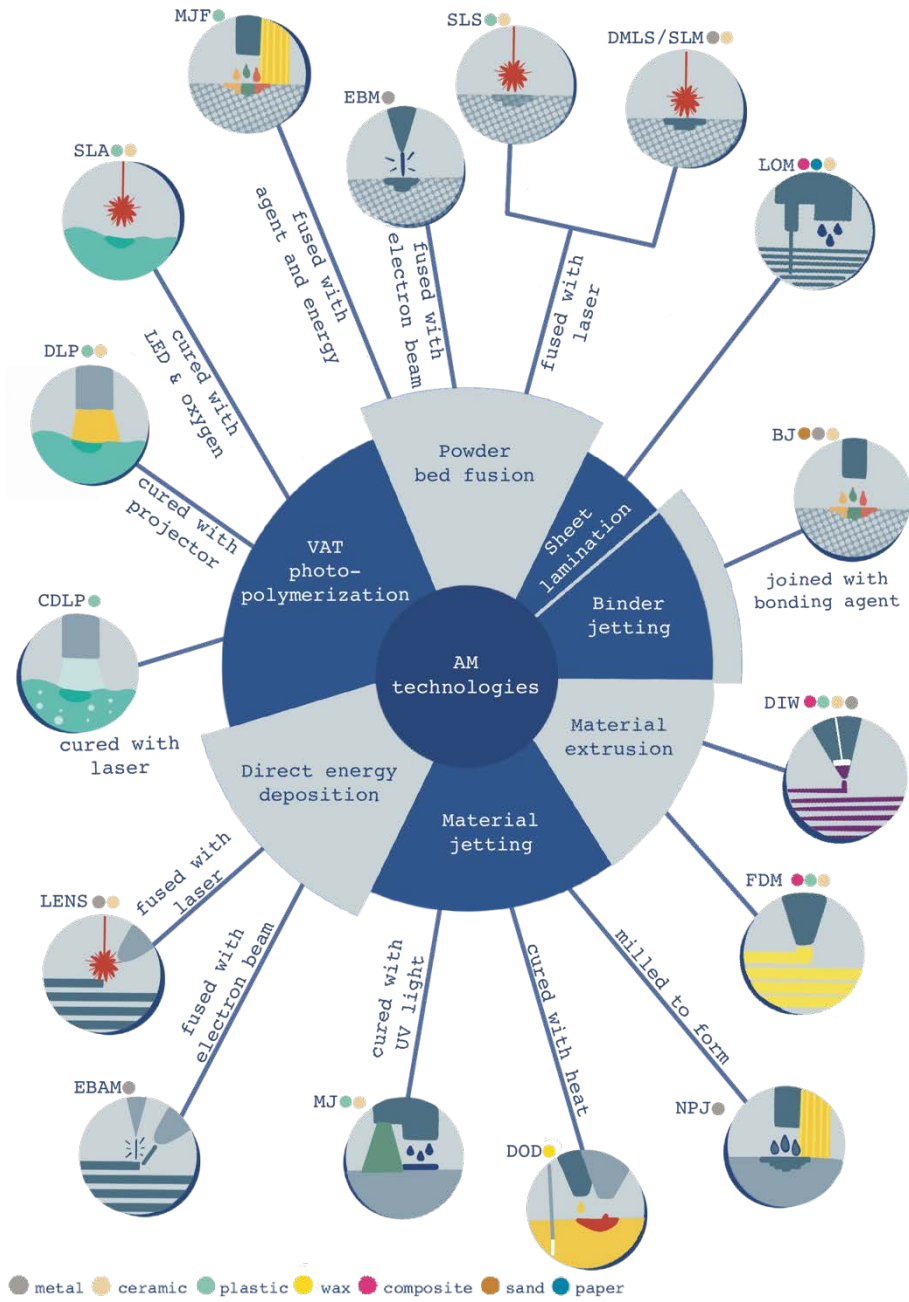
Figure 1-5: Classification of AM technologies. Adapted from reference [36]

Table 1-2: Abbreviations of AM technologies from Figure 1-5

Abbreviation	AM technology	Abbreviation	AM technology
SLA	Stereolithography	MJF	Multi Jet Fusion
DLP	Digital Light Processing	SLS	Selective Laser Sintering
CDLP	Continous Digital Light Processing	DMLS/SLM	Direct Metal Laser Sintering / Selective Laser Melting
FDM	Fused Deposition Modeling	EBM	Electron Beam Melting
MJ	Material Jetting	LENS	Laser Engineering Net Shape
NPJ	NanoParticle Jetting	EBAM	Electron Beam Additive Manufacturing
DOD	Drop On Demand	LOM	Laminated Object Manufacturing
BJ	Binder Jetting		

1.2.1 Direct ink writing (DIW)

As it was mentioned previously, direct ink writing has an extended explanation here since this technique was the manufacturing method used in this study. Direct ink writing belongs to the material extrusion category of additive manufacturing, and it is one of the most versatile from a wide range of techniques. It is thanks to a wide variety of materials that can be used for manufacture, as long as they have required rheological behavior during extrusion. As described above in DIW the material in a viscoelastic form is extruded through a nozzle based on a computer model in a layer-by-layer fashion. It was first patented in 1997 by Cesarano and Calvert [45] as a printer for complex ceramic scaffolds, since then polymers, glass, metals, or cements have been used. It can be easily modified to the requirements of the material and therefore it is having a great potential for developing new materials for the additive manufacturing industry [30]. The typical process of DIW includes a CAD model of the desired structure, which is sliced with slicing software to create a

layer-by-layer model, and then the extrusion itself. The model of a typical DIW printer can be seen in Figure 1-6.

The printing quality is limited by nozzle diameter, printing speed, and pressure of extrusion. The smaller diameters can provide a higher resolution of printed pieces, but that also requires higher extrusion pressure and slower printing time to avoid clogging the nozzle or tearing the extruded filaments. One of the great advantages of the DIW is its unique ability to print continuous filaments at room temperature, therefore the printability of the ink is mostly dependent on the rheology of the printed material. The printability can be also adjusted with printing speed, usually 5-50 mm/s, or with extrusion pressure [30]. After the deposition, the scaffolds can be solidified either by drying on air, or other external processes can be involved. For example, in the case of ceramic materials, the printing process is normally followed by the drying process and then the printed parts are sintered at high temperatures.
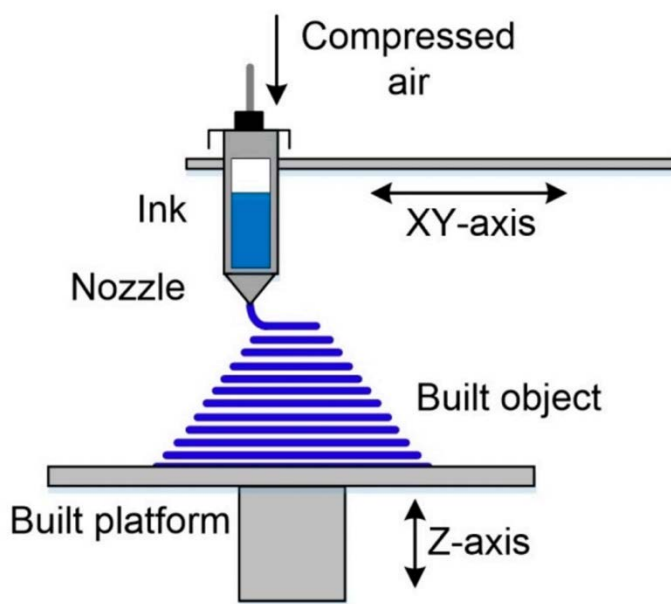
Figure 1-6: Direct ink writing assembly [130]

1.2.2 Additive manufacturing of ceramic materials

Ceramics, which are represented mostly by nitrides, carbides, and oxides are high-demand materials due to their excellent properties such as high strength, resistance to corrosion, electrical insulation properties, thermal stability, inertness, and biocompatibility. These properties ensure their application in almost all industrial fields, such as aerospace, automotive, and energetic industries, and they are also a favorable material for the biomedical field [41]. However, their brittleness and high hardness are often a challenge for shaping already sintered components, this type of processing introduces microcracks and defects. Another disadvantage of machine processing is the high cost, as they need to be shaped by diamond. Estimates say it could represent up to 70% of production costs [44], [46]. Many of their applications require complex shapes and fast manufacturing, which is a challenge for traditional methods of production. Methods like gel casting, injection molding, cold isostatic pressing, and others are all based on molds, where either dry method (powder mix is directly shaped in the mold), or wet approach, powder mix is mixed with a liquid carrier and then shaped into a mold. Therefore, the final shapes depend on the limitations of the molds. Additive manufacturing can be a solution to complex shapes, such as porous structures, pieces with hollow spaces (macro-pores), or microscale pieces [30], [44], [47], [48].

There are two main types of additive manufacturing of ceramics, either with required post-processing, or direct sintering of pieces during manufacturing. In the case of a single-step process, the powder base is directly sintered during the manufacturing process and no further processing, except surface finishes, is required. Multistep production is based on printing the green body, which is usually produced from the polymer-based paste and needs to be sintered

separately [44]. The majority of AM technologies for ceramics belong to multistep production. However, Juste et al. [49] developed an SLM technique to produce ceramic parts in one step and DED was explored and successfully executed [43], [49]. Multistep AM techniques include many of those mentioned at the beginning of this section, namely photopolymerization techniques, binder jetting, extrusion techniques, fused deposition, and direct ink writing [44], [50]. Recent development in new printing machines and extensive research on material modifications have improved the previous challenge of the achievement of high-density specimens, where densities over 96% have been reached by multiple researchers [21], [50], [51].

The main objective of this work is the development of new zirconia-based composite material for the biomedical field, particularly for dental applications. As this area requires high-end customization of products, AM is becoming a go-to manufacturing process, as the final product can be based on real data from a patient. Even though there still are many challenges in the AM processes including surface quality, resolution and dimensional accuracy, and shrinkage of the specimen [41]. A list of recently successful manufacturing methods for zirconia-based final products applied in dentistry can be found in Table 1-3.

Table 1-3: Different dental restoration specimens produced by additive manufacturing from zirconia. The table has been adapted from the following reference [52].

AM Technology	Application	Reference
Direct Inkjet printing	Dental crown	[53]
	Dental bridge framework	[54]
Direct light processing	Root analogue implants	[55]
	Dental implant	[56]
	Dental bridges	[57]
Stereolithography	Dental crown	[58]–[61]
	Implant-supported AM crown	[62]
	Dental implant	[63]
Lithography-based process	Occlusal veneers	[64]

1.3   Polymeric materials

Before the discovery and development of synthetic polymers, such as acrylates, natural sources were modified and used as plastic materials. The first example of such materials were horns and hoofs of animals, and it was found that if these were heated, they could be molted in different shapes and that they hardened back to their original state after cooling. Another example of natural polymeric materials is shellac, which is still widely used today [65]. The current applications include numerous surface protective formulations, adhesives, cosmetics, and applications in the pharmaceutical industry and also

electrical industry, more detailed information about properties and future aspects can be found in the following reference [66]. It is a natural resin produced by insects (*Coccus Lacca*), which infest fig trees. It was used for more than a thousand years in India before it was described in the scientific work of John Huyglen von Linschoeten in 1596 [67]. The first applications included protective wood and metal coatings, but later it was also used as phonograph discs [68].

In 1735 natural rubber was developed in France from a resin from South American trees (*Hevea brasiliensis*). It has a polyisoprene structure and was primarily used as an eraser for pencils. With further study of natural rubber and incorporation of solvents into the production ways, rubber could be molded into various shapes. However, the mechanical properties did not allow for multiuse in many areas. Over a century later (1844), Dr. Charles Goodyear Jr. discovered that the properties of such natural rubber were significantly improved after the addition of sulfur [69]. The new material was still flexible, but the glass transition was significantly lower. Added sulfur bonded with unreacted carbon-to-carbon double bonds and based on the added amount, the flexibility and hardness can be managed to desired values. This process still used today was named vulcanization. With further development of manufacturing processes in the 19th century, such as extruding, pressing, and shape molding, vulcanized rubber revolutionized the production of day-to-day products [68].

As this work focuses on materials used in stomatology, another historically significant natural polymer that should be mentioned is gutta-percha, also known as a corallite. It is a natural polymer with a structure very similar to that of natural rubber, with the only difference being a trans conformation instead of the cis conformation of natural rubber (Figure 1-7). Small differences on the molecular level project themselves significantly in the means of physical properties. Gutta-percha in comparison with natural rubber is hard and tough

and has a high melting point and low flexibility. This thermoplastic polymer was first introduced to the western world by Dr. W. Montomerie and it was soon applied to multiple areas and improved with various additives. One of the interesting applications includes the insolation of the first underwater communications cables, where this polymer was used until the development of polyethylene at the beginning of the 20th century. For this work, a far more interesting application of gutta-percha was its application as a temporary filling material for emergencies in dentistry. Temporary crowns were also prepared, but the most widely used application was, and still is used, endodontic root canal filling [68].
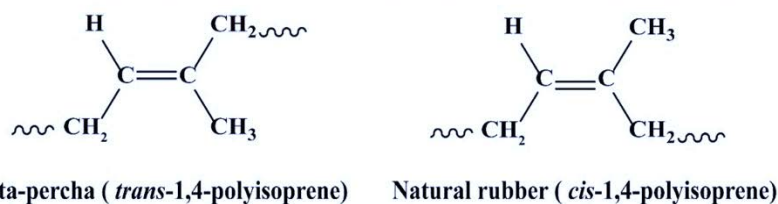
Figure 1-7: Gutta-percha and natural rubber molecules [131]

The first half of the 20th century brought the world well-known polymers such as Bakelite, polystyrene, polyvinyl chloride, urea formaldehyde, polyester, nylon, epoxy resins, and many more [70]. This development was driven by a desire to find a synthetic replacement for natural rubber. This period, also sometimes referred to as the age of thermoplastics, was the time when the principles of polymerization were discovered. In 1920, Dr. Herman Staudinger referred to "macromolecules" in relationship with polymers [71], [72]. One hundred years after, Staudinger is still recognized as the father of polymer chemistry. The first synthetic fiber polymer nylon was patented in 1937 by Carothers [73] since then the development of new polymers accelerated.

As there is a great number of different types of polymers, some basic classification is required. Figure 1-8 shows the main characteristics of how the

polymers can be divided into groups. Based on the source the polymers can be divided into natural, synthetic, and semi-synthetic, the type of polymerization process divides the entire population into two groups, polymerization by addition, where monomer molecules react together to form a polymer chain with no side product of the reaction, whereas during condensation reaction monomers are linked together with the formation of side products, usually in the form of small molecules, such as H_2O, HCl or ammonia. However, other authors consider ring-opening polymerization (ROP) as another class of growth polymerization process. Ring-opening polymerization is a reaction where cyclic monomers after initiation break the ring and form a linear structure, with the exception of 6-membered rings [74]. Another important classification is the one based on the microstructure homogeneity of polymer chains, which will be different depending on the arrangement of the monomers or on the different polymer mixture compositions. A homopolymer is a polymer made from many copies of a single repeating unit, whereas copolymers are made of two or more different monomers, which are alternating in the structure [74], [75]. For example, acrylate polymers in many cases are built as copolymers to ease manipulation and obtain the required properties [76]. Another strategy that is extensively employed in plastic technology is to combine different polymer matrices to obtain a new polymer, which is called blend. The proportion of each polymer will play an important role in the final properties of the blend material.

Molecular forces	Sources of origin	Polymerization Process
Elastomers Thermoplastics Thermosets Fibres	Natural Synthetic Semi synthetic	Addition Condensation

Classification of polymers

Growth Polymerization	Homogeneity of polymers	Structure
Ring opening Chain growth Step growth	Homopolymers Copolymers Blends	Linear Branched Cross—linked (network)

Figure 1-8: Classification of polymers. Adapted from references [70], [74]*.*

Developing new polymers is an active field of research, and discoveries are made daily. The application of new materials in dentistry has always been closely linked to the development of new technologies. There has always been a demand for better, easy-to-use materials with superior mechanical and aesthetical properties, including high biocompatibility. Since its discovery, the usage of resin materials in dentistry has been exponential [68]. As this work focuses on acrylate polymers in dentistry, the following part will only include those polymers relevant to this research.

1.3.1. Acrylate polymers

Acrylic polymers, produced from acrylic acid were not discovered until 1901, even though acrylic acid and its derivates were known and characterized decades earlier. The first to produce clear, solid polymers of this acid was Dr. Otto Röhm, and since then a great variety of acrylate polymers were manufactured. By the 1930s poly(methyl acrylates) emerged, used as a safety

glasses, followed by poly(methyl methacrylates) (PMMA), which were harder and are commonly known as Plexiglas[TM]. By the end of the decade, those polymers were commercially available in the form of powders and used for fabric finishes, coatings, and acrylic-based paints. The acrylic polymers are made of polymers and copolymers of acrylic and methacrylic acids, their esters, acrylonitriles, and acryl amides [68], [74]. So, acrylate polymers like PMMA can be considered structurally as derivatives of acrylic acid.

All the above-mentioned acrylic monomers contain a characteristic vinyl group, which appears on the terminal end of the monomers (Figure 1-9). Characteristic is an unsaturated carbon-to-carbon double bond with three hydrogens and one bond available for substitution at the alpha carbon. For acrylates, this group is occupied by carboxylic acid and the starting material, called acrylic acid is created. For further functionalization, the hydrogen of the acid group is substituted. For example, if substituted with a methyl group, the methyl methacrylate monomer is created. Other examples of such substitution are ethyl methacrylate, hydroxyethyl methacrylate, t-butyl methacrylate, or n-butyl methacrylate [68].
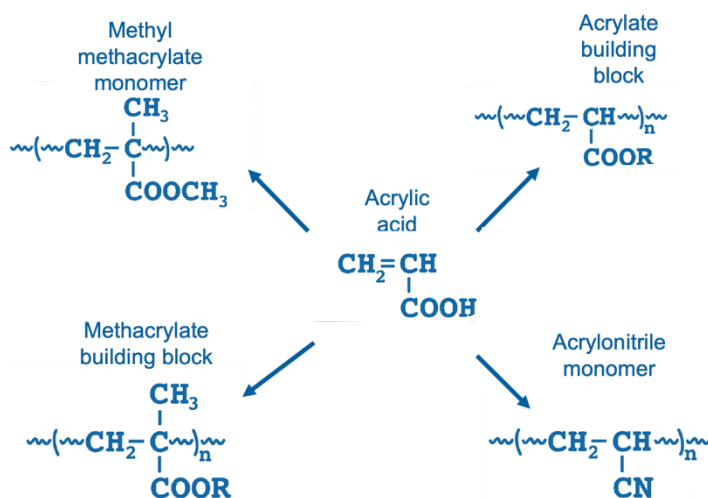
Figure 1-9: Monomers derived from acrylic acid. Adapted from reference [132]

1.3.2. Acrylate polymers in dentistry

The first acrylate polymer valuable for dental applications was poly(methyl methacrylate) (PMMA) processed by heat. It was a great hit in inlays, crowns, and partial denture making [68].

PMMA is an amorphous, but high-strength rigid polymer, with great dimensional stability. It can be polymerized by suspension, solution, or by emulsion and the T_g reaches 105 °C. It is quite inert towards chemicals, however, not towards organic solvents, transparent, and has great impact resistance in comparison with polyacrylates, which are softer, and because they are missing the extra methyl group, the polymeric chains are less rigid. Another important property of PMMA is biocompatibility [77]–[79], however, it could cause allergic reactions [80]. Polymethacrylates are usually shaped into finished products, whereas polyacrylates are used based on their flexibility and extensibility [68], [74].

To improve the mechanical properties of the methacrylate polymers, difunctional monomers were developed, and pioneered by Dr. Rafael Bowen [81]. His research was based on modifications of epoxy resins, where he substituted epoxy groups with methacrylate and produced a high molecular weight monomer (M = 512.6 g/mol), called bisphenol A glycerolate dimethacrylate (Bis-GMA), or Bowen's resin. Thanks to its additional functional groups, such as benzene rings, it has more hydrogen bonds, which in turn results in the very viscous form of monomer (η = 1369 Pa s) [82]. Mostly Bis-GMA is synthesized from bisphenol A and glycidyl methacrylate, or diglycidylether of bisphenol A (DGEBA) and methacrylic acid. The synthesis road of the first one is shown in Figure 1-10. To improve the mechanical properties of the methacrylate polymers, difunctional monomers were developed and pioneered by Dr. Rafael Bowen [81]. His research was based on modifications of epoxy resins, where he

substituted epoxy groups with methacrylate and produced a high molecular weight monomer (M = 512.6 g/mol), called bisphenol A glycerolate dimethacrylate (Bis-GMA), or Bowen's resin.
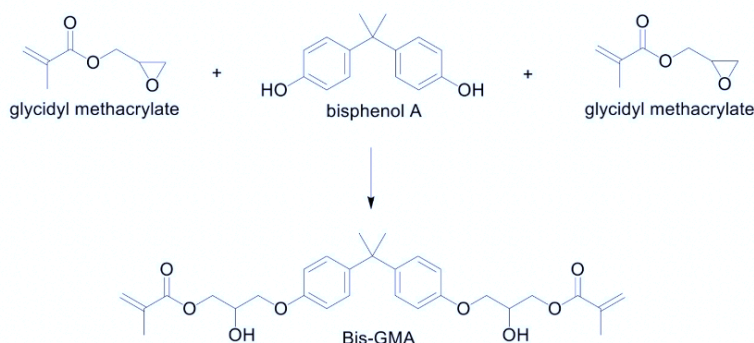
Figure 1-10: Synthesis of Bis-GMA [93]

Furthermore, the Bis-GMA molecule has a lower shrinkage ratio (~ 7.5%) in comparison with PMMA, thanks to the cohesive energy ratio and the higher molecular weight of the middle part of the molecule [83]. Another advantage is also its good biocompatibility demonstrated in several studies [84], [85]. However, in recent years multiple works on leaching assays demonstrated monomer release and some cytotoxicity [86], [87]. Thus, more investigations are necessary in this field. Nowadays, new Bis-GMA-free dental resins are being investigated [88], [89].

To ease the manipulation with such viscous monomers, like Bis-GMA, they are usually mixed with lower-molecular-weight monomers, also called viscosity controllers [90]. In the case of this study, it was triethylene glycol dimethacrylate (TEGDMA) with a molecular weight of 286.3 g/mol and viscosity η = 0.05 Pa s [82]. Some other viscosity controllers are ethylene glycol dimethacrylate (EGDMA), ethylene diglycol dimethacrylate (DEGDMA), and 2-hydroxyethyl methacrylate (HEMA), or 1,10-decanediol dimethacrylate (DDDMA or D3MA) [87]. However, the ratio of the two monomers should be carefully monitored,

as the addition of low molecular weight monomers increases polymerization shrinkage and can shorten the van der Walls distances by 50%. Except for polymerization shrinkage, the type of viscosity controller affects conversion, the reactivity of matrix, mechanical properties, and water absorption [68], [91], [92]. Other common methacrylate monomers used in dentistry are Bis-EMA, what is ethoxylated bisphenol A glycol dimethacrylate, bisphenol A dimethacrylate (Bis-DMA), urethane dimethacrylate (UDMA), and bis(acryloyloxymethyl) tricyclo [5.2.1.02,6] decane (TCD-DI-HEA) (Figure 1-11) [93].
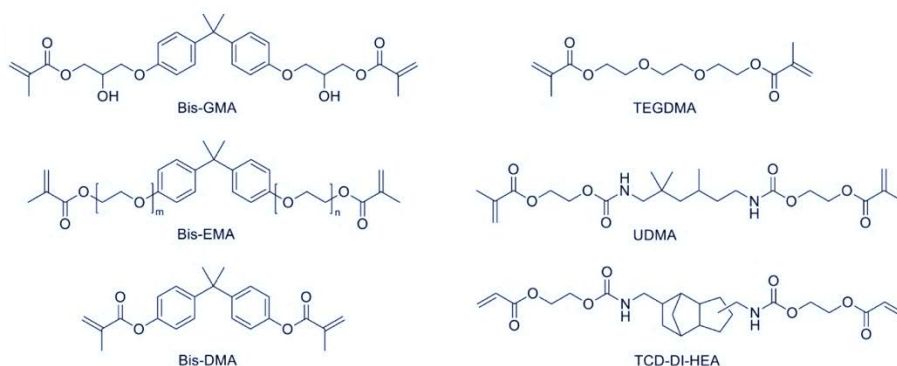
Figure 1-11: Methacrylate monomers used in dentistry [93]

Difunctional methacrylate monomers in dentistry are usually polymerized by radical polymerization, where the double bonds of ending vinyl groups are the active sites of the polymerization reaction. Based on the creation of free radicals the polymerization can be initiated chemically (self-curing), thermally, or by a photoinitiator [94]. Typically, in dentistry photopolymerization is the main technique sometimes paired with self-curing polymerization if the placement cannot be reached by light [94]. Although in the case of dentures or PICN thermopolymerization is used [95], [96]. An example of such polymerization thermally initiated by benzoyl peroxide is shown in Figure 1-12, where R represents the core of the used monomer [97]. During the polymerization

reaction, excessive crosslinking is present, which causes rapid changes in the viscosity of the system. The propagation and termination of the reaction are controlled by chemical processes, but with growing viscosity, the movement of the molecules is reduced. This is a cause for termination reaction to be controlled by diffusion, which slows it down. Slower termination influences the number of free radicals in the system and therefore the propagation speed is increased. This phenomenon is quite usual for methacrylate polymerization and is also called autoacceleration. After a rapid speed increase of reaction, the still-growing viscosity causes also propagation reaction to be controlled by diffusion, which is followed by a rapid decrease of the reaction, also known as autodeceleration [98], [99].
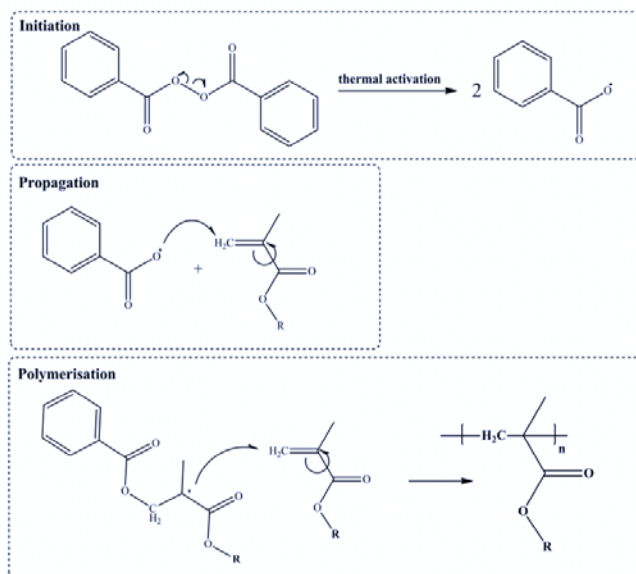
Figure 1-12: Radical polymerization of methacrylate monomers with benzoyl peroxide (BPO) as initiator. From top to bottom: Initiation, propagation, and polymerization [97].

Commercial difunctionalized methacrylates are used in dentistry as resins or sealants, however not as pure material but as dental composites. These composites consist of a base made of multiple different monomers and a filler.

Fillers are used to enhance mechanical and physical properties. Macro or nanoscaled fillers vary in shape and size as well as in dispersion, orientation, and surface modifications. A plethora of fillers has been studied [100]–[104], where some of the most important are silica-based glasses, metals, ceramics, natural minerals, and pre-polymerized particles. They can affect the final strengths, hardness, toughness as well as the polymerization shrinkage. Nevertheless, the most critical point that should be mentioned is the final aesthetics of the tooth filling [82], [105]. Therefore, the next section will introduce a relatively new concept to obtain hybrid materials with performances improved in comparison to the individual examples shown above, which could be useful for future uses in dentistry.

1.4   Polymer-infiltrated ceramic networks (PICN)

Polymer-infiltrated ceramic networks (PICN) can be defined as porous pre-sintered ceramic blocks, which are infiltrated with polymer matrix based on capillary action [106]–[109]. Based on the glass infiltrated ceramic systems, the first PICN was developed and commercialized by VITA Zahnfabrik (Bad Säckingen, Germany) under the commercial name of VITA ENAMIC , in 2012 [110]. The ceramic scaffold covers 86% of PICN whereas the polymeric network of UDMA and TEGDMA makes 14% of the final material as listed by VITA Zahnfabrik [111]. The composition of this feldspar ceramic scaffold of this hybrid material is listed in Table 1-4.

Table 1-4: Chemical composition of ceramic scaffold of commercial PICN (VITA ENAMIC®) [111]

Component		Percentage (%)
Silicon dioxide	SiO_2	58 – 63 %
Aluminum oxide	Al_2O_3	20 – 23 %
Sodium oxide	Na_2O	9 – 11 %
Potassium oxide	K_2O	4– 6%
Boron trioxide	B_2O_3	0.5 – 2 %
Zirconia	ZrO_2	<1 %
Calcium oxide	CaO	<1 %

This new system was developed based on the demand for new materials, which would be exhibiting mechanical properties more similar to natural dentin [112]. The manufacturing process consists of preparing the ceramic scaffold, sintering the porous scaffold, surface activation, capillary penetration of the ceramic voids, and thermal polymerization of the dental resin [113]. Presently they are manufactured in form of blocks, which are later modified with CAD/CAM technology, thus subtractive methods are used to produce the final pieces. Interpenetrated network of two materials makes the final product possess intermediate properties of the two ones, which makes it an ideal material for dental applications [109]. As mentioned earlier, pure ceramics exhibit high hardness and brittleness, which causes faster wear of surrounding natural teeth, mechanical failure, and discomfort for the patient [114]. Even though the less sufficient mechanical properties of the polymeric resins could be improved with inorganic fillers, the high content of filler particles makes the manipulation almost impossible due to the very high viscosity of the resin

composites [109], [113]. Therefore, the continuous ceramic material with capillaries filled with resin results in the desirable combination of both components of PICN [108], [115]. Another advantage of PICNs is their easier machinability, as they can be milled rapidly in very low thickness, they become less brittle, have high damage resistance, and are more resistant to marginal chipping [116].

Since the development of PICN, multiple studies were done to properly characterize aesthetic [117] and mechanical properties, such as hardness, elastic modulus, flexural strength, or fracture toughness [112], as well as their biocompatibility [116]. Comparison of some mechanical parameters of various PICN with human dentin and enamel are listed in Table 1-5. One of the main reasons to mimic the properties of natural teeth is the wear resistance of surrounding teeth. Xu et al. [108] observed that the wear mechanism of PICN is comparable with natural teeth. Other authors also observed satisfying wear properties of PICN in comparison with other materials [107], [114], [118].

Based on multiple studies the mechanical properties such as hardness, flexural strength, and elastic modulus are in proximity to those of natural teeth. It should be noted, that as this material is quite a novelty in the dentistry field, most of the studies were performed on VITA ENAMIC® (Table 1-5). Some other properties of the material were also studied, for example Özarslan *et al.* [121] studied the roughness and color shade of VITA ENAMIC®, whereas Zhawi et al. [122] analyzed flexural damage and resistance to fatigue content with satisfying results. Material with similar properties, which is often used as a comparison to PICN is Cerasmart by GC (Leuven, Belgium). However, this hybrid material is based on filler technology, rather than infiltration [115], [123], [124].

Table 1-5: Comparison of mechanical properties of different PICN composites and natural enamel and dentin testes in vitro over the last 10 years.

Composite	Vickers hardness [HV]	Elastic modulus [GPa]	Flexural strength [MPa]	Fracture toughness [MPa$^{1/2}$ m]	Ref.
Silica TEGMA/ UDMA	200-300	13-22	-	-	[118]
VITA ENAMIC®	177-190	20-38	-	-	[118]
VITA ENAMIC®	-	23.5	-	-	[108]
Silica TEGMA/ UDMA	301	-	-	-	[114]
VITA ENAMIC®	192	-	-	-	[114]
FELDSPAR TEGMA/ UDMA	107-220	16-28	130-160	-	[112]
Silica TEGMA/ UDMA	300	20.5	100	-	[119]
3Y-TZP TEGMA/ UDMA	40-92	14.5-38.8	58-90	0.8-1.4	[120]
3Y-TZP Bis-GMA/TEGMA	160-300	28-58	110-240	1.5-3.5	[106]
Enamel	270-420	48-105	-	0.4-1.5	[108], [112], [118]
Dentin	20-90	16-25	-	2.2-3.9	[108], [112], [118]

In the case of Li *et al.* [106], they developed their own PICN samples, where the ceramic used was 3Y-TZP, as it is one of the most used ceramics for dental restorative materials. The porous scaffolds were manufactured by cold isostatic pressing and the filling material was Bis-GMA/TEGDMA copolymer in a 50:50 ratio, respectively. Thermal copolymerization was initiated with benzoyl peroxide and occurred at 70 °C at atmospheric pressure. The four different sintering temperatures for preparing porous scaffolds in the range from 1000 °C to 1150 °C were observed, where the lather was chosen as the most suitable for dental application. It was preferred based on mechanical properties the most resembling natural teeth such as flexural strength (240.9 MPa), fracture toughness (1.55 –3.69 MPa$^{1/2}$ m), elastic modulus (28.6 to 58.8 GPa), and hardness (3.1 GPa). Part of this thesis was inspired by this study.

More recently, Sodeyama *et al*. [119] have developed a printable PICN, where the silica skeleton is 3D-printed by SLA, then sintered and subsequently filled with 3 different polymeric resins, the system filled with heat or photopolymerized TEGDMA and heat polymerized UDMA/TEGDMA copolymer. They obtained an elastic modulus of 18-21 GPa, corresponding to natural dentin as well as rest of the mechanical properties (Table 1-5, reference [119]) They were also able to 3D-print a crown model, which maintained stable after the application of the sintering step.

Biocompatibility assays have proven, that such materials are biocompatible. For example, Grenade et al. [116] have tested PICN against human gingival keratinocytes cells with similar results to pure zirconia and titanium samples. Cui et al. [125] have proven that the already good biocompatibility of PICN can be improved by modification with hydroxyapatite.

It should be mentioned, that even though the properties seem to be superior to other dental materials, the long-term application could not be properly evaluated, because of the short availability on the market [109]. However, Banh

et al. compared various clinical trials with follow-up periods of 2-3 years where the success of implantation was superior to 96%. PICN used in these trials was all VITA ENAMIC® based [126].

Based on all the aspects described in this chapter, the following chapters focus on the fabrication of PICN with the novelty of production of the ceramic scaffold by additive manufacturing, to be able to control the porosity and the geometry of the final product. The employed method was DIW to produce the green body and the sintered scaffolds were later filled with Bis-GMA/TEGDMA copolymer, as it is a commonly used resin in restorative dentistry. Also, numerous modifications were explored and described.

1.5   References

[1]   O. S. Abd El-Ghany and A. H. Sherief, "Zirconia based ceramics, some clinical and biological aspects: Review," *Future Dental Journal*, vol. 2, no. 2, pp. 55–64, 2016, doi: 10.1016/j.fdj.2016.10.002.

[2]   R. A. Bapat *et al.*, "Review on synthesis, properties and multifarious therapeutic applications of nanostructured zirconia in dentistry," *RSC Advances*, vol. 12, no. 20, pp. 12773–12793, 2022, doi: 10.1039/d2ra00006g.

[3]   E. C. Subbarao, H. S. Maiti, and K. K. Srivastava, "Martensitic transformation in zirconia," *physica status solidi (a)*, vol. 21, no. 1, pp. 9–40, 1974, doi: https://doi.org/10.1002/pssa.2210210102.

[4]   R. H. J. Hannink, P. M. Kelly, and B. C. Muddle, "Transformation toughening in zirconia-containing ceramics," *Journal of the American Ceramic Society*, vol. 83, no. 3, pp. 461–487, 2000, doi: 10.1111/j.1151-2916.2000.tb01221.x.

[5]   P. O. L. Duwez, F. Odell, and F. H. Brown Jr., "Stabilization of Zirconia with Calcia and Magnesia," *Journal of the American Ceramic Society*, vol. 35, no. 5, pp. 107–113, 1952, doi: https://doi.org/10.1111/j.1151-2916.1952.tb13081.x.

[6]   R. Muccillo, R. C. Buissa Netto, and E. N. S. Muccillo, "Synthesis and characterization of calcia fully stabilized zirconia solid electrolytes," *Materials Letters*, vol. 49, no. 3–4, pp. 197–201, 2001, doi: 10.1016/S0167-577X(00)00367-0.

[7]   R. C. Garvie, "The Occurrence of Metastable Tetragonal Zirconia as a Crystallite Size Effect," *The Journal of Physical Chemistry*, vol. 69, no. 4, pp. 1238–1243, 1965, doi: 10.1021/j100888a024.

[8]   R. C. Garvie and P. S. Nicholson, "Phase Analysis in Zirconia Systems," *Journal of the American Ceramic Society*, vol. 55, no. 6, pp. 303–305, 1972, doi: https://doi.org/10.1111/j.1151-2916.1972.tb11290.x.

[9]   A. Reckziegel, "Properties and Applications of High-Performance Ceramics Made of Zirconia," Mannheim-Germany, 2015.

[10]   P. H. Rieth, J. S. Reed, and A. W. Naumann, "Fabrication and flexural strength of ultrafine-grained yttria-stabilized zirconia," *American Ceramic Society Bulletin*, vol. 55, no. 8, pp. 717–721, 1976, [Online]. Available: http://inis.iaea.org/search/search.aspx?orig_q=RN:08295920

[11]   T. K. Gupta, J. H. Bechtold, R. C. Kuznicki, L. H. Cadoff, and B. R. Rossing, "Stabilization of tetragonal phase in polycrystalline zirconia," *Journal of Materials Science*, vol. 12, no. 12, pp. 2421–2426, 1977, doi: 10.1007/BF00553928.

[12]   P. Li, I. -W Chen, and J. E. Penner-Hahn, "Effect of Dopants on Zirconia Stabilization—An X-ray Absorption Study: III, Charge-Compensating Dopants," *Journal of the American Ceramic Society*, vol. 77, no. 5, pp. 1289–1295, 1994, doi: 10.1111/j.1151-2916.1994.tb05404.x.

[13]   P. Li, I.-W. Chen, and J. E. Penner-Hahn, "Effect of Dopants on Zirconia Stabilization—An X-ray Absorption Study: I, Trivalent Dopants," *Journal of the American Ceramic Society*, vol. 77, no. 1, pp. 118–128, 1994, doi: https://doi.org/10.1111/j.1151-2916.1994.tb06964.x.

[14]   P. Li, I.-W. Chen, and J. E. Penner-Hahn, "Effect of Dopants on Zirconia Stabilization—An X-ray Absorption Study: II, Tetravalent Dopants," *Journal of the American Ceramic Society*, vol. 77, no. 5, pp. 1281–1288, 1994, doi: https://doi.org/10.1111/j.1151-2916.1994.tb05403.x.

[15]   S. Fabris, A. T. Paxton, and M. W. Finnis, "A stabilization mechanism of zirconia based on oxygen vacancies only," *Acta Materialia*, vol. 50, no. 20, pp. 5171–5178, 2002, doi: 10.1016/S1359-6454(02)00385-3.

[16]   F. A. Kröger and H. J. Vink, "Relations between the Concentrations of Imperfections in Crystalline Solids," vol. 3, F. Seitz and D. B. T.-S. S. P. Turnbull, Eds. Academic Press, 1956, pp. 307–435. doi: https://doi.org/10.1016/S0081-1947(08)60135-6.

[17]   H. K. Kim, "Effect of a rapid-cooling protocol on the optical and mechanical properties of dental monolithic zirconia containing 3-5 mol% Y2O3," *Materials*, vol. 13, no. 8, 2020, doi: 10.3390/MA13081923.

[18]   T. Vagkopoulou, S. O. Koutayas, P. Koidis, and J. R. Strub, "Zirconia in dentistry: Part 1. Discovering the nature of an upcoming bioceramic.," *The European Journal of Esthetic Dentistry*, vol. 4, no. 2, pp. 130–151, 2009.

[19]   I. Denry and J. R. Kelly, "State of the art of zirconia for dental applications," *Dental Materials*, vol. 24, no. 3, pp. 299–307, 2008, doi: 10.1016/j.dental.2007.05.007.

[20]   A. A. Madfa, F. A. Al-Sanabani, N. H. Al-Qudami, J. S. Al-Sanabani, and A. G. Amran, "Use of Zirconia in Dentistry: An Overview," *The Open Biomaterials Journal*, vol. 5, no. 1, pp. 1–7, 2014, doi: 10.2174/1876502501405010001.

[21]   Z. Chen *et al.*, "3D printing of ceramics: A review," *J Eur Ceram Soc*, vol. 39, no. 4, pp. 661–687, 2019, doi: 10.1016/j.jeurceramsoc.2018.11.013.

[22]   C. Piconi, G. Maccauro, F. Muratori, and E. Brach Del Prever, "Alumina and zirconia ceramics in joint replacements.," *J Appl Biomater Biomech*, vol. 1, no. 1, pp. 19–32, 2003, [Online]. Available: http://www.ncbi.nlm.nih.gov/pubmed/20803469

[23]   S. M. Kurtz, S. Kocagöz, C. Arnholt, R. Huet, M. Ueno, and W. L. Walter, "Advances in Zirconia Toughened Alumina Biomaterials for Total Joint Replacement," *Molecular and Cellular Biochemistry*, vol. 23, no. 1, pp. 1–7, 2012, doi: 10.1016/j.jmbbm.2013.03.022.Advances.

[24]   F. H. Schünemann *et al.*, "Zirconia surface modifications for implant dentistry," *Materials Science and Engineering C*, vol. 98, no. July 2018, pp. 1294–1305, 2019, doi: 10.1016/j.msec.2019.01.062.

[25]   G. Plotino, N. M. Grande, R. Bedini, C. H. Pameijer, and F. Somma, "Flexural properties of endodontic posts and human root dentin," *Dental Materials*, vol. 23, no. 9, pp. 1129–1135, 2007, doi: 10.1016/j.dental.2006.06.047.

[26] K. J. Chun, H. H. Choi, and J. Y. Lee, "Comparison of mechanical property and role between enamel and dentin in the human teeth," *Journal of Dental Biomechanics*, vol. 5, no. 1, pp. 1–7, 2014, doi: 10.1177/1758736014520809.

[27] W. Li and J. Sun, "Effects of ceramic density and sintering temperature on the mechanical properties of a novel polymer-infiltrated ceramic-network zirconia dental restorative (filling) material," *Medical Science Monitor*, vol. 24, pp. 3068–3076, 2018, doi: 10.12659/MSM.907097.

[28] S. A. Kumar and R. V. S. Prasad, "Chapter 2 - Basic principles of additive manufacturing: different additive manufacturing technologies," in *Additive Manufacturing*, M. Manjaiah, K. Raghavendra, N. Balashanmugam, and J. P. Davim, Eds. Woodhead Publishing, 2021, pp. 17–35. doi: https://doi.org/10.1016/B978-0-12-822056-6.00012-6.

[29] M. Whitaker, "The history of 3D printing in healthcare. The Bulletin of the Royal College of Surgeons of England. 2014;96(7):228-229.," *Bulletin of The Royal College of Surgeons of England*, vol. 96, no. 7, pp. 17–19, 2015.

[30] M. A. S. R. Saadi *et al.*, "Direct Ink Writing: A 3D Printing Technology for Diverse Materials," *Advanced Materials*, vol. 2108855, pp. 1–57, 2022, doi: 10.1002/adma.202108855.

[31] C. W. Hull, "Apparatus for production of three-dimensional objects by stereolithography," US4575330A, 1986

[32] B. C. Gross, J. L. Erkal, S. Y. Lockwood, C. Chen, and D. M. Spence, "Evaluation of 3D printing and its potential impact on biotechnology and the chemical sciences," *Analytical Chemistry*, vol. 86, no. 7, pp. 3240–3253, 2014, doi: 10.1021/ac403397r.

[33] A. V. Kumar, "A Review paper on 3D-Printing and Various Processes Used in the 3D-Printing," *Interantional Journal of Scientific Research in Engineering and Management*, vol. 06, no. 05, 2022, doi: 10.55041/ijsrem13278.

[34] S. S. Crump, "Apparatus and method for creating three-dimensional objects," US5121329A, 1992

[35] E. M. Sachs, J. S. Haggerty, M. J. Cima, and P. A. Williams, "Three-dimensional printing techniques," USO05204055A, 1993

[36] S. J. Trenfield *et al.*, "Shaping the future: recent advances of 3D printing in drug delivery and healthcare," *Expert Opinion on Drug Delivery*, vol. 16, no. 10, pp. 1081–1094, 2019, doi: 10.1080/17425247.2019.1660318.

[37] Z. Gu, J. Fu, H. Lin, and Y. He, "Development of 3D bioprinting: From printing methods to biomedical applications," *Asian Journal of Pharmaceutical Sciences*, vol. 15, no. 5, pp. 529–557, 2020, doi: 10.1016/j.ajps.2019.11.003.

[38] G. Auriemma, C. Tommasino, G. Falcone, T. Esposito, C. Sardo, and R. P. Aquino, "Additive Manufacturing Strategies for Personalized Drug Delivery Systems and Medical Devices: Fused Filament Fabrication and Semi Solid Extrusion," *Molecules*, vol. 27, no. 9, 2022, doi: 10.3390/molecules27092784.

[39] A. Awad, F. Fina, A. Goyanes, S. Gaisford, and A. W. Basit, "3D printing: Principles and pharmaceutical applications of selective laser sintering," *International Journal of Pharmaceutics*, vol. 586, no. June, p. 119594, 2020, doi: 10.1016/j.ijpharm.2020.119594.

[40] J. Deckers, J. Vleugels, and J. P. Kruth, "Additive manufacturing of ceramics: A review," *Journal of Ceramic Science and Technology*, vol. 5, no. 4, pp. 245–260, 2014, doi: 10.4416/JCST2014-00032.

[41] R. Galante, C. G. Figueiredo-Pina, and A. P. Serro, "Additive manufacturing of ceramics for dental applications: A review," *Dental Materials*, vol. 35, no. 6, pp. 825–846, 2019, doi: 10.1016/j.dental.2019.02.026.

[42] M. V. Varma *et al.*, "3D printed scaffolds for biomedical applications," *Materials Chemistry and Physics*, vol. 255, no. August, p. 123642, 2020, doi: 10.1016/j.matchemphys.2020.123642.

[43] V. K. Balla, S. Bose, and A. Bandyopadhyay, "Processing of bulk alumina ceramics using laser engineered net shaping," *International Journal of Applied Ceramic Technology*, vol. 5, no. 3, pp. 234–242, 2008, doi: 10.1111/j.1744-7402.2008.02202.x.

[44] Y. Lakhdar, C. Tuck, J. Binner, A. Terry, and R. Goodridge, "Additive manufacturing of advanced ceramic materials," *Progress in Materials Science*, vol. 116, no. September 2020, p. 100736, 2021, doi: 10.1016/j.pmatsci.2020.100736.

[45] I. Joseph Cesarano and P. D. Cavert, "Freeforming objects with low-binder slurry," US006027326A, 2000

[46] N. Travitzky *et al.*, "Additive manufacturing of ceramic-based materials," *Advanced Engineering Materials*, vol. 16, no. 6, pp. 729–754, 2014, doi: 10.1002/adem.201400097.

[47] E. Feilden, E. G. T. Blanca, F. Giuliani, E. Saiz, and L. Vandeperre, "Robocasting of structural ceramic parts with hydrogel inks," *J Eur Ceram Soc*, vol. 36, no. 10, pp. 2525–2533, 2016, doi: 10.1016/j.jeurceramsoc.2016.03.001.

[48] K. Huang, H. Elsayed, G. Franchin, and P. Colombo, "Complex SiOC ceramics from 2D structures by 3D printing and origami," *Additive Manufacturing*, vol. 33, no. February, p. 101144, 2020, doi: 10.1016/j.addma.2020.101144.

[49] E. Juste, F. Petit, V. Lardot, and F. Cambier, "Shaping of ceramic parts by selective laser melting of powder bed," *Journal of Materials Research*, vol. 29, no. 17, pp. 2086–2094, 2014, doi: 10.1557/jmr.2014.127.

[50] T. Yu, Z. Zhang, Q. Liu, R. Kuliiev, N. Orlovskaya, and D. Wu, "Extrusion-based additive manufacturing of yttria-partially-stabilized zirconia ceramics," *Ceramics International*, vol. 46, no. 4, pp. 5020–5027, 2020, doi: 10.1016/j.ceramint.2019.10.245.

[51] Y. Sun, C. Wang, and Z. Zhao, "ZTA Ceramic Materials for DLP 3D Printing," *IOP Conference Series: Materials Science and Engineering*, vol. 678, no. 1, 2019, doi: 10.1088/1757-899X/678/1/012020.

[52] L. N. Khanlar, A. S. Rios, A. Tahmaseb, and A. Zandinejad, "Additive manufacturing of zirconia ceramic and its application in clinical dentistry: A review," *Dentistry Journal*, vol. 9, no. 9, 2021, doi: 10.3390/DJ9090104.

[53] J. Ebert *et al.*, "Direct Inkjet Printing of Dental Prostheses Made of Zirconia," *Journal of Dental Research*, vol. 88, no. 7, pp. 673–676, Jul. 2009, doi: 10.1177/0022034509339988.

[54] E. Özkol, W. Zhang, J. Ebert, and R. Telle, "Potentials of the ' Direct inkjet printing' method for manufacturing 3Y-TZP based dental restorations," *J Eur Ceram Soc*, vol. 32, no. 10, pp. 2193–2201, 2012, doi: 10.1016/j.jeurceramsoc.2012.03.006.

[55] D. Anssari Moin, B. Hassan, and D. Wismeijer, "A novel approach for custom three-dimensional printing of a zirconia root analogue implant by digital light processing," *Clinical Oral Implants Research*, vol. 28, no. 6, pp. 668–670, 2017, doi: 10.1111/clr.12859.

[56] R. B. Osman, A. J. van der Veen, D. Huiberts, D. Wismeijer, and N. Alharbi, "3D-printing zirconia implants; a dream or a reality? An in-vitro study evaluating the dimensional accuracy, surface topography and mechanical properties of printed zirconia implant and discs," *Journal of the Mechanical Behavior of Biomedical Materials*, vol. 75, no. August, pp. 521–528, 2017, doi: 10.1016/j.jmbbm.2017.08.018.

[57] Q. Lian, W. Sui, X. Wu, F. Yang, and S. Yang, "Additive manufacturing of ZrO ceramic dental bridges by stereolithography," *Rapid Prototyping Journal*, vol. 24, no. 1, pp. 114–119, Jan. 2018, doi: 10.1108/RPJ-09-2016-0144.

[58] W. Wang, H. Yu, Y. Liu, X. Jiang, and B. Gao, "Trueness analysis of zirconia crowns fabricated with 3-dimensional printing," *Journal of Prosthetic Dentistry*, vol. 121, no. 2, pp. 285–291, 2019, doi: 10.1016/j.prosdent.2018.04.012.

[59] R. Li *et al.*, "Strength and Adaptation of Stereolithography-Fabricated Zirconia Dental Crowns: An In Vitro Study.," *Int J Prosthodont*, vol. 32, no. 5, pp. 439–443, 2019, doi: 10.11607/ijp.6262.

[60] M. Revilla-León, M. M. Methani, D. Morton, and A. Zandinejad, "Internal and marginal discrepancies associated with stereolithography (SLA) additively manufactured zirconia crowns," *Journal of Prosthetic Dentistry*, vol. 124, no. 6, pp. 730–737, 2020, doi: 10.1016/j.prosdent.2019.09.018.

[61] W. Wang and J. Sun, "Dimensional accuracy and clinical adaptation of ceramic crowns fabricated with the stereolithography technique," *Journal of Prosthetic Dentistry*, vol. 125, no. 4, pp. 657–663, 2021, doi: 10.1016/j.prosdent.2020.02.032.

[62] A. Zandinejad, M. M. Methani, E. D. Schneiderman, M. Revilla-León, and D. M. Bds, "Fracture Resistance of Additively Manufactured Zirconia Crowns when Cemented to Implant Supported Zirconia Abutments: An in vitro Study," *Journal of Prosthodontics*, vol. 28, no. 8, pp. 893–897, 2019, doi: 10.1111/jopr.13103.

[63] Y. C. Cheng, D. H. Lin, C. P. Jiang, and Y. M. Lin, "Dental implant customization using numerical optimization design and 3-dimensional printing fabrication of zirconia ceramic," *International Journal for Numerical Methods in Biomedical Engineering*, vol. 33, no. 5, pp. 7–9, 2017, doi: 10.1002/cnm.2820.

[64] A. Ioannidis, D. Bomze, C. H. F. Hämmerle, J. Hüsler, O. Birrer, and S. Mühlemann, "Load-bearing capacity of CAD/CAM 3D-printed zirconia, CAD/CAM milled zirconia, and heat-pressed lithium disilicate ultra-thin occlusal veneers on molars," *Dental Materials*, vol. 36, no. 4, pp. e109–e116, 2020, doi: 10.1016/j.dental.2020.01.016.

[65] M. Peschka, "Equipment for adhesive bonding," in *Handbook of Adhesion Technology: Second Edition*, 2nd ed., vol. 2–2, L. F. M. da Silva, A. Öchsner, and R. D. Adams, Eds. Springer International Publishing, 2018, pp. 1098–1116. doi: 10.1007/978-3-319-55411-2_38.

[66] N. Thombare *et al.*, "Shellac as a multifunctional biopolymer: A review on properties, applications and future potential," *International Journal of Biological Macromolecules*, vol. 215, no. June, pp. 203–223, 2022, doi: 10.1016/j.ijbiomac.2022.06.090.

[67] M. Gilbert, "Plastics Materials: Introduction and Historical Development," *Brydson's Plastics Materials: Eighth Edition*, pp. 2–18, 2016, doi: 10.1016/B978-0-323-35824-8.00001-3.

[68] F. A. Rueggeberg, "From vulcanite to vinyl, a history of resins in restorative dentistry," *Journal of Prosthetic Dentistry*, vol. 87, no. 4, pp. 364–379, 2002, doi: 10.1067/mpr.2002.123400.

[69] C. Goodyear, "Improvement in India-Rubber Fabrics," US3633A, 1844 [Online]. Available: https://dl.acm.org/doi/10.1145/178951.178972

[70] L. H. Sperling, *History and Development of Polymer Blends and Ipns*, no. 2. American Chemical Society Division of Polymeric Materials: Science and Engineering, 2000. doi: 10.1016/b978-008043417-9/50020-9.

[71] H. Staudinger, "On Polymerization," in *A Source Book in Chemistry, 1900-1950*, H. M. Leicester, Ed. Harvard University Press, 2013, pp. 259–264. doi: doi:10.4159/harvard.9780674366701.c90.

[72] H. Frey and T. Johann, "Celebrating 100 years of 'polymer science': Hermann Staudinger's 1920 manifesto," *Polymer Chemistry*, vol. 11, no. 1, pp. 8–14, 2019, doi: 10.1039/c9py90161b.

[73] W. H. Carothers, "Linear condensation polymers," US2071250A, 1937

[74] G. Odian, *Principles of polymerization*, 4th ed. John Wiley & Sons, Inc, 2004.

[75] R. J. Young and P. A. Lovell, "Introduction to Polymers," in *Introduction to polymers*, 3rd ed., Taylor & Francis Group, LLC, 2011, pp. 3–14.

[76] A. F. Obilor, M. Pacella, A. Wilson, and V. v. Silberschmidt, *Micro-texturing of polymer surfaces using lasers: a review*, vol. 120, no. 1–2. Springer London, 2022. doi: 10.1007/s00170-022-08731-1.

[77] H. Kaur and A. Thakur, "Applications of poly(methyl methacrylate) polymer in dentistry: A review," *Materials Today: Proceedings*, vol. 50, pp. 1619–1625, 2021, doi: 10.1016/j.matpr.2021.09.125.

[78] B. Ali Sabri, M. Satgunam, N. M. Abreeza, and A. N. Abed, "A review on enhancements of PMMA Denture Base Material with Different Nano-Fillers," *Cogent Engineering*, vol. 8, no. 1, 2021, doi: 10.1080/23311916.2021.1875968.

[79] S. M. Pituru *et al.*, "A review on the biocompatibility of PMMA-Based dental materials for interim prosthetic restorations with a glimpse into their modern manufacturing techniques," *Materials*, vol. 13, no. 13, pp. 1–14, 2020, doi: 10.3390/ma13132894.

[80] G. Schmalz and D. A. Bindslev, *Biocompatibility of Dental Materials*. Springer Berlin Heidelberg, 2008. [Online]. Available: https://books.google.es/books?id=mrreTHuo54wC

[81] G. Furtos *et al.*, "Nano forsterite biocomposites for medical applications: Mechanical properties and bioactivity," *Journal of Biomedical Materials Research - Part B Applied Biomaterials*, vol. 104, no. 7, pp. 1290–1301, 2016, doi: 10.1002/jbm.b.33396.

[82] K. Cho, G. Rajan, P. Farrar, L. Prentice, and B. G. Prusty, "Dental resin composites: A review on materials to product realizations," *Composites Part B: Engineering*, vol. 230, no. November 2021, p. 109495, 2022, doi: 10.1016/j.compositesb.2021.109495.

[83] J. L. Ferracane, "Materials in dentistry : principles and applications," 2nd ed., S. Katz, Ed. Philadelphia: Lippincott Williams & Wilkins, 2001, pp. 223–281. [Online]. Available: http://www.tandfonline.com/toc/rwhi20/

[84] S. M. Mousavinasab, "Biocompatibility of composite resins.," *Dent Res J (Isfahan)*, vol. 8, no. Suppl 1, pp. S21-9, 2011, [Online]. Available: http://www.ncbi.nlm.nih.gov/pubmed/23372592%0Ahttp://www.pubmedcentral.nih.gov/articlerender.fcgi?artid=PMC3556298

[85] S. Imazato *et al.*, "Proliferation and differentiation potential of pluripotent mesenchymal precursor C2C12 cells on resin-based restorative materials," *Dental Materials Journal*, vol. 29, no. 3, pp. 341–346, 2010, doi: 10.4012/dmj.2009-082.

[86] F. de Angelis *et al.*, "Cytotoxic and genotoxic effects of composite resins on cultured human gingival fibroblasts," *Materials*, vol. 14, no. 18, pp. 1–15, 2021, doi: 10.3390/ma14185225.

[87] A. Szczesio-Wlodarczyk, J. Sokolowski, J. Kleczewska, and K. Bociong, "Ageing of dental composites based on methacrylate resins-A critical review of the causes and method of assessment," *Polymers (Basel)*, vol. 12, no. 4, 2020, doi: 10.3390/POLYM12040882.

[88] A. A. Pérez-Mondragón, C. E. Cuevas-Suárez, J. A. González-López, N. Trejo-Carbajal, M. Meléndez-Rodríguez, and A. M. Herrera-González, "Preparation and evaluation of a BisGMA-free dental composite resin based on a novel trimethacrylate monomer," *Dental Materials*, vol. 36, no. 4, pp. 542–550, 2020, doi: 10.1016/j.dental.2020.02.005.

[89] M. Lotfy, N. A. Mahmoud, and M. I. Riad, "Effect of preheating on polymerization shrinkage strain of BIS-GMA free and containing resin composite restorative materials (in vitro study)," *Bull Natl Res Cent*, vol. 46, no. 1, 2022, doi: 10.1186/s42269-022-00741-z.

[90] J. Stansbury and S. Dickens, "Network Formation and Compositional Drift During Photo-Initiated Copolymerization of Dimethacrylate Monomers," *Polymer (Guildf)*, no. 42, pp. 6363–6369, 2001, doi: 10.1016/S0032-3861(01)00106-9.

[91] N. Moszner and U. Salz, "New developments of polymeric dental composites," *Progress in Polymer Science*, vol. 26, no. 4, pp. 535–576, 2001.

[92] A. Peutzfeldt, "Resin composites in dentistry: the monomer systems.," *Eur J Oral Sci*, vol. 105, no. 2, pp. 97–116, Apr. 1997, doi: 10.1111/j.1600-0722.1997.tb00188.x.

[93] M. Šimková, A. Tichý, M. Dušková, J. Vítků, L. Kolatorova, and P. Bradna, "Bisphenols release from dental composite materials," *Endocrine Abstracts*, no. October, 2020, doi: 10.1530/endoabs.70.aep541.

[94] M. Cadenaro *et al.*, "The role of polymerization in adhesive dentistry," *Dental Materials*, vol. 35, no. 1, pp. e1–e22, 2019, doi: 10.1016/j.dental.2018.11.012.

[95] J. Tiu, R. Belli, and U. Lohbauer, "Characterization of heat-polymerized monomer formulations for dental infiltrated ceramic networks," *Applied Sciences (Switzerland)*, vol. 11, no. 16, 2021, doi: 10.3390/app11167370.

[96] S. Dur *et al.*, "An optimally solving dentistry internal purity in heat polymerized acrylic resin with different polymerization methods," *Systematic Reviews in Pharmacy*, vol. 11, no. 3, pp. 974–980, 2020, doi: 10.31838/srp.2020.3.149.

[97] P. Rodič, R. C. Korošec, B. Kapun, A. Mertelj, and I. Milošev, "Acrylate-based hybrid sol-gel coating for corrosion protection of AA7075-t6 in aircraft applications: The effect of copolymerization time," *Polymers (Basel)*, vol. 12, no. 4, 2020, doi: 10.3390/POLYM12040948.

[98] L. G. Lovell, J. W. Stansbury, D. C. Syrpes, and C. N. Bowman, "Effects of composition and reactivity on the reaction kinetics of dimethacrylate/dimethacrylate copolymerizations," *Macromolecules*, vol. 32, no. 12, pp. 3913–3921, 1999, doi: 10.1021/ma990258d.

[99] K. S. Anseth, C. M. Wang, and C. N. Bowman, "Reaction behaviour and kinetic constants for photopolymerizations of multi(meth)acrylate monomers," *Polymer (Guildf)*, vol. 35, no. 15, pp. 3243–3250, 1994, doi: 10.1016/0032-3861(94)90129-5.

[100] M. M. Karabela and I. D. Sideridou, "Synthesis and study of physical properties of dental light-cured nanocomposites using different amounts of a urethane dimethacrylate trialkoxysilane coupling agent," *Dental Materials*, vol. 27, no. 11, pp. 1144–1152, 2011, doi: 10.1016/j.dental.2011.08.008.

[101] N. Moszner and U. Salz, "New developments of polymeric dental composites," *Progress in Polymer Science*, vol. 26, no. 4, pp. 535–576, 2001, doi: 10.1016/S0079-6700(01)00005-3.

[102] S. Hesaraki, M. Karimi, and N. Nezafati, "The synergistic effects of SrF2 nanoparticles, YSZ nanoparticles, and poly-ε-L-lysin on physicomechanical, ion release, and antibacterial-cellular behavior of the flowable dental composites," *Materials Science and Engineering C*, vol. 109, no. February 2019, 2020, doi: 10.1016/j.msec.2019.110592.

[103] Y. Wang, H. Hua, Y. Yu, G. Chen, M. Zhu, and X. X. Zhu, "Dental Resin Composites Reinforced by Rough Core-Shell SiO2 Nanoparticles with a Controllable Mesoporous Structure," *ACS Applied Bio Materials*, vol. 2, no. 10, pp. 4233–4241, 2019, doi: 10.1021/acsabm.9b00508.

[104] M. Shen, G. Liang, A. Gu, and L. Yuan, "Development of high performance dental resin composites with outstanding antibacterial activity, high mechanical properties and low polymerization shrinkage based on a SiO2 hybridized tetrapod-like zinc oxide whisker with C=C bonds," *RSC Advances*, vol. 6, no. 61, pp. 56353–56364, 2016, doi: 10.1039/c6ra13498j.

[105] G. Furtos, M. Tomoaia-Cotisel, and C. Prejmerean, "Resin composites reinforced by glass fibers with potential biomedical applications. structure and mechanical properties," *Particulate Science and Technology*, vol. 31, no. 4, pp. 332–339, 2013, doi: 10.1080/02726351.2012.736458.

[106] J. Li *et al.*, "Mechanical performance of polymer-infiltrated zirconia ceramics," *Journal of Dentistry*, vol. 58, pp. 60–66, 2017, doi: 10.1016/j.jdent.2017.01.008.

[107] P. Yu, Z. Xu, D. D. Arola, J. Min, P. Zhao, and S. Gao, "Effect of acidic agents on the wear behavior of a polymer infiltrated ceramic network (PICN) material," *Journal of the Mechanical Behavior of Biomedical Materials*, vol. 74, no. April, pp. 154–163, 2017, doi: 10.1016/j.jmbbm.2017.06.001.

[108] Z. Xu, P. Yu, D. D. Arola, J. Min, and S. Gao, "A comparative study on the wear behavior of a polymer infiltrated ceramic network (PICN) material and tooth enamel," *Dental Materials*, vol. 33, no. 12, pp. 1351–1361, 2017, doi: 10.1016/j.dental.2017.08.190.

[109] T. S. Porto, R. C. Roperto, S. T. Porto-Neto, F. F. Faddoul, E. A. Campos, and S. T. Teich, "Polymer-Infiltrated-Ceramic-Network the Evolution of CAD/CAM Materials Review Article," *EC DENTAL SCIENCE*, vol. 3, no. 2017, pp. 94–98, 2018.

[110] L.-H. H. He and M. Swain, "A novel polymer infiltrated ceramic dental material," *Dental Materials*, vol. 27, no. 6, pp. 527–534, 2011, doi: 10.1016/j.dental.2011.02.002.

[111] "VITA ENAMIC ® VITA-perfect match. Technical and scientific documentation", [Online]. Available: https://www.vita-zahnfabrik.com/en/VITA-ENAMIC-24970,27568.html

[112] A. Coldea, M. v. Swain, and N. Thiel, "Mechanical properties of polymer-infiltrated-ceramic-network materials," *Dental Materials*, vol. 29, no. 4, pp. 419–426, 2013, doi: 10.1016/j.dental.2013.01.002.

[113] N. T. Manh *et al.*, "Fabrication of polymer infiltrated zirconia ceramic composite materials," *Molecular Crystals and Liquid Crystals*, vol. 707, no. 1, pp. 118–125, 2020, doi: 10.1080/15421406.2020.1743463.

[114] J. Tokunaga, H. Ikeda, Y. Nagamatsu, S. Awano, and H. Shimizu, "Wear of Polymer-Infiltrated Ceramic Network Materials against Enamel," *Materials*, vol. 15, no. 7, 2022, doi: 10.3390/ma15072435.

[115] A. Skorulska, P. Piszko, Z. Rybak, M. Szymonowicz, and M. Dobrzyński, "Review on polymer, ceramic and composite materials for cad/cam indirect restorations in dentistry—application, mechanical characteristics and comparison," *Materials*, vol. 14, no. 7, 2021, doi: 10.3390/ma14071592.

[116] C. Grenade *et al.*, "Biocompatibility of polymer-infiltrated-ceramic-network (PICN) materials with Human Gingival Keratinocytes (HGKs)," *Dental Materials*, vol. 33, no. 3, pp. 333–343, 2017, doi: 10.1016/j.dental.2017.01.001.

[117] W. H. Mörmann, B. Stawarczyk, A. Ender, B. Sener, T. Attin, and A. Mehl, "Wear characteristics of current aesthetic dental restorative CAD/CAM materials: Two-body wear, gloss retention, roughness and Martens hardness," *Journal of the Mechanical Behavior of Biomedical Materials*, vol. 20, pp. 113–125, 2013, doi: 10.1016/j.jmbbm.2013.01.003.

[118] Y. Kawajiri, H. Ikeda, Y. Nagamatsu, C. Masaki, and R. Hosokawa, "PICN Nanocomposite as Dental CAD / CAM Block Comparable," *Materials*, vol. 14, no. 1182, pp. 19–21, 2021, doi: 10.3390/ma14051182.

[119] M. K. Sodeyama, H. Ikeda, Y. Nagamatsu, C. Masaki, R. Hosokawa, and H. Shimizu, "Printable PICN Composite Mechanically Compatible with Human Teeth," *Journal of Dental Research*, vol. 100, no. 13, pp. 1475–1481, 2021, doi: 10.1177/00220345211012930.

[120] W. Li and J. Sun, "Effects of ceramic density and sintering temperature on the mechanical properties of a novel polymer-infiltrated ceramic-network zirconia dental restorative (filling) material," *Medical Science Monitor*, vol. 24, pp. 3068–3076, 2018, doi: 10.12659/MSM.907097.

[121] M. M. Özarslan, U. S. Büyükkaplan, Ç. Barutcigil, M. Arslan, N. Türker, and K. Barutcigil, "Effects of different surface finishing procedures on the change in surface roughness and color of a polymer infiltrated ceramic network material," *Journal of Advanced Prosthodontics*, vol. 8, no. 1, pp. 16–20, 2016, doi: 10.4047/jap.2016.8.1.16.

[122] H. el Zhawi, M. R. Kaizer, A. Chughtai, R. R. Moraes, and Y. Zhang, "Polymer infiltrated ceramic network structures for resistance to fatigue fracture and wear," *Dental Materials*, vol. 32, no. 11, pp. 1352–1361, 2016, doi: 10.1016/j.dental.2016.08.216.

[123] H. Lambert, J. C. Durand, B. Jacquot, and M. Fages, "Dental biomaterials for chairside CAD/CAM: State of the art," *Journal of Advanced Prosthodontics*, vol. 9, no. 6, pp. 486–495, 2017, doi: 10.4047/jap.2017.9.6.486.

[124] H. Yu, "Material selection for CAD/CAM dentistry: Glass ceramic or hybrid materials?," *Dental, Oral and Craniofacial Research*, vol. 5, no. 1, p. 1000278, 2019, doi: 10.15761/docr.1000278.

[125] B. Cui *et al.*, "Mechanical and biocompatible properties of polymer-infiltrated-ceramic-network materials for dental restoration," *Journal of Advanced Ceramics*, vol. 9, no. 1, pp. 123–128, 2020, doi: 10.1007/s40145-019-0341-5.

[126] W. Banh *et al.*, "Longevity of polymer-infiltrated ceramic network and zirconia-reinforced lithium silicate restorations: A systematic review and meta-analysis," *Materials*, vol. 14, no. 17, 2021, doi: 10.3390/ma14175058.

[127] K. Nakamura, "Mechanical and Microstructural Properties of Monolithic zirconia," University of Gothenburg, 2015.

[128] J. C. Fray, Derek Varga, Áron Mounsey, Steve Tan, "https://www.doitpoms.ac.uk/tlplib/fuel-cells/printall.php," *DoITPoMS, UK Centre for Materials Education*. https://www.doitpoms.ac.uk/tlplib/fuel-cells/printall.php

[129] "Encyclopædia Britannica," *T. Information Architects of Encyclopaedia "advanced structural ceramics."* [Online]. Available: ttps://www.britannica.com/facts/advanced-structural-ceramics. Accessed on 14th July 2022

[130] N. W. S. Pinargote, A. Smirnov, N. Peretyagin, A. Seleznev, and P. Peretyagin, "Direct ink writing technology (3d printing) of graphene-based ceramic nanocomposites: A review," *Nanomaterials*, vol. 10, no. 7, pp. 1–48, 2020, doi: 10.3390/nano10071300.

[131] M. Wu, P. Liu, S. Wang, C. Zhong, and X. Zhao, "Ultrasonic microwave-assisted micelle combined with fungal pretreatment of eucommia ulmoides leaves significantly improved the extraction efficiency of total flavonoids and gutta-percha," *Foods*, vol. 10, no. 10, pp. 1–21, 2021, doi: 10.3390/foods10102399.

[132] A. P. Mosley, "Brydson's Plastics Materials," in *Brydson's Plastics Materials*, 8th ed., M. Gilbert, Ed. Elsevier Ltd, 2017, pp. 441–456. doi: 10.1016/c2014-0-02399-4.

02

Objectives
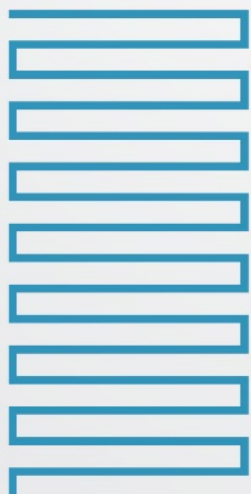
Objectives

The main objective of this thesis is the preparation of a hybrid material, composed of zirconia ceramic and acrylate polymers, for future implementation in the dentistry field. The aim of development of such system is to benefit from rather different material properties and create material applicable in the biomedical field. Along the side of mastering the assembly of such composite, various other modifications are explored to achieve the most suitable properties required for the final product. Therefore, the specific objectives can be divided into five areas:

1. Manufacture porous 3 mol% yttria-stabilized zirconia polycrystal (3Y-TZP) scaffolds with suitable macroscale porosity using direct ink writing (DIW) technology. In doing so, appropriate printing paste composition based on zirconia powder and Pluronic hydrogel was studied to obtain, after sintering, printed samples with good structural integrity.

2. Define the methodology to infiltrate biocompatible methacrylate copolymers in the porous zirconia scaffold, taking into account the 3D geometry. In this sense, adhesion of Bis-GMA/TEGDMA copolymer to zirconia is characterized, as well as copolymer composition.

3. Evaluate chemical and physical properties of the manufactured composite, including mechanical response, as well as its resistance towards bacterial growth. Explore also the biocompatibility of hybrid material with human cells, to ensure possible application in the biomedical field.

4. Improve osseointegration of zirconia materials using plasma deposition of polydopamine/acrylate copolymer, and concurrently study the

antimicrobial activity of such modified surfaces.

5. Explore and implement modification of hybrid composites with silver nanoparticles stabilized in phenolated lignin matrix to detect potential antimicrobial activity. Develop and verify methodology for the proper nanoparticles adhesion to composite surface.

03

Polymer infiltrated ceramic networks with biocompatible adhesive and 3D-printed highly porous scaffold:

Part 1

Samples preparation, characterization mechanical and antibacterial behaviors

Abstract

This chapter describes the manufacturing of an innovative polymer-infiltrated ceramic network (PICN) produced by additive manufacturing. The preparation of cubic structures printed by perpendicular layer-by-layer deposition of yttrium-stabilized tetragonal zirconia polycrystal (3Y-TZP) and Pluronic® hydrogel ceramic paste is described. The specimens fabricated by DIW, also called robocasting, with 50% infill and 50% of pores, as feed setup, are characterized in this chapter. As a filling material to produce PICN samples, a well-known biocompatible adhesive, which is widely used in the dentistry field; the bisphenol A glycerolate dimethacrylate (Bis-GMA) and tri(ethylenglycol) dimethacrylate (TEGDMA) copolymer was used to reinforce the pores of the 3D-printed ceramic structure. The proper infiltration and adhesion of the copolymer to the zirconia structure were explored. The infiltration of the zirconia structure with the copolymer was supported by previous activation of the surface with 3-(trimethoxysilyl)propyl methacrylate (γ-MPS), i.e. with sol-gel technology. The correct infiltration of pores, based on the gravimetry, was determined, and also, the mechanical properties of the specimen undergoing compression tests were described. Moreover, the aspect of resistance towards bacteria was tested, where Gram-negative *Escherichia coli* and Gram-positive *Streptococcus salivarius* bacteria lines were tested against all the stages of manufacturing of the composite.

3.1   Introduction

Nowadays, 3D-printing is a well-established and suitable technology for the dentistry industry [1], [2]. The range of dental devices that can be processed with 3D printing technologies is wide, including teeth restorations, dental appliances, orthodontic and prosthodontic models, dentures, orthodontic splints, dental trays, utensils, surgical guides, crowns, and bridges, among others [3]– [8].

Within the above context, some companies have specialized in designing and fabricating sophisticated 3D-printers for the dental market (e.g., 3D Systems Inc., EnvisionTEC Inc., Stratasys Ltd., and others). The availability of such speedy printers together with advanced software is transforming the dental field. A number of healthcare companies have launched their commercial activity based on additive manufacturing (NextDent B.V., Hybrid Technologies USA, Glidewell Laboratories Inc., etc). Several production methods are available, such as selective laser sintering (SLS),[9] direct metal printing (DMP),[10] selective laser melting (SLM),[11] stereolithography (SLA)[12][13] and digital light processing (DLP),[14][15][16] among others [4], [5], [17]. In this sense, the robocasting process allows obtaining dental pieces without shape restrictions, high dimensional precision, smooth finishing, efficiency, repeatability, and cost-effectiveness [18], [19].

Although lots of different classes of materials are being used for 3D-printing technologies[20]– [25], among them, ceramic compounds are the most widely used for dentistry applications. The most important classes in the biomedical field are alumina (α-Al_2O_3), spinel ($MgAl_2O_4$), and zirconia (ZrO_2) [26]. Yttrium-stabilized zirconia (YSZ) [27] has shown great promise in many challenging situations (for example, in single-tooth restoration and long-span bridges) due to its advantageous properties with respect to other dental materials, such as

the excellent aestheticism (brightness, refraction, coloring finishing), chemical resistance, improved mechanical behavior compared to alumina and spinel, bending strength and fracture toughness, high ionic conductivity, low thermal conductivity at high temperature together with relatively high thermal expansion coefficient, and high thermal stability of degradation-resistance [5], [28].

Despite its excellent properties, the major shortcoming of YSZ material is the low resistance to crack growth compared to metal implants, i.e., it behaves as a brittle material when subjected to impacts. Depending on the fabrication method and sintering temperature, the mechanical properties of zirconia vary substantially (fracture toughness ~25-60 GPa, flexural strength ~ 150-250 MPa, elastic modulus ~ 200-220 GPa).[29][30] Aiming to overcome this drawback and driven by the demands to design restorations with a real tooth-like function, fracture toughness and flexural strength of YSZ have been improved by following several approaches. For example, Srigurunathan et al. [31] have explored the benefits of doping ZrO_2 powder with rare-earth elements on the mechanical and optical properties of this material for biomedical applications. On the other hand, polymer-infiltrated-ceramic-network (PICN) materials have emerged in recent years, inspired by glass-infiltrated ceramic [32] structures [33]– [36]. Pioneering work developed by Li et al. [30] demonstrated an enhanced mechanical performance improvement of polymer-infiltrated zirconia ceramics using bisphenol A glycerolate dimethacrylate (Bis-GMA) and tri(ethylenglycol) dimethacrylate (TEGDMA) prepared by the conventional solid-state ceramic process. Resistance to crack extension was substantially increased, as compared to the one exhibited by the porous zirconia ceramic precursors. Thus, the infiltrated polymer acted as the plasticizers do in polymer transformation, reducing the rigidity of the matrix.

Unfortunately, ceramic computer-aided printing is easier for solid substrates pieces than for porous scaffold designs. This is mainly due to the weight of ceramic compounds that may lead to the bowing of filaments after the deposition and, therefore, user dissatisfaction. To overcome these problems, the direct-write assembly of materials with fugitive inks, developed by Lewis and co-workers [37], [38], and nowadays commonly referred to as robocasting or robotic direct deposition of ink filament, is a suitable option to retain both the shape of the scaffolds during fabrication and the dimensional stability of the ceramic filaments after the sintering process.

From all of the above-mentioned aspects, we can conclude that it is extremely difficult to obtain porous architectures from ceramic inks with additive manufacturing. Once the filaments are sintered at high temperatures, they usually break or deform. In this work, we were able to prepare stable 3D ceramic scaffolds by controlling several printer parameters (nozzle diameter, deposition speed, ink concentration) and by adding a polymer adhesive to reduce the stress of the scaffold filaments. For it, a strategy of zirconia surface functionalization with 3-(trimethoxysilyl) propyl methacrylate) [39], [40], was useful for the covalent adhesion of the biocompatible acrylate polymer. The idea of PICN fabrication with direct polymer infiltration aims to create a dental implant with superior properties, such as a long lifespan, mechanical properties mimicking natural enamel and dentin to reduce mandibular bone stiffness, easy fabrication with the possibility of personalized design, and ceramic-polymer interface without bacterial growth and adhesion promotion. Until now, PICN studies have been addressed with solid YSZ samples, in which porosity changes uniquely depending on the sintering temperature and fabrication method (hot-pressing or cold-isostatic pressing). The novelty of the present work relies on the obtaining of a well-controlled scaffold arrangement by establishing a pre-

fixed porosity, for the polymer infiltration, with the help of 3D-printing advanced equipment.

The properties of the whole scaffold will depend on the piece geometry, surface modification, and porosity, among other parameters. Furthermore, zirconia crowns have been used as an alternative to the common gold, alumina, and lithium disilicate crowns as well, and is due, in part, to its excellent antimicrobial behavior compared to the formers [41], [42]. However, the surface modification and geometry of biomaterial scaffolds will affect both the growth and adhesion of bacteria commonly found in the oral cavity [43]. Thus, detailed material characterization is necessary, as well as the investigation of the influence of such aspects on its microbial activity. The success of dental restoration therefore will be due to the success of avoiding biofilm formation.

The forecast growth of digital dentistry was calculated to be 23.2 % from 2018 to 2023, and it will represent a global market of 5.06 billion USD by 2023, which justifies the need for more investigations in this field [14], [15], [44].

3.2   Experimental procedure
3.2.1   Materials

3Y-TZP (3 mol% yttrium- stabilized tetragonal zirconia polycrystal) with an average particle size of 300 nm (measured by SEM) and ceramic density of 6.05 g·cm^{-3}, was provided by SEPR Saint-Gobain ZirPro under the commercial name CY3Z-R. The theoretical value of ceramic density (CY3Z-R grades) was taken from the technical datasheet available on the Saint-Gobain website. Pluronic® F-127 hydrogel; γ-MPS (3-(trimethoxysilyl) propyl methacrylate); Bis-GMA (bisphenol A glycerolate dimethacrylate); TEGDMA (triethylene glycol dimethacrylate) and BPO (benzoyl peroxide, Luperox®A75,) were all provided by Sigma-Aldrich.

For antimicrobial activity assays, Gram-negative *Escherichia coli (E. coli)* and Gram-positive *Streptococcus salivarius (S. salivarius)* bacteria lines were used.

The other reagents employed for the bacteria culture media growth will be described in section 3.2.4

3.2.2 3D-printed ceramic samples manufacturing

Porous zirconia structures were prepared from 25% Pluronic® F-127 hydrogel (25% w/w of Pluronic and 75% w/v of water) and 3Y-TZP powder at a 30:70 weight ratio, respectively. They were 3D-printed by the robocasting method (Figure 3-1a-b) at Saint-Gobain Research Provence (France),[1] employing a 3D Dima Elite dispenser (Nordson Dima, Netherlands) equipped with DimaSoft CAD/CAM software. Zirconia scaffolds were printed as $1.5 \times 1.5 \times 1.0$ cm^3 cubes with 50% infill of zirconia using an 800 µm cylindrical nozzle for extrusion of ceramic paste from a syringe (Figure 3-1b), subsequently dried for 2 days in a chamber with a controlled relative humidity of 90%, and for 2-3 days at 45% humidity chamber. Afterward, a two-stage sintering process at 700°C and 1450ºC, for 1h and 2h respectively (Figure 3-1c), was applied to obtain a stable tetragonal composition of zirconia particles. The heating and cooling temperature rates have been kept constant and equal to 3 ºC/min. During the sintering process ~20 % shrinkage occurs within specimens' dimensions due to the degradation of the Pluronic® hydrogel and ceramic compactness, as will be discussed in the results section.

3.2.3 Dip-coating method to obtain the polymer-infiltrated ceramic networks (PICN)

Here, for a good swelling and adhesion of the polymeric adhesive to the 3D-printed ceramic samples composed of aligned filaments and macropores, a simple surface modification strategy was employed: (i) activation of the zirconia surface with a silane coupling agent, and (ii) in-situ copolymerization of

---

[1] The candidate has recieved a training and performed 3 stays (2 months) to print all the samples, under the European project AMITIE (Marie Skłodowska Curie Grant Agreement n°734342)

methacrylate polymer. The ceramic scaffolds were carefully cleaned by immersion in distilled water, subsequently dipping in ethanol solvent (96%), and drying through airflow. In parallel, a solution of γ-MPS (24 mmol of liquid silane in 100 mL of 3:1 ethanol:water volume ratio) was prepared and left under magnetic stirring, for 1 h, for the silane hydrolysis. Afterward, the 3D-printed zirconia samples were submerged in such solution for 1 h, removed, and left to wring thoroughly to eliminate the excess of liquid.

For the obtaining of Bis-GMA/TEGDMA copolymer, with a molar ratio of 40:60 wt. %, covalently bonded to the 3D-printed zirconia cubes, the following procedure is exemplified. Previously to the immersion of the samples, a viscous solution of 39.5 wt. % Bis-GMA, 59.5 wt. % TEGDMA and 1.0 wt. % of BPO, as initiator, was prepared. The monomers were weighed in an analytical balance. Due to the high viscous property of Bis-GMA, the total amount of TEGMDA was adjusted to complete 99 wt. %. The catalyst amount was maintained constant. The whole system was stirred for 1 h at room temperature to start the copolymerization reaction. After the radical polymerization initiation, the silane-activated pieces were immersed for 1 h in the methacrylate viscous solution. Then, samples were carefully removed from the solution, the excess liquid was left to drain, and the pieces were placed in a glass petri dish, covered with aluminum foil before being transferred to the oven. The complete polymerization reaction was carried out by placing the samples in a JP Selecta Vaciotem-T vacuum oven, for 10 h at 115°C (Figure 3-1d). Subsequently, the 3D-printed PICN samples were cleaned with distilled water and ethanol before they were used for characterization studies. Two more molar ratios of Bis-GMA and TEGDMA were also prepared with the same procedure: 30:70 wt. % and 50:50 wt. %. For the quantification of the amount of copolymer infiltrated, the samples were weight before and after the final process. All of the above-mentioned compositions were characterized by FTIR and Raman spectroscopies as well as

by thermal analysis. Finally, the 40:60 Bis-GMA/TEGDMA copolymer was further investigated with XPS and Raman confocal analyses. In addition, bacterial cultures were conducted to assess its antimicrobial activity.
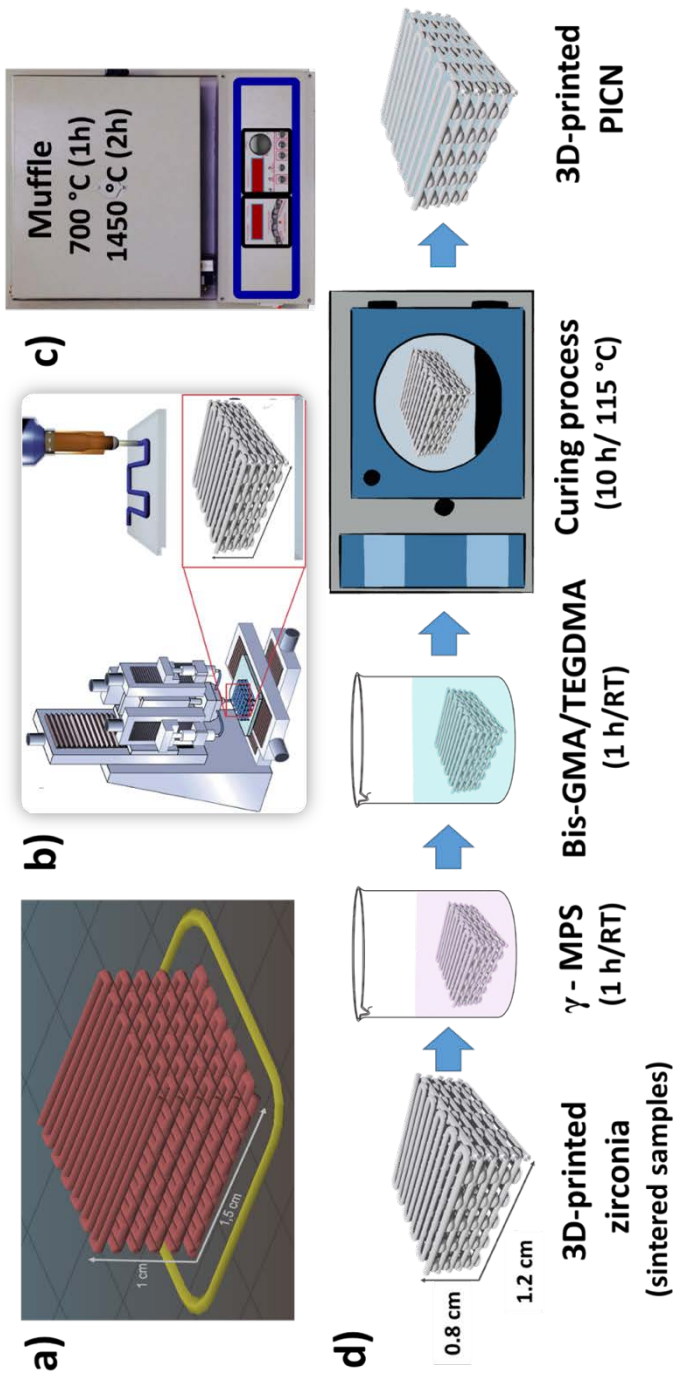
Figure 3-1: (a) DimaSoft CAD/CAM 3D design of simple cubic geometry (zig-zag filament layer-by-layer deposition and number of layers =10) of 3Y-TZP paste printing with 50% infill of zirconia. (b) Illustration of an ink-jet printer, filament deposition and the 3D-printed cubic specimen (Adapted from references [37], [38]). (c) Sintering process with two stepwise heating, employing muffle furnace. (d) Sequential steps for the functionalization and copolymer deposition onto 3D-printed ceramic samples used in the present study.

3.2.4   Physical-chemical characterization

In order to evaluate the chemical structure of all PICN samples, from the silane surface functionalization to the copolymer-infiltrated samples, spectroscopy (FTIR-ATR, micro-Raman, and XPS) and thermal analyses were performed. Infrared absorption spectra were recorded with a Fourier Transformation Infrared Spectrometer (FTIR) Jasco 4100, equipped with an ATR accessory and heating accessory Heated Golden Gate Controller by SPECAC. Spectra were obtained in a range of 4000-600 cm^{-1} and after the accumulation of 63 scans.

Raman spectra and 3D-mapping images of 3D-printed zirconia with infiltrated polymer network were obtained using Renishaw's inVia Qontor Raman microscope and Raman Environment (Wire™) software. The spectrometer is equipped with a Leica DM2700 M microscope for confocal measurements and LifeTrack technology for rough and curved surfaces. The spectra were recorded in the range of 4000-100 cm^{-1} and with a source of 532 nm, due to the hybrid nature of the whole implant model.

The chemical structure of the γ-MPS monolayer was evaluated using XPS due to the nanometric dimensions of the film. The equipment used was a SPECS system equipped with a high-intensity twin anode X-ray source XR50 of Mg/Al (1253 eV/1487 eV), operating at 150 W, placed perpendicular to the analyzer axis, and using a Phoibos 150 MCD-9 XP detector. The spectra were recorded with a pass energy of 25 eV in 0.1 eV steps, for the survey and narrow scans, at a pressure below 6×10-9 mbar. As the internal reference, the C 1s peak with a binding energy of 284.8 eV was used. The atomic percentage of each element was determined by dividing the peak area of the most intense XPS signal of each element by the corresponding sensitivity factor and expressing it as a fraction of the sum of all normalized peak areas. High-resolution XPS spectra were acquired

by Gaussian/Lorentzian curve, fitting after S-shape background subtraction, for the following elements: C 1s, O 1s, Si 2p, and Zr 3d.

The thermal analysis was performed with differential scanning calorimetry (DSC) was carried out with T*zero* technology and TA instrument Q100 to obtain calorimetric data of Bis-GMA/TEGDMA copolymers. Experiments were performed with heating and cooling rates of 10°C/min, under a nitrogen flow, and with 5 mg of sample for each measurement. The equipment was calibrated with indium. T*zero* calibration required two experiments: the first was performed without samples, while the second uses sapphire disks.

Thermal degradation was observed up to a temperature of 600°C, under a nitrogen flow, and using a Q50 thermogravimetric analyzer (TGA) by TA Instruments. Approximately 10 mg of the copolymer was placed into the equipment and a heating rate of 10°C/min was applied.

The scaffold porosity ($P_{scaffold}$) of each sample was calculated by dividing the scaffold's weight ($m_{scaffold}$) by the theoretical weight of a scaffold with 100% infill ($m_{theoretical}$):

$$P_{scaffold} = \left(1 - \frac{m_{scaffold}}{m_{theoretical}}\right) x \, 100 \qquad \text{(Eq. 1)}$$

The scaffold's theoretical weight ($m_{theoretical}$) was determined by a density equation using the density of material (6.05 g/cm^3) and the volume of the scaffold was calculated from the dimensions of the sample. Up to five mass measurements were taken to determine the porosity of the 3D-printed zirconia scaffold, with a 50 % of hollow structure, using a Mettler Toledo analytical balance (maximum capacity 81/120 g, repeatability $\pm$ 0.01/0.1 mg).

The success of polymer infiltration (I) into the pores was calculated with the following equation:

$$I = \left(\frac{m_{PICN}}{m_{PICN(T)}}\right) x \ 100 = \left(\frac{m_{PICN}}{\rho_{PICN(E)} \ x \ V_{PICN}}\right) x \ 100 \qquad \text{(Eq. 2)}$$

where m_{PICN} is the weight of PICN composite and $m_{PICN(T)}$ is the theoretical weight of PICN specimen with 100% pores infiltrated. The latter, in turn, was calculated from the experimental density ($\rho_{PICN(E)}$) of composite and volume (V_{PICN}) of composite determined from dimension measurements. The experimental density of composite ($\rho_{PICN(E)}$) was individually determined for each sample using the density of zirconia and the density of the copolymer (1.18 g/cm^3), according to equation 3:

$$\rho_{PICN(E)} = \left(1 - \frac{P_{scaffold}}{100}\right) x \ \rho_{zirconia} + \frac{P_{scaffold}}{100} x \ \rho_{Copolymer} \qquad \text{(Eq. 3)}$$

The experimental density of the zirconia filaments was measured by using a gas displacement pycnometer (Micrometrics Instrument Co., model AccuPyc 1330). The equipment determines density and volume with a pressure change of helium atmosphere in a vial with calibrated volume. Afterward, the density is calculated by dividing weight by the measured volume of a sample.

Morphology characterization and proper infiltration of polymer into zirconia structure were observed by SEM using a Focused Ion Beam Zeiss Neon 40 instrument, commercialized by Carl Zeiss (Germany). In order to avoid electron discharge, samples were carbon-coated using Mitek K950 Sputter Coater before

analysis. The accelerating voltage for obtaining morphology micrographs was 2 kV.

The side part of the copolymer infiltrated samples was appropriately polished by hand with silica carbide sandpapers, gradually evolving from P 600 to P 2500 level of abrasion before the analysis, to obtain a smooth surface for the observation of polymer-ceramic interface. SEM was also employed to observe the bacterial colonies formed on the surface of PICN hybrid material, after antibacterial activity experiments (Section 3.2.4).

Compression strength was measured while undergoing a compression test performed by an Instron 8511 compression machine, with a maximum load of 10 kN. The implied pressure rate for the experiment was 0.5 mm/s and the overall maximum pressure applied was ~7 kN. The results are represented as stress-strain curves (Section 3.3.3).

3.2.5 Antibacterial activity

To evaluate the antimicrobial activity, the bacteria adhesion, and growth of two different lines, have been investigated in the presence of zirconia 3D-printed scaffolds, zirconia 3D-printed scaffolds with γ-MPS coating, and PICN hybrid material with a composition of 40:60 Bis-GMA/TEGDMA copolymer. Within this context, *Escherichia coli (E. coli)* and *Streptococcus salivarius (S. salivarius)*, as Gram-negative and Gram-positive microorganisms, respectively, were employed. The bacteria were grown aerobically in Luria-Bertani (LB) broth culture (10 g/L tryptone, 5 g/L yeast extract, 5 g/L NaCl, pH 7.2) in advance, 7×10^9 colony-forming units (CFU) per mL being seeded in 10 mL LB broth medium after 24h. For antimicrobial assays, 7×10^9 of CFU/mL were seeded in sterile vials containing the specimens and fresh 10 mL of LB broth. For the control sample, bacteria were cultured in a sterile vial without the presence of any additional material. Both sample lines, including control samples, were stored,

and incubated for 24 h at 37°C and 90 rpm. Then, the turbidity of the solutions was analyzed using UV absorbance, 200 μL of bacteria solution for all the samples was placed in a 96-well plate and measured at λ= 595 nm in a microplate reader (EZ Read 400– Biochrom, UK) with ADAP 2.0 Plus Data Analysis Software.

A similar procedure was utilized for bacteria adhesion assays. However, after seeding the samples in fresh LB broth for 24 h, they were lightly washed with distilled water and incubated again for 24h, before counting. The counting was carried out by UV spectroscopy, employing the same procedure described above. The absorbance data were then compared with the control, which was prepared with 7×10^9 of CFU/mL seeded in sterile vials containing fresh 10 mL of LB broth without specimens.

The results of both experiments (i.e., antimicrobial activity and adhesion) are expressed in terms of relative cell viability to the control, and the average of 3 replicates of each type of sample was performed with both bacteria lines. Statistical analyses were performed with a confidence level of 95% ($p < 0.05$) using the Student's T-test.

Confocal laser scanning microscopy (LSM), which was performed using a Carl ZEISS LSM 800 equipment capable of performing epifluorescence techniques, was employed to observe bacteria colored with a blue fluorescent dye (Hoechst 33342).

3.3 Results and discussion

3.3.1 3D-printing of yttrium-stabilized tetragonal zirconia ceramic with high porosity

3D-printed cubes with controlled height, width, and length, as well as controlled hollow structure, were successfully extruded by robocasting manufacturing after the optimization of the printer trials (Figure 3-2a).

Filaments were printed layer-by-layer in a perpendicular fashion, creating a grid-like structure, with macropores (Figure 3-2b). Those macropores imparted high porosity to the ceramic scaffold, allowing better penetration of polymeric resins in comparison to the classical method of PICN with polymer inside micropores. As commonly occurs, after the sintering process from 700ºC to 1450ºC, the samples lose about 20 % of the original printed dimensions, being the final size of $1.2 \times 1.2 \times 0.8$ cm^3. Due to this variation in sample dimensions and scaffold pore size, the proper ratio of Bis-GMA and TEGMA monomers was adjusted for the full infiltration of the copolymer inside the ceramic devices. A representative example of the PICN pieces with the copolymer film with 50:50 wt. % of Bis-GMA/TEGDMA composition is displayed in Figure 3-2c.
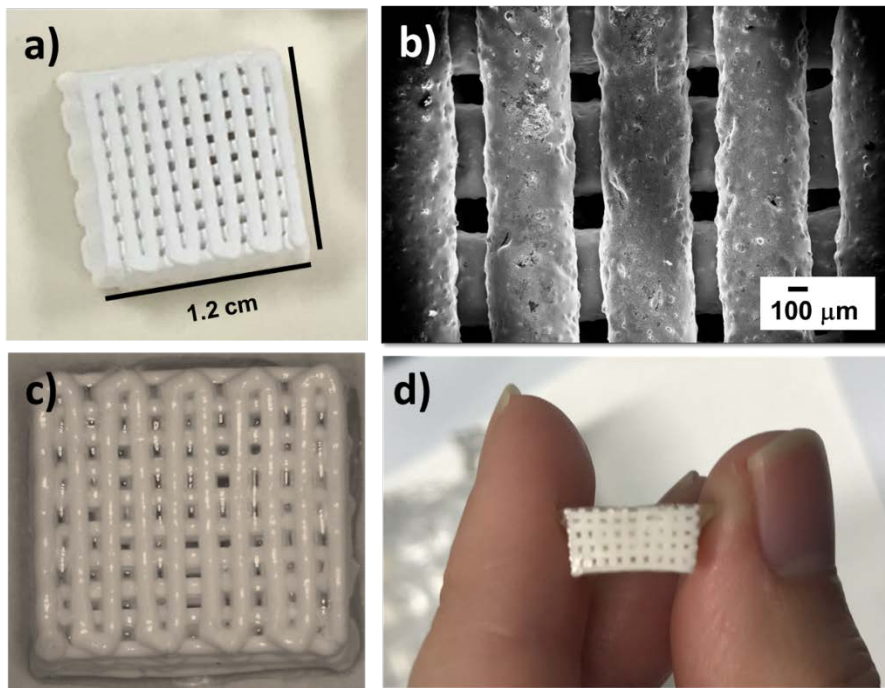
Figure 3-2 (a) Photograph of 3D-printed zirconia cube with stable dimensionality and pores formation upon drying and sintering processes. (b) SEM micrograph of zirconia filaments after printing and sintering processes. (c) Photograph of one PICN cube with 50 wt. % filled of 40:60 Bis-GMA/TEGDMA copolymer (gloss aspect over the filaments and inside the pores represents the copolymer coating and filling materials). (d) Photograph of 3D-printed ceramic with Bis-GMA/TEGDMA copolymer (lateral view).

The major drawback of the 3D-printing process was the effective control of the mixture viscosity, which is highly dependent on the temperature and relative humidity of the mixture and printer rooms. By maintaining both parameters constant, it was possible to obtain reproducible pieces. Another relevant aspect to be taken into consideration was the printer head. Using a nozzle of 800 µm in diameter, homogenous filaments diameter (704 $\pm$ 22 µm), pore sizes (422 $\pm$ 45 µm wide), and the dimensional stability of the whole piece was reached. Despite such parameters being well controlled, the printed ceramic samples with a 50% infill configuration had a slightly larger base than top dimensions upon drying and sintering processes, as can be seen from the photograph taken of one piece (Figure 3-2d, lateral view). It should be noted that, among over 25 printed pieces, a few samples (2-3) had some irregular edges and non-homogenous porosity. However, when using a smaller nozzle (580 µm), the dimensional integrity was completely lost (Figure 3-3).
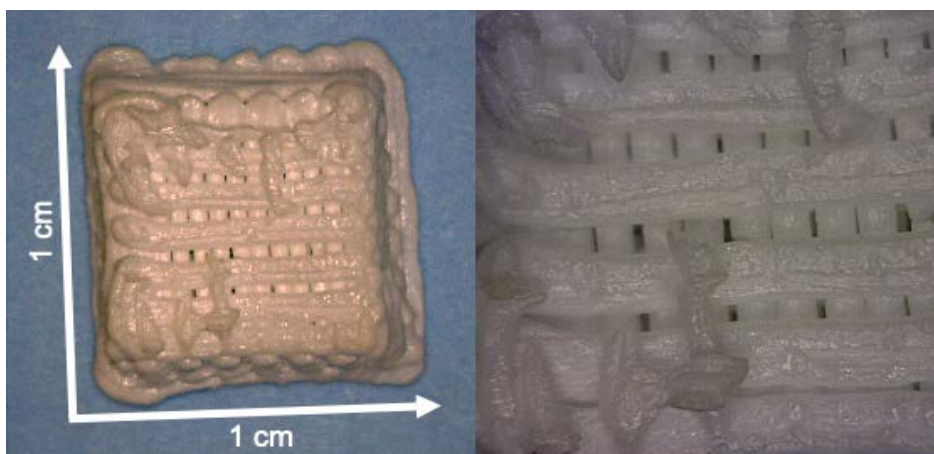
Figure 3-3: 3D-printed ceramic samples with 50% infill of zirconia after sintering, printed by using a printer head with tip diameter of 580 µm. Photographs were obtained using a DinoLite camera.

Gravimetric measurements are the most direct method of determining the porosity of solid materials. The experimental value for the scaffold porosity was calculated by gravimetry, taking into account the density of zirconia after sintering. The value found was 5.86 $\pm$ 0.08 g/cm³, which represents 97 % of the

theoretical value. The proper polymer infiltration, after the adhesive curing reaction, was also measured by gravimetry. The free scaffold percentage obtained was practically equivalent to that fixed in the printer setup (49.98 $\pm$ 2.75 %), confirming the good control offered by the advanced printer equipment and robocasting setup. After the polymer infiltration, it decreases substantially and, practically all the empty space is filled by the biocompatible adhesive. The success of polymer infiltration obtained was 87.5 $\pm$ 6.6 % (Table 3-1).

Table 3-1: Porosity of 3D-printed zirconia scaffolds (Eq. 1) and 3D-printed zirconia samples with Bis-GMA/TEGDMA copolymer infiltrated (Eq. 2)

Sample	3D-printed zirconia scaffold	3D-printed zirconia with copolymer infiltrated
	Porosity (%) (Eq. 1)	Infiltration (%) (Eq. 2)
#1	48,76	96,00
#2	45,93	85,00
#3	52,82	92,27
#4	52,02	79,57
#5	50,35	84,65
Average	49.98 $\pm$ 2.75	87.50 $\pm$ 6.56

On contrary, such a percentage of polymer in composite materials is not possible to find by conventional methods. For example, Li et. al. [30] obtained 34.7-46.3 % of porosity after the conventional cold isostatic pressing and sintering process at temperatures varying from 1000 to 1150 ºC. The higher the sintering temperature, the lower porosity was recorded, and therefore, a smaller number of pores were infiltrated. The Bis-GMA/TEGDMA copolymer content achieved, after the infiltration, varied from 12.3% to 18.4%, suggesting that the infiltration of such viscous copolymer is easier with bigger pores. In a recently published review, Bobbert and Zadpoor [45] highlighted the importance to control pore size, porosity, and fiber orientation in synthetic bone

biomedical implants, like autografts, allografts, and xenografts. Such critical parameters affect cell seeding efficiency, cell viability, cell proliferation, and cell differentiation. In this work, by employing the robocasting technology, the porosity of specimens, the pore sizes, and the ceramic filament diameter were designed prior to the ceramic manufacture, and all those critical parameters were conserved after sintering. We have demonstrated that the pores were successfully filled with the methacrylate copolymer (Figure 3-2c-d) and thus, we have obtained the PICN hybrid material. Therefore, the present work represents an advantage and key advance concerning the state-of-art in PICN technologies. The final properties of the resulting hybrid material are expected to be better controlled in comparison with those obtained using conventional methods.

3.3.2   Chemical structure and adhesion of the interpenetrating-polymer network to the 3D-printed ceramic devices

The use of silanization as a process to promote the further deposition and covalent bonding of other layers onto metal surfaces has been extensively reported [46]– [48]. Moreover, organosilane compounds in silica-based ceramics have also been extensively explored and, indeed, the organic-inorganic layer represents a good interface for the further deposition of other coatings [39], [47], [49]. However, silanization studies on zirconia-based ceramics are scarce and, typically, the silane content over zirconia is inferior to those observed for glass substrates. Caravaca et al. [50] have recently reported that the covalent bonding of 3-aminopropyldimethylethoxy silane (APDMES), directly on the surface of zirconia (3Y-TZP), was promoted after sample surface cleaning with cold plasma treatment. In such a study, the aim was to enhance the stability and biointegration of zirconia with the osteoblast-like cells, as an optimization process to obtain biologically compatible dental implants with enhanced biointegration.

Although the adherence of methacrylate polymers is usually good (i.e., they

have been used as the main component in adhesive applications for many years, including dentistry adhesive bonding by photopolymerization), the failure of adhesion has several clinical implications [51]. In the present study, silanization of zirconia has been employed to transform the inert sintered zirconia surface into a functionalized one, and to actuate as a coupling agent for the covalent bonding between Bis-GMA/TEGDMA copolymer and the porous ceramic cubic prototype to prolong the stability of the adhesive layer over time. For this purpose, γ-MPS was chosen as the coupling agent since it forms a stable monolayer with ceramic and metal surfaces, and it is the most used organosilane compound reported for dentistry applications [52]. The presence of terminal carbon-carbon double-bond groups is intended to help the copolymerization with Bis-GMA and TEGDMA monomers, during the radical polymerization steps (Scheme 1).
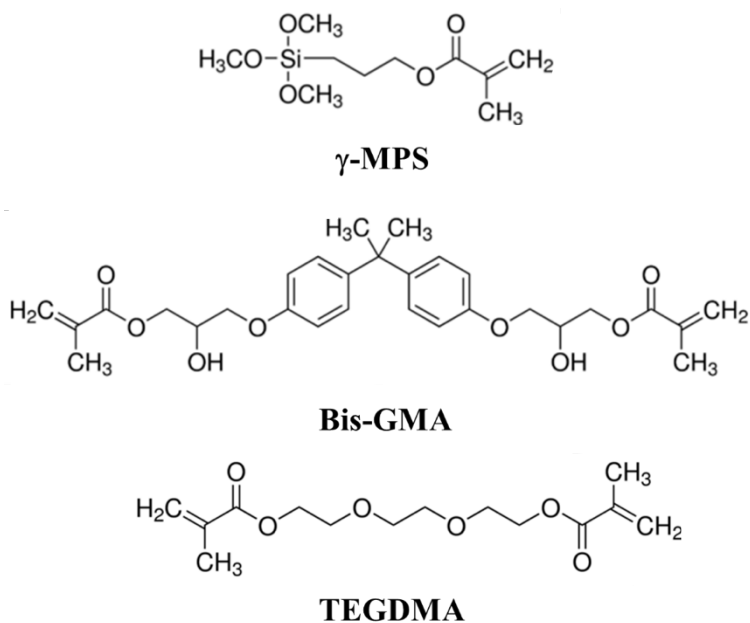
Scheme 1: Chemical structures of organosilane (γ-MPS) and monomers (Bis-GMA and TEGDMA) used for the zirconia functionalization and the preparation of the infiltrated polymer network, respectively.

The presence and successful application of γ-MPS to the zirconia scaffold were detected by XPS analyses. In order to obtain a better understanding of the chemical bonds established after the polymerization reaction, all three modified surfaces of PICN manufacture were analyzed: zirconia scaffolds (3D-printed samples), zirconia scaffolds with γ-MPS silane layer, and zirconia scaffolds with silane monolayer and Bis-GMA/TEGDMA copolymer.

The survey spectra of all three types of samples are represented in Figure 3-4 where a peak representing Si 2p is clearly visible and therefore proves silanization of the 3Y-TZP scaffold. Figure 3-5a represents the XPS high-resolution spectra of 3D-printed zirconia sample after sintering. As it can be seen, two main peaks of Zr–O bonds appear at 181.5 eV and 183.9 eV, corresponding to Zr 3d 5/2 and 3d 3/2 orbitals from ZrO_2 structures [53].
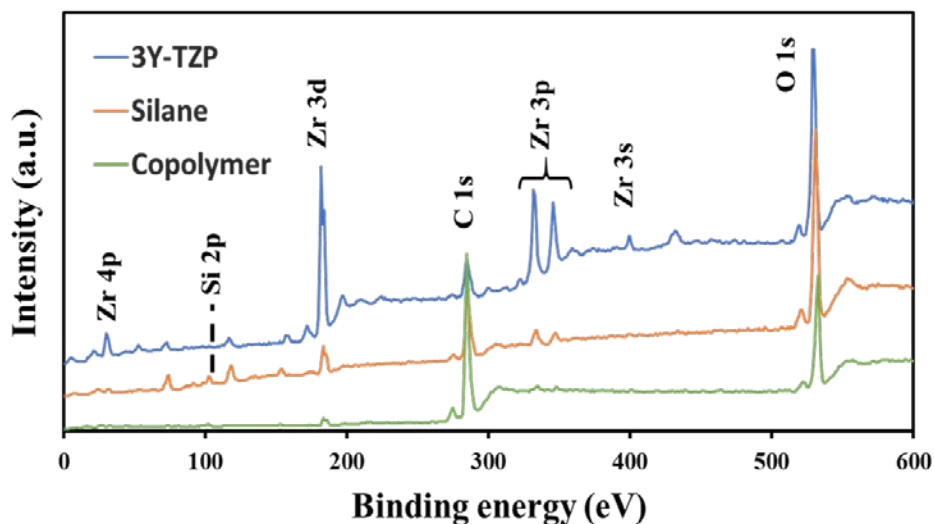
Figure 3-4: Survey XPS spectra of 3D-printed zirconia (3Y-TZP), 3D-printed zirconia with γ-MPS silane monolayer (silane) and 3D-printed zirconia/γ-MPS/Bis-GMA/TEGDMA (copolymer).

A great difference in the Zr 3d binding energies was observed for samples with the γ-MPS layer (Figure 3-5b), which exhibited a shift of +1.13 eV with respect to the pure 3Y-TZP that was attributed to the creation of new Zr–O–Si

bonds on the ceramic surface [54]. The Si 2p and O 1s XPS high-resolution spectra confirm the well-established covalent linkages of Zr–O–Si in the ceramic-silane interface and the Si–C in the interface of silane-copolymer (Figure 3-5). Figure 3-5c represents the binding energies for the 3D-printed sample with silane coating, where the peak at 99.1 eV was attributed to Zr–O–Si bonds [54], and the peak at 102.4 eV was assigned to Si–O–Si, which corresponds to the core of γ-MPS molecules [50], [55]. The detection of Si–O–Si bonds, with higher intensities than those of Zr–O–Si linkages, suggest that an organosilane network is formed on the surface of the 3D-printed zirconia.

For the copolymer infiltrated sample (PICN), the two peaks obtained for Si 2p orbitals (Figure 3-5d) represent uniquely the linkages of γ-MPS with Bis-GMA/TEGDMA structure (Si–C, 104.0 eV) [56], and silane network (Si–O–Si, 102.0 eV) [50], [57]. Si–C peak is quite wide and cannot be distinguished, in case it also covers other Si–O bonds (for example, Si-OH or Si–O–C from hydrolyzed and methylated silane, respectively). Moreover, atomic concentration data (Table 3-2) show that the amount of silane detected for the hybrid ceramic-resin sample (PICN scaffolds) is significantly lower than the amount detected over zirconia functionalized with γ-MPS silane layer (1.15 % and 9.18 %), respectively.

Table 3-2: Atomic concentrations of elements analyzed by XPS for 3D-printed zirconia, 3D-printed zirconia with γ-MPS silane monolayer; and 3D-printed zirconia/γ-MPS/Bis-GMA/TEGDMA copolymer.

Sample	Element	Atomic percentage (%)
3D-printed zirconia scaffolds	C 1s	36.43
	O 1s	42.78
	Zr 3d	20.78
3D-printed zirconia scaffolds with γ-MPS	C 1s	50.89
	O 1s	36.85
	Zr 3d	3.08
	Si 2p	9.18
3D-printed zirconia scaffolds with Bis-GMA/TEGDMA copolymer infiltrated	C 1s	82.57
	O 1s	15.56
	Si 2p	1.15

The establishment of Zr–O–Si linkages on silanized 3D-printed zirconia samples can also be explained when evaluating the O 1s orbital. The pristine sample showed O 1s deconvoluted peaks at 527.5 eV, 529.1 eV, and 530.5 eV, which are mainly associated with Y–O, Zr–O, and O–H bonds, respectively (Figure 3-5g). After silanization, the intensity of the peaks associated with the Zr–O, and O–H bonds (529.1 eV and 530.3 eV, respectively) decreases and a new linkage related to Si–O–Si siloxane bonds appears at 531.4 eV (Figure 3-5) [58]. The PICN surface presents a little variation on the O1s neighborhood, where a much higher contribution of C–O–C/O–H, C–O/C=O bonds (532.6 eV, Figure 3-5i), belonging to the methacrylate copolymer (Bis-GMA/TEGDMA) coating, was achieved and less Si–O–C bonds were detected [59] Figure 3-5e,f represent the C 1s spectra of silanized and PICN samples. The silanized sample (Figure 3-5e) displays four main peaks at 282.1, 284.5, 286.6, and 288.6 eV, which have been attributed to the Si–C bond from the silanization, and the C–C, C–O, and

C=O bonds of γ-MPS molecule [60], [61], respectively. For the Bis-GMA/TEGDMA infiltrated sample (Figure 3-5f), the C 1s spectrum deconvolution is similar to that of the silanized sample, showing four peaks at 283.2 eV (Si–C), 284.5 (C–C), 286.1 (C–O), 288.5 (C=O), in accordance to previous reports [62], [63]. Small differences are observed in the relative intensities of the peaks detected for the PICN with respect to that of the silanized samples. Thus, the relative intensity for peaks associated with Si–C, and C–C bonds are slightly lower for the former sample than for the latter one, while the opposite effect occurs for the peak of the C–O bonds originating from the copolymer. In a conclusion, the correlation among high-resolution spectra of Zr 3d, Si 2p and O 1s proves that γ-MPS is adhered to the zirconia surface, actuating as a coupling agent for the adhesion of the methacrylate copolymer resin. The survey spectrum for each sample is shown in Figure 3-4 and Table 3-2 lists the atomic percentage of Zr 3d, Si 2p, O 1s, and C1s atoms.
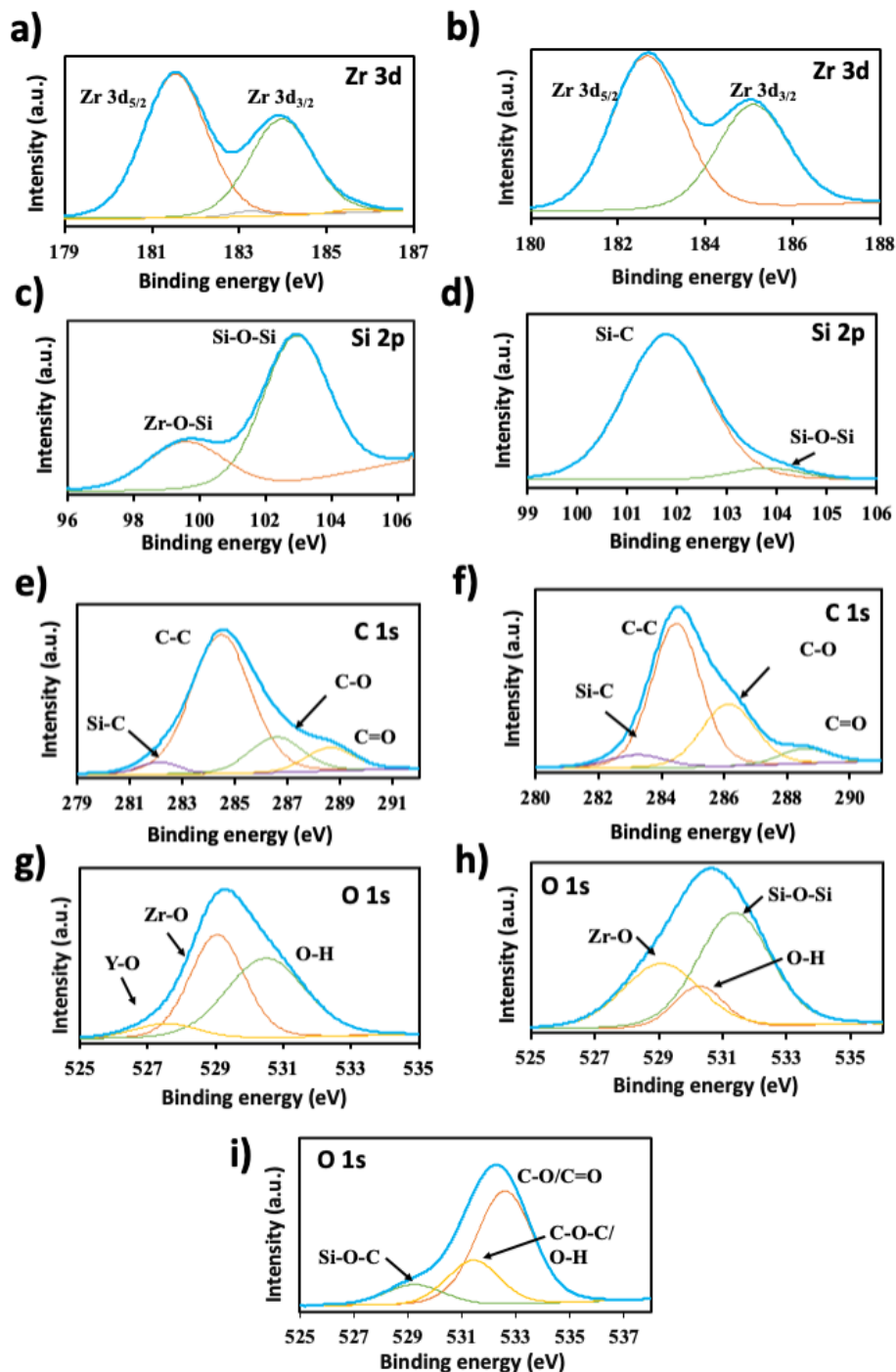
Figure 3-5: XPS high-resolution spectra of: (a, b) Zr 3d; (c, d) Si 2p; (e, f) C 1s; and (g-i) O 1s. Samples identification: 3D-printed zirconia platforms (a, e); 3D-printed zirconia with γ-MPS silane monolayer (b, c, f); and PICN scaffolds (d, g).

The copolymer adhesion was investigated by Raman and SEM analyses. For this characterization, the 40:60 Bis-GMA/TEGDMA ratio was chosen as the most suitable proportion for the zirconia pore infiltration. Figure 3-6a shows a 3D map of the PICN side zone after cutting and polishing it until a satisfying surface finishing was reached. The Raman image identifies the main regions in the cubic section of the sample with a 40:60 Bis-GMA/TEGDMA copolymer. It clearly evidences the infiltration of the polymer inside of the pores. As it can be seen, the mapping analysis enables discrimination between the different components of the hybrid material according to their nature. The red color represents the copolymer, while the green color shows the single filaments of a 3D-printed structure. Raman mapping analysis allowed the identification of the main absorption bands of the 40:60 Bis-GMA/TEGDMA copolymer and the 3Y-TZP zirconia scaffold is displayed in Figures 3-6b and 3-6c, respectively. The Raman shift of the copolymer was previously reported [61], and the main absorption bands are associated with C=C, C=O, =C-H, and C-H groups. Furthermore, 3Y-TZP absorption bands from 100 to 1100 cm^{-1} correspond to the standard representation of sintered 3Y-TZP zirconia reported in the literature [64], [65]. The 3Y-TZP sintered samples showed to adopt mostly the tetragonal phase with characteristic sharp bands of the different Raman modes at approximately 145, 263, 320, 465, 612, and 643 cm^{-1} (Figure 3-6c). Further characterization of the other copolymer ratios studied in the present work is described below and the results correspond with the previous report on the material [66].
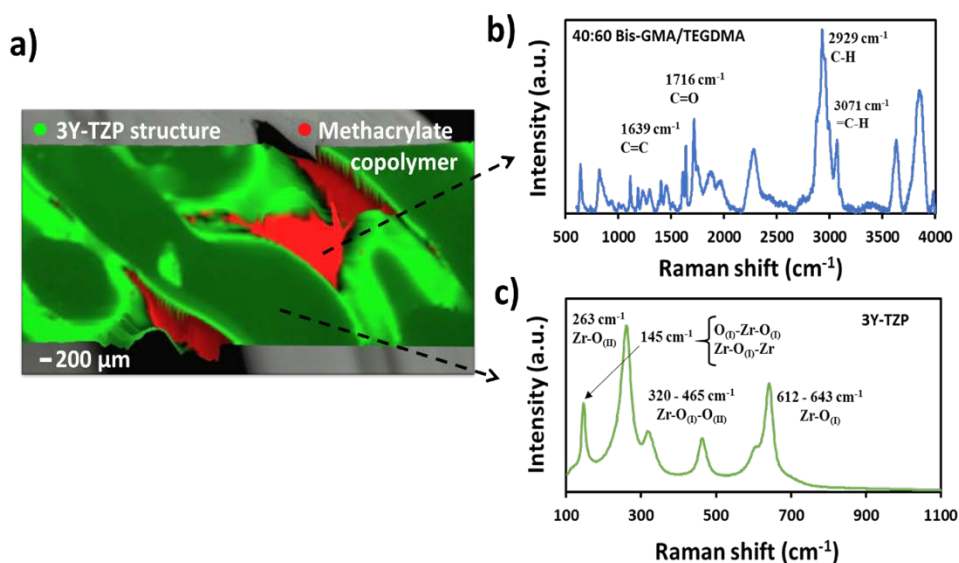
Figure 3-6: (a) Confocal 3D mapping of copolymer-infiltrated cubic sample (in green, are visible zirconia filaments and in red the copolymer inside of the pores). Raman spectra of: (b) the 40:60 Bis-GMA/TEGDMA copolymer, and (c) the 3Y-TZP zirconia structure.

Figure 3-7 represents the FTIR spectra of different Bis-GMA/TEGDMA copolymer ratios (50:50, 40:60, and 30:70) tested for the infiltration of ceramic scaffolds. Comparison of such spectra allows a better understanding of copolymerization reaction and composition reached for each ratio. The wide peaks at 3444 cm^{-1} and 2920 cm^{-1} correspond to the hydroxyl groups and C–H stretching, respectively, from aromatic rings of the Bis-GMA monomer. The broad peak at 2920 cm^{-1} also includes methylene and methyl groups of the copolymer. The 1714 cm^{-1} absorption band is attributed to the carbonyl group from ester linkages in the Bis-GMA and TEGDMA monomers. The peaks at ~1634 cm^{-1}, which belong to aliphatic C=C double bonds, indicate the success of the copolymerization reaction. Aromatic double C=C bonds attributed to the Bis-GMA monomer are represented by a peak at 1507 cm^{-1}. The multiple peaks at 1294, 1244, and 1162 cm^{-1} represent the C–O stretching bands from ether linkages on TEGDMA units [60].
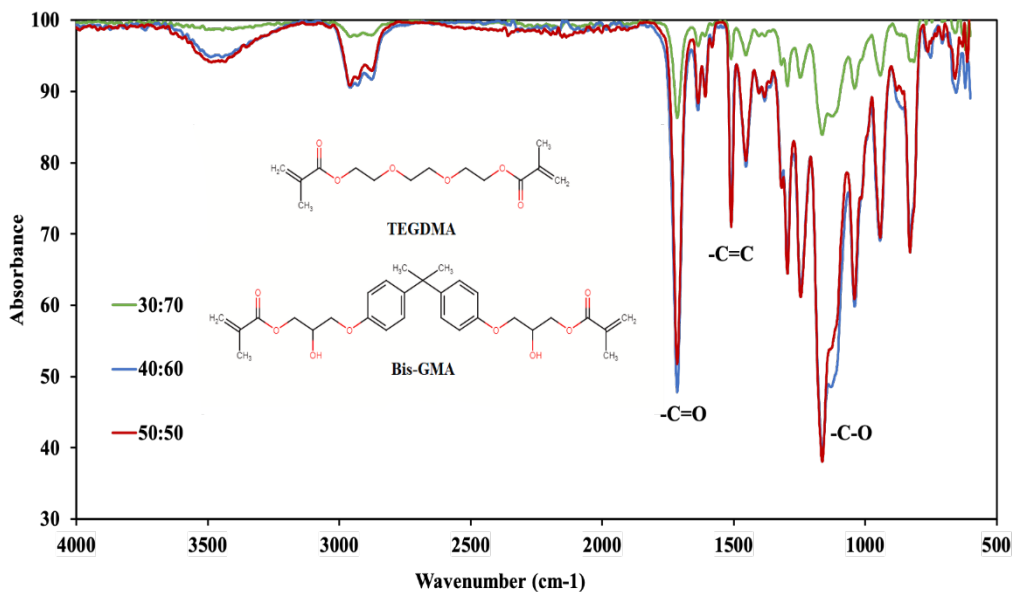
Figure 3-7: FTIR spectra of three copolymers prepared using different monomer ratios. The functional groups associated to the Bis-GMA and TEGDMA units depend on the copolymer ratio.

These findings are also supported by the Raman spectra, which are shown in Figure 3-8. As discussed above for FTIR spectra, the intensity of the aliphatic C=C double bond at 1637 cm^{-1} increases with the amount of Bis-GMA in the copolymer. The intensity of the peak at 2931 cm^{-1} also increases with the amount of Bis-GMA in the copolymer. Thus, the latter absorption band is associated with the methyl groups, as the Bis-GMA monomer has twice as many CH_3 groups in comparison to the TEGDMA unit. The detected functional groups correspond and are consistent with previous studies.[61] [62]
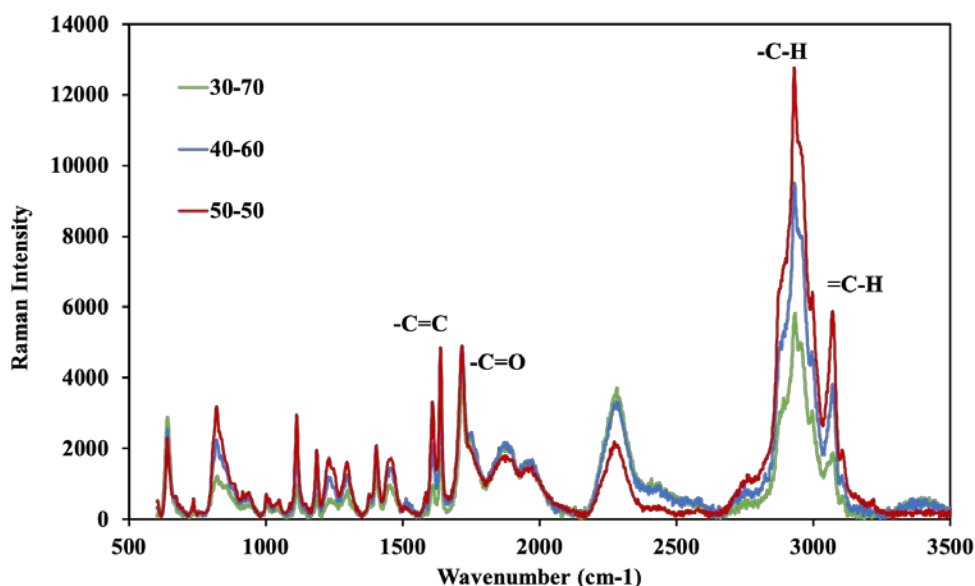
Figure 3-8: Raman spectra of Bis-GMA/TEGDMA copolymers prepared using 30:70, 40:60 and 50:50 ratios. The spectra show visible differences, depending on monomers ratios.

The behavior of the copolymer with temperature was examined using differential scanning calorimetry. Figure 3-9a indicates that, although the Tg of all copolymers is approximately -60 °C, this parameter experiences a slight increase with the amount of Bis-GMA. This has been attributed to the mobility of the latter monomer, which is lower than that of TEGDMA. This low mobility of Bis-GMA is caused by the presence of two benzene rings and multiple hydrogen bonds, the latter promoting the formation of strong intermolecular forces among the molecules.[63]

Thermogravimetric analysis in Figure 3-9b clearly shows a two-step degradation. The first degradation weight loss, which occurs at 311 °C is assigned to a non-homogenous network and, possibly, the formation of primary cycles. This is followed by the second step at 395 °C, in which the main copolymer network broke down.[67] The copolymer is completely degraded at

600 °C. The two decomposition steps were very similar for all copolymer ratios, evidencing that monomers have reacted in the proper way.[60]
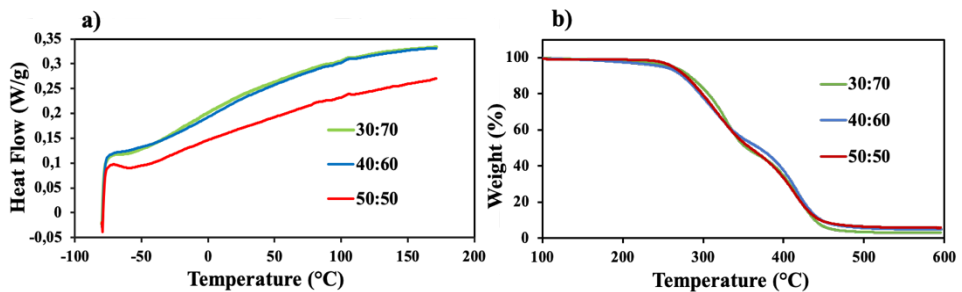
Figure 3-9: (a) DSC and (b) TGA curves for the copolymers prepared using three Bis-GMA/TEGDMA copolymer ratios.

As mentioned before, the main aim of this work was to achieve successful infiltration of the ceramic scaffold with methacrylate resin to obtain stable structures for future dental applications. As well known, dental implants manufactured with ceramic material are generally considered to be hard and brittle in nature [29]. Ceramics can be toughened by reinforcement with other materials [68], [69]. The polymer adhesive is intended to toughen the porous zirconia scaffold by reinforcing its filaments and amortizing the impact or tensions generated over the long time-implanted prosthesis.

SEM micrographs displayed in Figure 3-10 demonstrate the properly infiltrated pores (Figure 3-10a) and the excellent adhesion in copolymer-zirconia interfaces (Figure 3-10b). The lack of gaps or vacancies at the interface points (Figure 3-10b) is observed, even after mechanical manipulation of the sample (cutting and polishing treatment). This result supports our strategy of silanization and further Bis-GMA/TEGDMA deposition for the preparation of the PICN devices, in terms of two-stage synthesis and without additional surface

activation. The proposed strategy represents an easy method to reinforce hollow 3D-printed zirconia scaffolds.
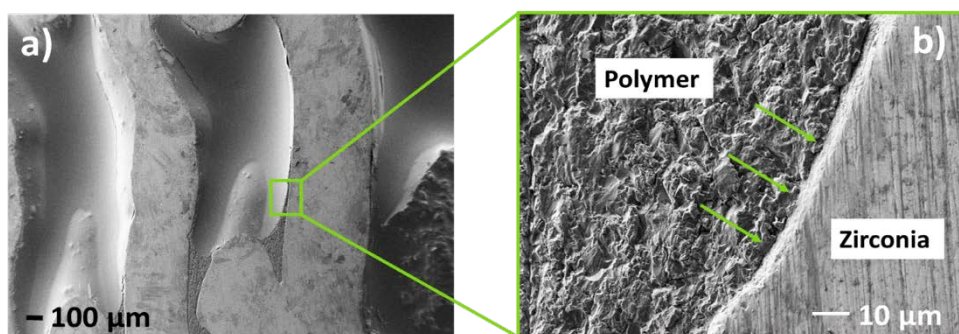
Figure 3-10: SEM micrographs of PICN samples, proving the adhesion and infiltration of pores by Bis-GMA/TEGDMA deposition after silanization: a) low magnification image of two infiltrated pores; and b) high magnification image of the polymer-ceramic interface.

3.3.3   Compression test

As the mechanical performance of a dental implant is an important aspect of a material design, the compression strength of the specimen was measured. The compression strength of zirconia scaffolds was compared with the PICN sample and with a sample printed with 100% infill of zirconia filaments. The behavior of specimens, while undergoing compression was recorded in the means of stress-strain curves, which are displayed in Figure 3-11. Due to the morphology of the 3D-printed cubic samples, it was not possible to obtain homogeneous height curves. Therefore, the data were recorded until a breakage or load limit of ~7 kN. There is a significant difference between the three samples, as can be seen by the photographs of pieces after being broken under pressure load (Figure 3-11, inset). In the case of zirconia scaffold without polymer infiltrated (Figure 3-11, blue curve), the cube loses its mechanical integrity at only 2.1 % of elongation at break (ε) and the strength resistance diminishes. On the other hand, in the case of PICN samples, it resisted to start breaking until 3 % of ε, whereas the pieces resist the stress force applied (Figure 3-11, red curve). The drops along

the curve show breakage of small parts of the PICN sample, especially in corners, but the core of the infiltrated sample stays undamaged even at 7 kN. This fact demonstrates that the mechanical properties can be compared with samples with 100% infill cubic structure (Figure 3-11, green curve).
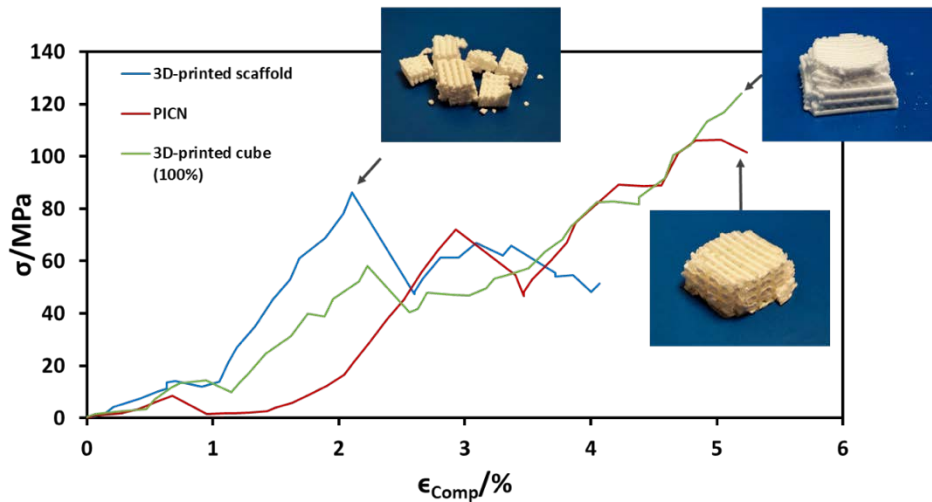
Figure 3-11: Stress-strain curves obtained after the compression test, at 0.5 mm/s of pressure rate, for the 3D-printed zirconia scaffold, 3D-printed zirconia with copolymer infiltrated (PICN sample), and 3D-printed cube with 100 % infill of zirconia filaments. Insets: photographs taken after the pieces ruptures or until reaching the pressure force of 7 kN.

3.3.4   Antimicrobial activity of PICN devices

In this study, we are combining three different materials: a zirconia substrate, an organic-inorganic anchoring molecule, and a copolymer adhesive. Each one has different surface properties and different behavior over bacteria proliferation. The organosilane compound is supposed to not be in direct contact with saliva, therefore, its bacterial property is of less importance. However, with time, saliva can penetrate the abutment of zirconia and reach the titanium screw implants under the zirconia abutment. *Streptococcus salivarius* is one of the microorganisms present in saliva and responsible for dental caries [70], whereas *Escherichia coli* is the most commonly used type of

Gram-negative bacterial line and is considered a model organism in microbiological studies [71]. Such microorganisms were chosen to evaluate the bacterial activity on the new material.

Therefore, to ensure the possible application of the new composite in the biomedical field, the antimicrobial activity and bacteria adhesion of all stages of the composite preparation were tested. Figure 3-12 summarizes the antimicrobial behaviour of each sample. The control, which was the same as for the proliferation or adhesion tests, consisted of bacteria seeded in sterile vials (i.e., without additional materials) using optimal conditions for promoting their growth. As expected, zirconia scaffolds showed lower bacterial growth than the control (Figure 3-12a), due to their inert structure, as previously reported by El-Ghany and Sherief [72]. On the other hand, 3D-printed scaffolds with γ-MPS silane monolayer and PICN samples did not experience significant changes after 24 h of bacteria incubation. However, the *S. salivarius* bacteria colonies rose slightly on this hydrophilic surface compared to the *E. coli* organisms and the control (Figure 3-12a), showing a preference for this compound. On other hand, the error deviation is also high in *S. salivarius*, suggesting that such results should be taken carefully [52]. The 3D-printed structures with infiltrated polymer showed similar relative viability of bacteria growth in either *S. salivarius* or *E. coli* media.
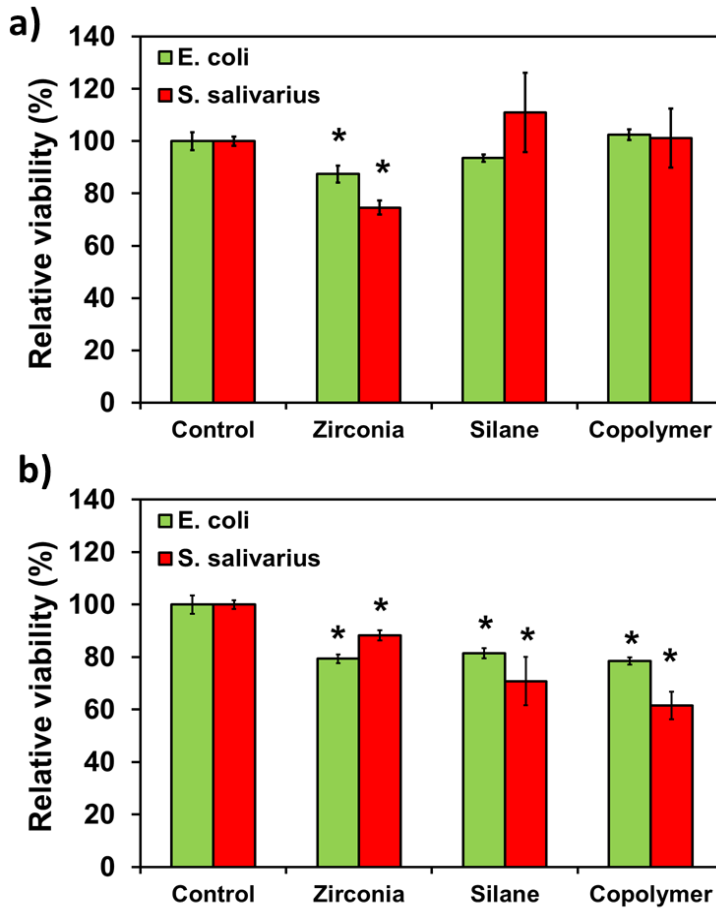
Figure 3-12: Antimicrobial activity of composites tested with E. coli and S salivarius bacterial lines for plane zirconia scaffolds (marked as Zirconia), scaffolds coated with γ-MPS (marked as Silane) and PICN scaffolds (marked as Copolymer): a) bacterial growth and b) bacterial adhesion, both recorded after 24h. Results marked with stars are confidence level where p <0.05, using the Student's T-test.

On contrary, *E. coli* proliferation is higher in silane and copolymer surfaces than *S. salivarius* microorganisms (Figure 3-12b). It was also evidenced in the SEM images (Figure 3-13 and Figure 3-14). Bacteria growth is favored by the media, whereas bacteria adhesion depends on several factors: surface roughness, material hydrophilicity, presence of charges, superficial tension, and others.

In general, the bacteria proliferation on the surface of any of the studied samples was found to be limited, the lowest values being obtained for the 3D-

printed zirconia substrate with Bis-GMA/TEGDMA copolymer coating (78.5 ± 1.3 % and 61.6 ± 5.2 % in *E. coli* and *S. salivarius*, respectively).

In the case of the zirconia scaffolds alone, the antimicrobial behaviour observed from growth and adhesion tests was similar [72]. However, the *S. salivarius* proliferation increases in 24 h due to the preference of such microorganisms for rough surfaces. The roughest surface of zirconia filaments (Figure 3-2b) usually promotes microorganism adhesion compared to polymer smooth surfaces. After zirconia filaments covering with the copolymer, such proliferation decreases (Figure 3-12b), proving that filaments are well coated by the copolymer.
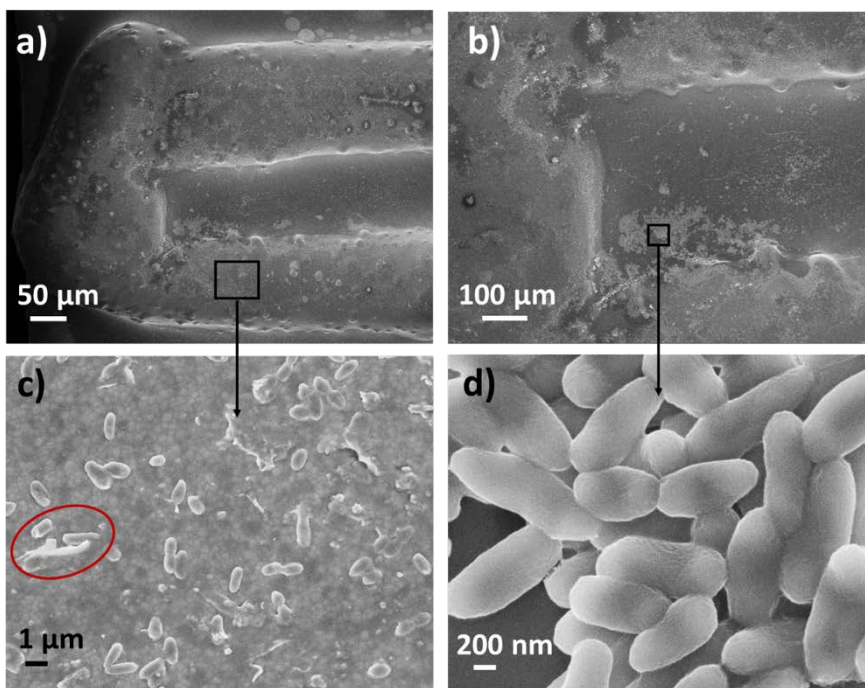
Figure 3-13: SEM micrographs of E. coli colony at the surface of PICN sample: a) overview of filaments and pores covered by copolymer (low magnification, ×100), b) higher magnification of image a) (×250), c) microorganism growth on zirconia filaments (×10000), and d) microorganism growth on scaffold pores (×50000). The red circle in image c) shows one example of bacteria inside filament micropores.

Careful evaluation of the copolymer samples allowed discrimination between *E. coli* and *S. salivarius*, the former showing a slightly higher adhesion of *E. coli* bacteria than the latter. SEM micrographs of *E. coli* bacteria attached to the surface of the composite (Figure 3-13a-d) reveal that the copolymer forms a small valley between the filaments in which the colonies of bacteria are mostly accumulated. Another important observation is that bacteria can proliferate inside some of the superficial micropores of the zirconia filaments, supposedly not fully covered by the adhesive (Figure 3-13c, circle inside), making difficult their removal. If SEM micrographs at low magnification, from filaments and pores covered by the adhesive and incubated in *E. coli* and *S. salivarius*, respectively, are compared (Figure 3-13b and Figure 3-14b), big colonies are mostly observed inside valleys.
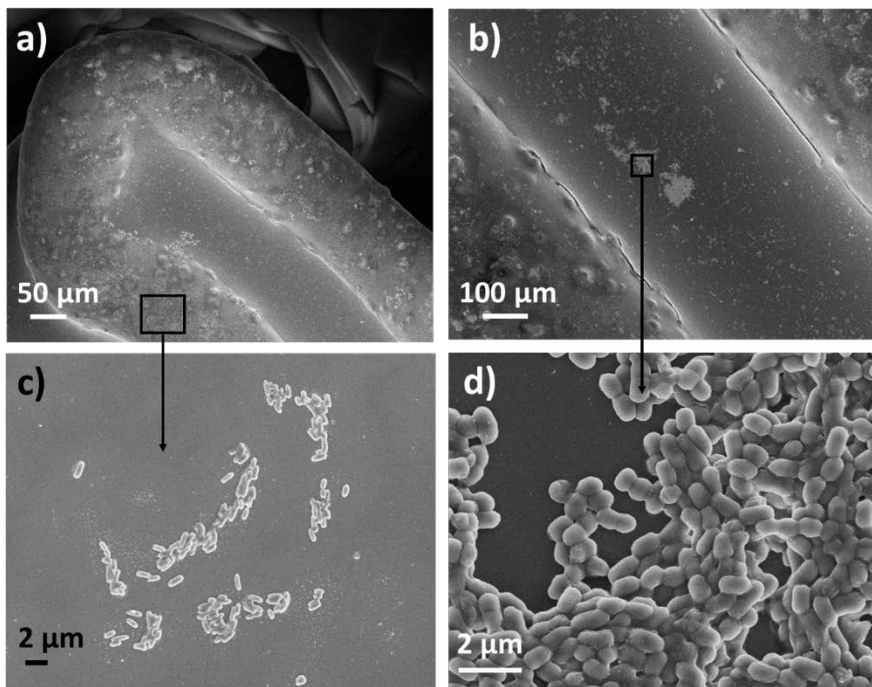
Figure 3-14: SEM micrographs of S. salivarius colony at the surface of PICN sample: a) overview of filaments and pores covered by copolymer (low magnification, ×100), b) higher magnification of image a) (×250), c) microorganism growth on zirconia filaments (×5000), and d) microorganism growth on scaffold pores (×15000).

Thus, SEM images prove that the topography of the samples has a remarkable influence on bacteria proliferation. Our results demonstrate that the antimicrobial properties of 3Y-TZP infiltrated with Bis-GMA/TEGDMA are similar to those of pure zirconia, which make it a suitable hybrid material for the medical field [50], [73]. Studies on cell proliferation and cell adhesion, with osteoblast MG-63 cells, to observe the biocompatibility of the new system will be presented in the next Chapter.

3.4   Conclusions

In this work, the feasibility of fabrication of dimensionally stable and highly porous zirconia scaffolds (50 % of voids) by combining two technologies, robocasting manufacturing, and polymer-infiltrated ceramic network, has been proved. The use of a high-tech 3D-printer, with precise control over the ink paste deposition, was the key to the success achieved with cubic geometry processing and stability, containing 49.98 ± 2.75 % of pores among ceramic filaments. After the sintering step, a reduction of only 20 % of the original printed dimensions, with no mismatch in the compactness of the ZrO_2 filaments was observed by digital images.

Another successful strategy was to promote the adhesion of Bis-GMA/TEGDMA copolymer (40:60 ratio) by the previous functionalization of the 3Y-TZP filaments with γ-MPS organosilane compound. The pores of the 3D-printed scaffolds were almost completely filled, obtaining an infiltration density of 87.50 ± 6.56 %, which is not possible to reach with conventional ceramic production methods. The filaments are well impregnated by the copolymer, as checked by optical and SEM analyses, and the polymer infiltrated scaffold is more resistant to filament rupture if compared to the non-infiltrated one, as demonstrated by the compression test. The scaffold architecture plays an important role in bacteria adhesion and proliferation. The novel zirconia

scaffolds prepared using polymer-infiltrated ceramic network and 3D-printing technologies exhibit antimicrobial properties similar to that of 3Y-TZP, as has been demonstrated by the adhesion and proliferation tests with *E. coli* and *S. salivarius* bacteria. This study is the preliminary approach to exploring the cell viability and mechanical properties of the new scaffold composite for dental implants. Therefore, this second part of the project will be presented in the next Chapter.

3.5   References

[1]   B. Berman, "3-D printing : The new industrial revolution," *Business Horizons*, vol. 55, no. 2, pp. 155–162, 2012, doi: 10.1016/j.bushor.2011.11.003.

[2]   B. T. Wittbrodt *et al.*, "Life-cycle economic analysis of distributed manufacturing with open-source 3-D printers," *Mechatronics*, vol. 23, no. 6, pp. 713–726, 2013, doi: 10.1016/j.mechatronics.2013.06.002.

[3]   M. Kasparova, L. Grafova, P. Dvorak, T. Dostalova, A. Prochazka, and H. Eliasova, "Possibility of reconstruction of dental plaster cast from 3D digital study models," *BioMedical Engineering Online*, vol. 12, pp. 1–11, 2013.

[4]   J. W. Stansbury and M. J. Idacavage, "3D printing with polymers: Challenges among expanding options and opportunities," *Dental Materials*, vol. 32, no. 1, pp. 54–64, 2016, doi: 10.1016/j.dental.2015.09.018.

[5]   L. C. Hwa, S. Rajoo, A. M. Noor, N. Ahmad, and M. B. Uday, "Recent advances in 3D printing of porous ceramics: A review," *Current Opinion in Solid State and Materials Science*, vol. 21, no. 6, pp. 323–347, 2017, doi: 10.1016/j.cossms.2017.08.002.

[6]   G. B. Brown, G. Fräns Currier, O. Kadioglu, and J. P. Kierlb, "Accuracy of 3-dimensional printed dental models reconstructed from digital intraoral impressions," *American Journal of Orthodontics and Dentofacial Orthopedics*, vol. 154, pp. 733–739, 2018, doi: 10.1016/j.ajodo.2018.06.009.

[7]   A. Dawood, B. M. Marti, V. Sauret-Jackson, and A. Darwood, "3D printing in dentistry," *British Dental Journal*, vol. 219, no. 11, pp. 521–529, 2015, doi: 10.1038/sj.bdj.2015.914.

[8]   M. Juneja, N. Thakur, D. Kumar, A. Gupta, B. Bajwa, and P. Jindal, "Accuracy in dental surgical guide fabrication using different 3-D printing techniques," *Additive Manufacturing*, vol. 22, no. May, pp. 243–255, 2018, doi: 10.1016/j.addma.2018.05.012.

[9]   A. Awad, F. Fina, A. Goyanes, S. Gaisford, and A. W. Basit, "3D printing: Principles and pharmaceutical applications of selective laser sintering," *International Journal of Pharmaceutics*, vol. 586, no. June, p. 119594, 2020, doi: 10.1016/j.ijpharm.2020.119594.

[10]   K. Shah and D. J. Lee, "Fabricating a screw-retained, complete arch, fixed implant prosthesis using selective metal laser sintering: A clinical report," *Journal of Prosthetic Dentistry*, vol. 123, no. 3, pp. 373–378, 2020, doi: 10.1016/j.prosdent.2019.01.013.

[11]   M. Antanasova, A. Kocjan, M. Hočevar, and P. Jevnikar, "Influence of surface airborne-particle abrasion and bonding agent application on porcelain bonding to titanium dental alloys fabricated by milling and by selective laser melting," *Journal of Prosthetic Dentistry*, vol. 123, no. 3, pp. 491–499, 2020, doi: 10.1016/j.prosdent.2019.02.011.

[12]   S. Baumgartner, R. Gmeiner, J. A. Schönherr, and J. Stampfl, "Stereolithography-based additive manufacturing of lithium disilicate glass ceramic for dental applications," *Materials Science and Engineering C*, vol. 116, no. June, p. 111180, 2020, doi: 10.1016/j.msec.2020.111180.

[13]   J. A. Schönherr, S. Baumgartner, M. Hartmann, and J. Stampfl, "Stereolithographic additive manufacturing of high precision glass ceramic parts," *Materials*, vol. 13, no. 7, pp. 5–7, 2020, doi: 10.3390/ma13071492.

[14]   F. Chen *et al.*, "Preparation and biological evaluation of ZrO2 all-ceramic teeth by DLP technology," *Ceramics International*, vol. 46, no. 8, pp. 11268–11274, 2020, doi: 10.1016/j.ceramint.2020.01.152.

[15]   J. Zhang, Q. Hu, S. Wang, J. Tao, and M. Gou, "Digital light processing based three-dimensional printing for medical applications," *International Journal of Bioprinting*, vol. 6, no. 1, pp. 12–27, 2020, doi: 10.18063/ijb.v6i1.242.

[16]   M. Goldberg *et al.*, "The Influence of Co Additive on the Sintering, Mechanical Properties, Cytocompatibility, and Digital Light Processing Based Stereolithography of 3Y-TZP-5Al2O3 Ceramics," *Materials*, vol. 13, p. 2789, 2020, doi: doi:10.3390/ma13122789.

[17]   J. Li, J. Hu, Y. Zhu, X. Yu, M. Yu, and H. Yang, "Surface roughness control of root analogue dental implants fabricated using selective laser melting," *Additive Manufacturing*, vol. 34, no. April, p. 101283, 2020, doi: 10.1016/j.addma.2020.101283.

[18]   D. Zhang, E. Peng, R. Borayek, and J. Ding, "Controllable Ceramic Green-Body Configuration for Complex Ceramic Architectures with Fine Features," *Advanced Functional Materials*, vol. 29, no. 12, pp. 1–12, 2019, doi: 10.1002/adfm.201807082.

[19]   A. C. Branco *et al.*, "Suitability of 3D printed pieces of nanocrystalline zirconia for dental applications," *Dental Materials*, vol. 36, no. 3, pp. 442–455, 2020, doi: 10.1016/j.dental.2020.01.006.

[20]   H. N. Chia and B. M. Wu, "Recent advances in 3D printing of biomaterials," *Journal of Biological Engineering*, vol. 9, no. 1, pp. 1–14, 2015, doi: 10.1186/s13036-015-0001-4.

[21]   H. O. T. Ware *et al.*, "High-speed on-demand 3D printed bioresorbable vascular scaffolds," *Materials Today Chemistry*, vol. 7, pp. 25–34, 2018, doi: 10.1016/j.mtchem.2017.10.002.

[22]   R. S. Brum *et al.*, "Polymer coatings based on sulfonated-poly-ether-ether-ketone films for implant dentistry applications," *Journal of Materials Science: Materials in Medicine*, vol. 29:132, no. 8, p. 1 of 9, 2018, doi: 10.1007/s10856-018-6139-0.

[23]   D. Zhang *et al.*, "A 3D-printing method of fabrication for metals, ceramics, and multi-materials using a universal self-curable technique for robocasting," *Materials Horizons*, vol. 7, no. 4, pp. 1083–1090, 2020, doi: 10.1039/c9mh01690b.

[24]   R. D. Farahani, K. Chizari, and D. Therriault, "Three-dimensional printing of freeform helical microstructures: A review," *Nanoscale*, vol. 6, no. 18, pp. 10470–10485, 2014, doi: 10.1039/c4nr02041c.

[25]   M. Tilton, G. S. Lewis, H. Bok Wee, A. Armstrong, M. W. Hast, and G. Manogharan, "Additive manufacturing of fracture fixation implants: Design, material characterization, biomechanical modeling and

experimentation," *Additive Manufacturing*, vol. 33, no. March, p. 101137, 2020, doi: 10.1016/j.addma.2020.101137.

[26]   S. J. Bonsor and G. J. Pearson, *A clinical guide to applied dental materials*. Elsevier/Churchill Livingstone, 2013.

[27]   T. Maridurai, D. Balaji, and S. Sagadevan, "Synthesis and characterization of yttrium stabilized zirconia nanoparticles," *Materials Research*, vol. 19, no. 4, pp. 812–816, 2016, doi: 10.1590/1980-5373-MR-2016-0196.

[28]   A. Jonhson, P. Sinthuprasirt, H. Fathi, and S. Pollington, "Current Glass-Ceramic Systems Used in Dentistry," in *Current Trends on Glass and Ceramic Materials*, S. H. Nandyala and J. Dos Santos, Eds. Sharjak: Bentham Science Publishers, 2013, pp. 49–72.

[29]   J. W. Ruh, Robert; Adams, "Yttria-Stabilized Zirconia versus Temperature," *Journal of Americal Ceramic Society*, vol. 80, no. 4, pp. 903–908, 1997.

[30]   J. Li *et al.*, "Mechanical performance of polymer-infiltrated zirconia ceramics," *Journal of Dentistry*, vol. 58, pp. 60–66, 2017, doi: 10.1016/j.jdent.2017.01.008.

[31]   K. Srigurunathan, R. Meenambal, A. Guleria, D. Kumar, J. M. D. F. Ferreira, and S. Kannan, "Unveiling the Effects of Rare-Earth Substitutions on the Structure, Mechanical, Optical, and Imaging Features of ZrO2 for Biomedical Applications," *ACS Biomaterials Science and Engineering*, vol. 5, no. 4, pp. 1725–1743, 2019, doi: 10.1021/acsbiomaterials.8b01570.

[32]   M. Guazzato, M. Albakry, L. Quach, and M. V. Swain, "Influence of surface and heat treatments on the flexural strength of a glass-infiltrated alumina/zirconia-reinforced dental ceramic," *Dental Materials*, vol. 21, no. 5, pp. 454–463, May 2005, doi: 10.1016/j.dental.2004.07.010.

[33]   L.-H. He and M. Swain, "A novel polymer infiltrated ceramic dental material," *Dental Materials*, vol. 27, no. 6, pp. 527–534, 2011, doi: 10.1016/j.dental.2011.02.002.

[34]   A. Coldea, M. V. Swain, and N. Thiel, "In-vitro strength degradation of dental ceramics and novel PICN material by sharp indentation," *Journal of the Mechanical Behavior of Biomedical Materials*, vol. 26, pp. 34–42, 2013, doi: 10.1016/j.jmbbm.2013.05.004.

[35]   A. Coldea, M. V. Swain, and N. Thiel, "Mechanical properties of polymer-infiltrated-ceramic-network materials," *Dental Materials*, vol. 29, no. 4, pp. 419–426, 2013, doi: 10.1016/j.dental.2013.01.002.

[36]   M. V. Swain, A. Coldea, A. Bilkhair, and P. C. Guess, "Interpenetrating network ceramic-resin composite dental restorative materials," *Dental Materials*, vol. 32, no. 1, pp. 34–42, 2016, doi: 10.1016/j.dental.2015.09.009.

[37]   J. E. Smay, G. M. Gratson, R. F. Shepherd, J. Cesarano, and J. A. Lewis, "Directed colloidal assembly of 3D periodic structures," *Advanced Materials*, vol. 14, no. 18, pp. 1279–1283, 2002, doi: 10.1002/1521-4095(20020916)14:18<1279::AID-ADMA1279>3.0.CO;2-A.

[38]   D. Therriault, R. F. Shepherd, S. R. White, and J. A. Lewis, "Fugitive inks for direct-write assembly of three-dimensional microvascular networks," *Advanced Materials*, vol. 17, no. 4, pp. 395–399, 2005, doi: 10.1002/adma.200400481.

[39]   I. D. Sideridou and M. M. Karabela, "Effect of the amount of 3-methacyloxypropyltrimethoxysilane coupling agent on physical properties of dental resin nanocomposites," *Dental Materials*, vol. 25, no. 11, pp. 1315–1324, 2009, doi: 10.1016/j.dental.2009.03.016.

[40]   B. Chen *et al.*, "Effectiveness of pre-silanization in improving bond performance of universal adhesives or self-adhesive resin cements to silica-based ceramics: Chemical and in vitro evidences," *Dental Materials*, vol. 35, no. 4, pp. 543–553, 2019, doi: 10.1016/j.dental.2019.01.010.

[41]   M. Kumaresan, K. Vijai Anand, K. Govindaraju, S. Tamilselvan, and V. Ganesh Kumar, "Seaweed Sargassum wightii mediated preparation of zirconia (ZrO2) nanoparticles and their antibacterial activity against gram positive and gram negative bacteria," *Microbial Pathogenesis*, vol. 124, no. August, pp. 311–315, 2018, doi: 10.1016/j.micpath.2018.08.060.

[42]   A. I. Hussein, "Bacterial Adhesion on Zirconia, Lithium Desilicated and Gold Crowns-In Vivo Study," *Advances in Dentistry and Oral Health*, vol. 1, no. 5, pp. 105–107, 2016, doi: 10.19080/adoh.2016.01.555574.

[43]   A. Accardo *et al.*, "Multiphoton Direct Laser Writing and 3D Imaging of Polymeric Freestanding Architectures for Cell Colonization," *Small*, vol. 13, no. 27, pp. 1–11, 2017, doi: 10.1002/smll.201700621.

[44]   J. Schweiger, D. Bomze, and M. Schwentenwein, "3D Printing of Zirconia–
        What is the Future?," *Current Oral Health Reports*, vol. 6, no. 4, pp. 339–
        343, 2019, doi: 10.1007/s40496-019-00243-4.

[45]   F. S. L. Bobbert and A. A. Zadpoor, "Effects of bone substitute
        architecture and surface properties on cell response, angiogenesis, and
        structure of new bone," *Journal of Materials Chemistry B*, vol. 5, no. 31,
        pp. 6175–6192, 2017, doi: 10.1039/c7tb00741h.

[46]   V. Dalmoro, J. H. Z. dos Santos, E. Armelin, C. Alemán, and D. S. Azambuja,
        "A synergistic combination of tetraethylorthosilicate and
        multiphosphonic acid offers excellent corrosion protection to AA1100
        aluminum alloy," *Applied Surface Science*, vol. 273, pp. 758–768, May
        2013, doi: 10.1016/j.apsusc.2013.02.131.

[47]   J. I. Iribarren-Mateos, I. Buj-Corral, J. Vivancos-Calvet, C. Alemán, J. I.
        Iribarren, and E. Armelin, "Silane and epoxy coatings: A bilayer system to
        protect AA2024 alloy," *Progress in Organic Coatings*, vol. 81, pp. 47–57,
        2015, doi: 10.1016/j.porgcoat.2014.12.014.

[48]   V. Dalmoro, D. S. Azambuja, C. Alemán, and E. Armelin, "Hybrid
        organophosphonic-silane coating for corrosion protection of magnesium
        alloy AZ91: The influence of acid and alkali pre-treatments," *Surface and
        Coatings Technology*, vol. 357, no. July 2018, pp. 728–739, 2019, doi:
        10.1016/j.surfcoat.2018.10.013.

[49]   V. Dalmoro, C. Alemán, C. A. Ferreira, J. H. Z. Dos Santos, D. S. Azambuja,
        and E. Armelin, "The influence of organophosphonic acid and conducting
        polymer on the adhesion and protection of epoxy coating on aluminium
        alloy," *Progress in Organic Coatings*, vol. 88, pp. 181–190, 2015, doi:
        10.1016/j.porgcoat.2015.07.004.

[50]   C. Caravaca *et al.*, "Direct silanization of zirconia for increased
        biointegration," *Acta Biomaterialia*, vol. 46, no. 2016, pp. 323–335, 2016,
        doi: 10.1016/j.actbio.2016.09.034.

[51]   M. Cadenaro *et al.*, "The role of polymerization in adhesive dentistry,"
        Dental Materials, vol. 35, no. 1, pp. 1–22, 2019, doi:
        10.1016/j.dental.2018.11.012.

[52]   J. P. Matinlinna, C. Y. K. Lung, and J. K. H. Tsoi, "Silane adhesion
        mechanism in dental applications and surface treatments: A review,"
        Dental Materials, vol. 34, no. 1, pp. 13–28, 2018, doi:
        10.1016/j.dental.2017.09.002.

[53]   X. Yue, X. Hou, J. Gao, P. Bao, and J. Shen, "Effects of MDP-based primers on shear bond strength between resin cement and zirconia," *Experimental and Therapeutic Medicine*, vol. 17, no. 5, pp. 3564–3572, Mar. 2019, doi: 10.3892/etm.2019.7382.

[54]   T. Yamauchi, H. Kitamura, N. Wakai, S. Zaima, Y. Koide, and Y. Yasuda, " Photoelectron spectroscopic studies on interfacial reactions in Zr/2×1(100)Si and Zr/SiO 2 /(100)Si systems ," *Journal of Vacuum Science & Technology A: Vacuum, Surfaces, and Films*, vol. 11, no. 5, pp. 2619–2622, 1993, doi: 10.1116/1.578616.

[55]   I. Milošev, Ž. Jovanović, J. B. Bajat, R. Jančić-Heinemann, and V. B. Mišković-Stanković, "Surface Analysis and Electrochemical Behavior of Aluminum Pretreated by Vinyltriethoxysilane Films in Mild NaCl Solution," *Journal of The Electrochemical Society*, vol. 159, no. 7, pp. C303–C311, 2012, doi: 10.1149/2.042207jes.

[56]   J. M. Oliveira, T. Miyazaki, M. A. Lopes, C. Ohtsuki, and J. D. Santos, "Bonelike®/PLGA hybrid materials for bone regeneration: Preparation route and physicochemical characterisation," *Journal of Materials Science: Materials in Medicine*, vol. 16, no. 3, pp. 253–259, 2005, doi: 10.1007/s10856-005-6687-y.

[57]   M. E. Simonsen, C. Sønderby, Z. Li, and E. G. Søgaard, "XPS and FT-IR investigation of silicate polymers," *Journal of Materials Science*, vol. 44, no. 8, pp. 2079–2088, 2009, doi: 10.1007/s10853-009-3270-9.

[58]   M. R. Turner, E. Duguet, and C. Labrugère, "Characterization of silane-modified ZrO2 powder surfaces," *Surface and Interface Analysis*, vol. 25, no. 12, pp. 917–923, 1997, doi: 10.1002/(SICI)1096-9918(199711)25:12<917::AID-SIA314>3.0.CO;2-3.

[59]   B. Sivaranjini, R. Mangaiyarkarasi, V. Ganesh, and S. Umadevi, "Vertical Alignment of Liquid Crystals over a Functionalized Flexible Substrate," *Scientific Reports*, vol. 8, no. 1, pp. 1–13, 2018, doi: 10.1038/s41598-018-27039-3.

[60]   R. Srivastava, J. Liu, C. He, and Y. Sun, "BisGMA analogues as monomers and diluents for dental restorative composite materials," *Materials Science and Engineering C*, vol. 88, no. January, pp. 25–31, 2018, doi: 10.1016/j.msec.2018.01.011.

[61]   J. Xu, I. S. Butler, D. F. R. Gibson, and I. Stangel, "High-pressure infrared and FT-Raman investigation of a dental composite," *Biomaterials*, vol. 18, no. 24, pp. 1653–1657, 1997, doi: 10.1016/S0142-9612(97)00123-3.

[62]   L. E. S. Soares, R. Rocha, A. A. Martin, A. L. B. Pinheiro, and M. Zampieri, "Monomer conversion of composite dental resins photoactivated by a halogen lamp and a LED: A FT-RAman spectroscopy study," *Quimica Nova*, vol. 28, no. 2, pp. 229–232, 2005, doi: 10.1590/S0100-40422005000200012.

[63]   P. Saen, M. Atai, A. Nodehi, and L. Solhi, "Physical characterization of unfilled and nanofilled dental resins: Static versus dynamic mechanical properties," *Dental Materials*, vol. 32, no. 8, pp. 185–197, 2016, doi: 10.1016/j.dental.2016.06.001.

[64]   Q. Wang, C. Li, M. Guo, C. Hu, and Y. Xie, "Controllable synthesis of zirconia nano-powders using vapor-phase hydrolysis and theoretical analysis," *Journal of Materials Chemistry A*, vol. 2, no. 5, pp. 1346–1352, 2014, doi: 10.1039/c3ta13571c.

[65]   A. Ghosh, A. K. Suri, M. Pandey, S. Thomas, T. R. Rama Mohan, and B. T. Rao, "Nanocrystalline zirconia-yttria system-a Raman study," *Materials Letters*, vol. 60, no. 9–10, pp. 1170–1173, 2006, doi: 10.1016/j.matlet.2005.10.102.

[66]   F. Alifui-Segbaya, J. Bowman, A. R. White, R. George, I. Fidan, and R. M. Love, "Chemical characterization of additively manufactured methacrylates for dental devices," *Additive Manufacturing*, vol. 31, no. November 2018, p. 100944, 2020, doi: 10.1016/j.addma.2019.100944.

[67]   M. M. Karabela and I. D. Sideridou, "Synthesis and study of physical properties of dental light-cured nanocomposites using different amounts of a urethane dimethacrylate trialkoxysilane coupling agent," *Dental Materials*, vol. 27, no. 11, pp. 1144–1152, 2011, doi: 10.1016/j.dental.2011.08.008.

[68]   T. Yu, Z. Zhang, Q. Liu, R. Kuliiev, N. Orlovskaya, and D. Wu, "Extrusion-based additive manufacturing of yttria-partially-stabilized zirconia ceramics," *Ceramics International*, vol. 46, no. 4, pp. 5020–5027, 2020, doi: 10.1016/j.ceramint.2019.10.245.

[69]   C. H. Lin, Y. M. Lin, Y. L. Lai, and S. Y. Lee, "Mechanical properties, accuracy, and cytotoxicity of UV-polymerized 3D printing resins composed of Bis-EMA, UDMA, and TEGDMA," *Journal of Prosthetic*

Dentistry, vol. 123, no. 2, pp. 349–354, 2020, doi: 10.1016/j.prosdent.2019.05.002.

[70]   C. G. Figueiredo-Pina, M. Guedes, J. Sequeira, D. Pinto, N. Bernardo, and C. Carneiro, "On the influence of Streptococcus salivarius on the wear response of dental implants: An in vitro study," *Journal of Biomedical Materials Research - Part B Applied Biomaterials*, vol. 107, no. 5, pp. 1393–1399, 2019, doi: 10.1002/jbm.b.34231.

[71]   C. J. Chen, S. J. Ding, and C. C. Chen, "Effects of surface conditions of titanium dental implants on bacterial adhesion," *Photomedicine and Laser Surgery*, vol. 34, no. 9, pp. 379–388, Sep. 2016, doi: 10.1089/pho.2016.4103.

[72]   O. S. Abd El-Ghany and A. H. Sherief, "Zirconia based ceramics, some clinical and biological aspects: Review," *Future Dental Journal*, vol. 2, no. 2, pp. 55–64, 2016, doi: 10.1016/j.fdj.2016.10.002.

[73]   D. Mostafa and M. Aboushelib, "Bioactive–hybrid–zirconia implant surface for enhancing osseointegration: an in vivo study," *International Journal of Implant Dentistry*, vol. 4, no. 1, 2018, doi: 10.1186/s40729-018-0129-3.

04

Polymer infiltrated ceramic networks with biocompatible adhesive and 3D-printed highly porous scaffold:

Part 2
Structure, morphology, deformation evaluation, and cell viability
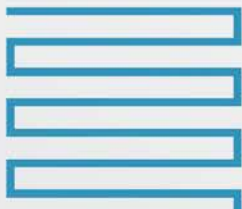
Abstract

This chapter focuses on further characterization of polymer-infiltrated ceramic networks as a material for dental application. Materials designed for such applications need to resist fracture while they undergo extreme forces, not forgetting the hostile environment of the oral cavity. In the following chapter 3D-printed porous zirconia scaffolds with 50% infill were infiltrated with Bis-GMA/TEGDMA copolymer. The proper scaffold deposition and morphology of samples with 50% zirconia infill were studied by means of X-ray computed microtomography and scanning electron microscopy. Mechanical properties of prepared PICNs were observed under compression test and compared to unfilled scaffolds as well as to 100% infill samples with the help of an Infrared Vic 2D™ camera. The microtomography proved the homogeneous distribution of pores throughout the whole sample, whereas the presence of the biocompatible copolymer among the ceramic filaments, resulting in a safety "damper", preventing crack propagation and securing the desired material flexibility, as observed by the infrared camera in real-time. Moreover, the biocompatibility of the composite material was ascertained with MG-63 cell viability assay. The results of this study represent a challenge for future dental implant applications, demonstrating that it is possible to combine the fast robocasting of ceramic paste and covalent bonding of polymer adhesive for hybrid material stabilization.

4.1   Introduction

Nowadays, the most important metal used in dental implants and jaw fixation is titanium [1]. Per-Ingvar Brånemark, a Sweden physician and research professor, successfully integrated a titanium screw into a human subject in 1965, changing the dental landscape [2]. Since then, several materials have been investigated and not only pure metals were explored but also metals, ceramics modified with biocompatible coatings, and polymers. Some examples include calcium phosphate and hydroxyapatite (HA) [3]–[6]; some metal alloys, such as nickel-titanium (NiTi), stainless steel, and Vitallium (a cobalt-chrome alloy composed of 65% Co, 30% Cr, and 5% Mo) [7]; ceramic cements like alumina (Al_2O_3), spinel ($MgAl_2O_4$) and zirconia (ZrO_2) [4]; and polymers such as sulfonated poly(ether-ether-ketone) (PEEK), poly(methylmethacrylate) (PMMA), and polylactic acid (PLA) [8]–[11].

Zirconia (ZrO_2) was first reported as being used in dental implantation surgery in 1975 when Cranin and co-workers employed zirconia and alumina (Al_2O_3) to coat Vitallium alloy [7]. Many decades later, several studies revealed some important advantages of zirconia concerning materials, for example, minimal local or systemic adverse reactions, biocompatibility with bone and soft tissues, excellent tissue response, and superior esthetic appearance, among others [12]–[15]. Zirconia has excellent mechanical and esthetic properties for orthodontic restorations, such as tooth-like natural coloration and it is suitable for the fabrication of single crowns, fixed partial dentures, and implant abutments in the dentistry field. However, the two most important drawbacks involved with this type of ceramic, from a clinical point of view, are chipping fractures and spontaneous failure caused by accelerated aging (known as low-temperature degradation) [16]–[20], as previously stated in the Introduction chapter.

From ancestral civilizations to the present day [1], there has been a continuous search for the best biomaterial for dental implants and orthodontic tools for oral

cavity and jaw fixation. For example, Schünemann et al. [15] have recently discussed the relevance of the correct ceramic surface modification to enhance osseointegration properties. Satisfactory bone-to-implant contact (BIC) values and a substantial reduction in bacterial biofilm adhesion were found in machined zirconia implants when compared to titanium ones. Moreover, it was reported that zirconia-based implants with bioactive coatings, such as calcium phosphate ceramics and bioactive glasses, can speed up the osseointegration process for both zirconia and titanium implants.

Currently, zirconia restorations are manufactured by either soft- or hard-milling processes. However, nowadays, additive manufacturing is at the top of the most important fabrication methods for the fast production and reproducibility of pieces [21]–[23]. 3D-printing technology permits facile assembly and, depending on the scaffold configuration, it can also be used to control the mechanical stability of the pieces by combining different materials (ceramic–polymer, ceramic–metal, metal–polymer) and different geometries [24]–[26].

While advancements in 3D-printing technology have increased the effectiveness of dental prototype fabrication, the desired final property of the material itself is still the key aspect setting the limitations of the fabrication process. Fortunately, we were able to create—following a robocasting route—a new polymer-infiltrated ceramic network (PICN) with 50% infill of solid yttria-stabilized tetragonal zirconia (3Y-TZP) filaments and 50% of macropores filled with methacrylate polymer, in a cubic geometry, a detailed description can be found in Chapter 3 [27]. The work demonstrated that different architectures can be explored, combining the robocasting process and the direct interfacing of biocompatible polymer adhesives inside ceramic dental implants. This approach should allow the reduction in Young's modulus of zirconia (~200 GPa) to values closer to dentin (20–25 GPa) [28]–[30], without the loss of adaptive modulation to teeth [31]. Therefore, the present work aims to investigate the morphology, crystalline structure changes, and hardness of

PICN after 3D-printing fabrication more in-depth, as well as the biocompatibility of the system when in contact with human cells.

4.2 Materials and Methods

4.2.1 Materials

Zirconia powder was provided by SEPR Saint-Gobain ZirPro under the commercial name CY3Z-R, (Le Pontet Cedex, France). It consists of 3 mol% yttria-stabilized tetragonal zirconia polycrystal (hereafter denoted as 3Y-TZP), with a particle size of about 300 nm. The ceramic density is 6.05 g·cm^{-3}, after the sintering process. Pluronic® F-127 hydrogel (25% w/v); γ-MPS (3-(trimethoxysilyl)propyl methacrylate); Bis-GMA (bisphenol A glycerolate dimethacrylate); TEGDMA (triethylene glycol dimethacrylate) and BPO (benzoyl peroxide, Luperox®A75) were all supplied by Sigma-Aldrich (Madrid, Spain) and were used to prepare the polymer-modified pieces.

4.2.2 Preparation of 3D-Printed Cubic Samples, Ceramic Functionalization, and Copolymer Covalent Deposition

The detailed procedure for scaffold fabrication, printer model, polymer infiltration, drying processes, and weight ratios of each system was reported in Chapter 3.2 and will not be repeated here. The hybrid material thus produced received the name PICN, as previously indicated. The whole process was illustrated in Figure 3-1 (Chapter 3).

4.2.3 Scaffold Characterization

In Chapter 3, section 3.3.4. we already described the equipment and methods used for the characterization of chemical structures of both, the ceramic component and the copolymer adhesive. In this section, the most relevant methods are related to the crystallinity and morphology of the 3Y-TZP structure, the PICN micro-morphology, and compression tests to evaluate the mechanism of failure.

The crystalline structure of 3Y-TZP was investigated by means of X-ray diffraction (XRD). The equipment used was a Bruker D8-Discover diffractometer (Billerica, MA, USA) with a vertical goniometer (Bragg-Brentano configuration θ-2θ), XYZ-motorized stage mounted on a sample holder, and provided with a PSD Lynx-Eye detector. The data were collected in the 2θ range from 10° to 80° with an angular step of 0.02° at 1 s per step and a fixed incidence angle of 1°. Cu Kα radiation was obtained from a Cu X-ray tube operated at 40 kV and 40 mA. The average crystal size was estimated using the Debye-Scherrer equation:

$$t = K\lambda/B \cos \theta B \qquad (1)$$

where t is the size of the crystalline domains, K is a dimensionless shape factor (default value = 0.9 when using a Cu Kα source), λ is the X-ray wavelength (0.15417 nm), B is the line broadening at half of the maximum intensity, and θB is the Bragg angle for tetragonal and monoclinic diffraction peaks.

The topography of zirconia filaments and grain size were investigated using scanning electron microscopy (SEM). The study was carried out using a focused-ion-beam Zeiss Neon 40 scanning electron microscope (Carl Zeiss, Oberkochen, Germany) and equipped with an energy-dispersive X-ray (EDX) spectroscopy system. Secondary electrons detector (SE) was employed to study the topography of the surfaces and an immersion lens detector (InLens) was preferred for high lateral resolution. The scanning was carried out at 5 kV. The samples were mounted on a double-sided adhesive carbon disc and sputter-coated with a thin layer of carbon to prevent sample charging problems.

The structure, pore distribution, and overall architecture of zirconia 3D-printed scaffolds (50% infill) were analyzed with an X-ray computed microtomography (micro-CT) Skyscan 1272 by Bruker (Kontich, Belgium). The measurement was performed at a source voltage of 100 keV and a current of 100 µA, with an isotropic

pixel size of 4.6 µm. The analysis and the scan stacking were performed with Nrecon and CTAn software from Bruker.

The Vickers hardness of the empty 3Y-TZP scaffold and the copolymer-infiltrated composite were obtained using a DuraScan 10 G5 unit by Emco-Test (Kuchl, Austria). Abraded 3D-printed samples were used, with and without infiltrated copolymer. The hardness imprint was made on the filament area of each sample using an applied load of 7 kN; thus, the data measured are reported as HV10.

The failure mode of the 50% infill 3D scaffold, 100% infill 3D scaffold, and polymer infiltrated 3D scaffold under pressure was observed with an Infrared Vic 2D™ camera and analyzed with Vic 2D software from Correlated Solutions, Inc. (Irmo, SC, USA). Vic-2D software uses optimized algorithms to provide full-field displacement and strain data for mechanical testing on planar samples. Definite in-plane movement can be determined for every point within the measurement surface, as well as by using the Lagrangian strain tensor. For this analysis, the samples were abraded to attain straight sides that were exposed to the camera recording. Compression tests were conducted using an Instron 8511 universal testing machine, under a displacement rate of 0.1 mm/s. As a result, the high-stress areas and crack propagation were recorded in real-time until the sample cracked or until a maximum applied force of 7 kN was reached.

The chemical composition of the adhesive was investigated by infrared spectroscopy. The infrared spectra of Bis-GMA/TEGDMA copolymer and pure monomers were measured with an FTIR 4700 Jasco spectrophotometer (Madrid, Spain). The equipment is coupled to an attenuated total reflection (ATR) accessory (Specac model MKII Golden Gate Heated Single Reflection Diamond ATR). For this, 32 scan accumulations and a resolution of 8 cm^{-1} were chosen for spectra acquisition in the wavenumber range from 4000 cm^{-1} to 600 cm^{-1}. The spectra are reported as a percentage of transmittance versus wavenumber.

4.2.4   Human Cells Adhesion and Proliferation

MG-63 cells (derived from human osteosarcoma; ATCC) were cultured in Dulbecco's modified Eagle's medium (DMEM). It contains 4500 mg/L of glucose, 110 mg/L of sodium pyruvate, and 2 mM of L-glutamine, complemented with 10% fetal bovine serum (FBS); 50 U/cm^3 penicillin, 50 mg/mL streptomycin, and L-glutamine 2 mM at 37 °C, in a 10% humidified atmosphere with CO_2 and air in the proportion of 5% and 95%, respectively. Culture media were changed every two days, as standard protocol. For the sub-culture, cell monolayers were rinsed with PBS solution (phosphate buffer saline) and detached by incubating them with 2 mL TrypLETM (Gibco, Amarillo, TX, USA) for 2–5 min at 37 °C. The incubation was stopped by re-suspending in 5 mL of fresh medium. For cell counting, a Neubauer camera and a dye (trypan blue, 4%) were employed.

3D scaffolds were placed in 12-well tissue culture plates and sterilized by exposure to UV light for 15 min for each side of the cube. A culture medium (4 mL) was added to each well to cover the scaffolds. Then, 100 μL containing 2×10^4 cells/well to rate cell adhesion, and 5×10^4 cells/well for a cell proliferation assay, were seeded in each well. The plates were incubated for 24 h to check the cellular adhesion and, further, for 7 days to determine the cell proliferation. In parallel, the control was performed in each without any scaffold.

The percentage of cells adhered (after 24 h) and proliferated (after 7 days) was determined through an MTT (3-(4,5-dimethylthiazol-2-yl)-2,5-diphenyltetrazolium bromide) assay [32]. The procedure consisted of washing each well per triplicate with PBS and adding 4 mL of culture medium to each well. Afterward, 200 μL of MTT (3 mg/mL) were also added and incubated for 4 h. Then, the samples were washed again (twice) with PBS and the specimens were deposited in a new plate. Finally, 2 mL of dimethyl sulfoxide (DMSO) were subsequently added to each well to measure the absorbance (570 nm) in a microplate reader (Biochrom EZ-Read 400, Fisher

Scientific, Madrid, Spain), after 15 min of gentle stirring. Three replicates were evaluated, and the corresponding values were averaged for its plot representation; statistical analysis was performed by ANOVA software, followed by the Tukey test (OriginPro v8).

4.3 Results and Discussion

4.3.1 Hybrid Material Characterization

The fabrication of dense and geometrically complex ceramic structures through 3D-printing technology by using polymer-derived ceramic precursors is relatively easy with 100% infill of ceramic deposition. However, the preparation of 3D-printed highly porous structures is rather difficult, due to the sample deformation. Considering that the objective of this study was the development of a hybrid material intended for dental applications, the most important properties to be evaluated for the new PICN material are the mechanical resistance and osseointegration via a cell viability test. The first property will be affected by the piece's geometry, the proper infiltration of polymer adhesive to create the PICN structure, and the crystal structure of the zirconia filaments after the robocasting and sintering processes. In this regard, the geometry was fixed to have the maximum percentage of macropores as possible without the loss of the CAD/CAM 3D cubic design, characterized by a layer-by-layer zigzag filament deposition and the number of layers being 10 (Figure 4-1, inset image). Proper polymer infiltration has been discussed in depth in the previous Chapter 3.3.1-3.3.2.

It is well known that the monoclinic and cubic phases of zirconia are less mechanically stable than the tetragonal ones, and that phase changes are usually observed after aging, hydration, or temperature increase [33]–[35]. The XRD spectrum of the 3D-printed material shows typical changes that have been reported in the literature [25]. After the robocasting and sintering processes, both tetragonal and monoclinic phases coexist. However, in this study, the comparison of spectra

from the powder and the 3D-printed piece (Figure 4-1) indicates that the tetragonal phase is predominant, whereas the monoclinic one decreases substantially [34]. Moreover, a lack of broadening of the (111) peak confirms that there is no overlapping with other phases (e.g., the rhombohedral one). Similarly, the (002) and (200) peaks at 34.8° and 35.3°, associated with the tetragonal phase, have converged into pure tetragonal phases when compared to the spectrum of the powder. This further indicates that this phase is concentrated in regions of less than 1 μm from the surface; it should be noted that, for an incidence angle of 1° with Cu Ka radiation, the penetration depth is ~0.3 μm. The XRD peaks of the sintered 3D-printed body were indexed against the standard reflection pattern of tetragonal (t-ZrO_2; JCPDS #50-1089) and monoclinic (m-ZrO_2; JCPDS #37-1484) zirconia.
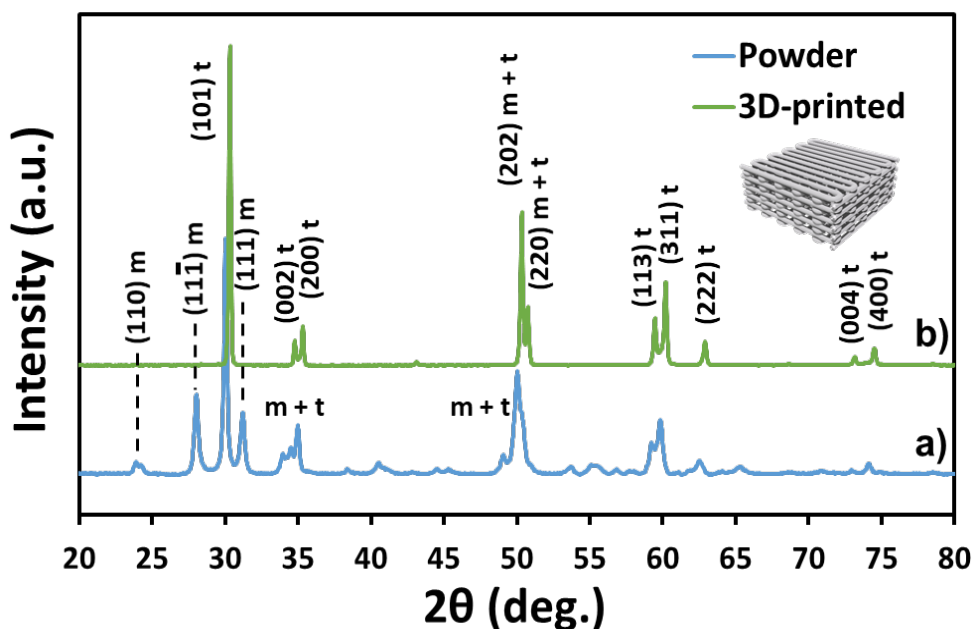
Figure 4-1: XRD spectra with an incident angle of 1° of: (a) 3Y-TZP powder and (b) 3D-printed sample, after the robocasting and sintering process, up to 700 °C and 1450 °C. The inset represents the cubic geometry designed by layer-by-layer zigzag filament deposition to create macropores for further copolymer infiltration.

The crystalline size of the tetragonal lattice was found to be 35 nm and 51 nm, before and after robocasting, respectively (Table 4-1). From these data, it is clear that the tetragonal structure is formed after the rearrangement of monoclinic nanocrystallites. The size of these nanocrystals tends to be slightly higher in the case of the 3D-printed samples than in the case of the powder ones.

Table 4-1: Application of the Debey–Scherrer (equation 1) for 3Y-TZP powder and 3D-printed zirconia cubes.

Sample	Phase	2θ	$\cos(\theta)$	B (rad)	t (nm)
3Y-TZP powder	Monoclinic	28	0.970	0.005	28
	Tetragonal	30	0.966	0.004	35
3D-printed	Monoclinic	-	-	-	-
	Tetragonal	30	0.966	0.003	51

The computed tomography technique (commonly referred to as micro-CT) allowed 3D- and 2D-investigations of the marginal and internal gaps produced by the computer-aided manufacturing of zirconia scaffolds, within the range of a few micrometers (Figure 4-2). The ceramic scaffold obtained was found to be very stable, even though 50% of the volume of the cubic pieces—generated through robocasting of ten zig-zag layers of zirconia filaments (Figure 4-2a)—is composed of voids. In Figure 4-2b, it is possible to envisage the direction of the filament deposition. The images also reveal the shrinkage of the whole structure after the sintering step, corresponding to a contraction of about 20%. According to the micro-CT image in Figure 4-2c, the average size of macropores is 380.11 ± 51.77 µm.
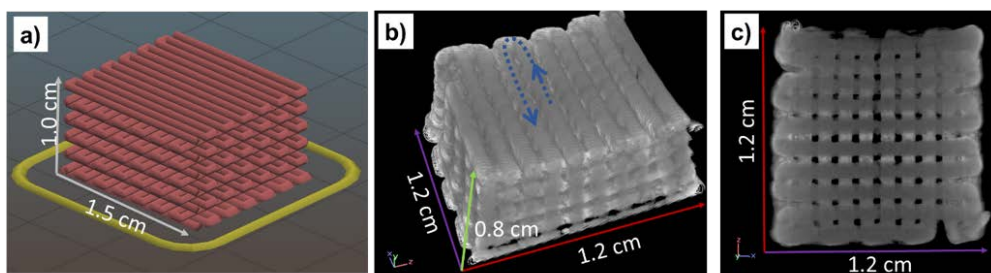
Figure 4-2: a) CAD/CAM 3D design of the simple cubic geometry of zirconia. Reprinted from Ref. [27] with permission; Copyright Elsevier 2021, (b) three-dimensional micro-CT image and (c) cross-sectional micro-CT image of the sintered 3D-printed scaffold, with a 50% feed infill of zirconia. The dashed arrow in (b) indicates the direction of filament deposition in one single layer.

The successful deposition of zirconia filaments was only possible thanks to the mixing of 3Y-TZP powder with Pluronic® hydrogel under vacuum, which helped to avoid bubbles, and, thanks to the employment of an adequate printer nozzle (800 µm in diameter), which avoided particle agglomerations and the formation of defects during the printing process. In Figure 4-3, the morphology of the 3Y-TZP zirconia powder has been compared with that obtained after the robocasting process. As can be seen, the zirconia powder has a spherical morphology with particle diameters at a micrometric scale (109 ± 25 µm, Figure 4-3a). After the robocasting deposition and sintering, the particles have been reduced to 448 ± 71 nm (Figure 4-3b). In the same micrograph, inter-particle voids left by the hydrogel degradation can be also visualized. The porosity of such dense filaments was determined and reported (Chapter 3.3.1) by gas displacement pycnometry, being very low (3%). Thus, such microporosity is not presumed to affect the copolymer infiltration of macropores, strategically created to reinforce the 3Y-TZP zirconia scaffolds. Once the material was printed and sintered at high temperatures, the SEM images at low magnification revealed the good stability of the zirconia filaments (Figure 4-3c), corroborating that observed previously by micro-CT (Figure 4-3b). The surface topography was inspected by employing the InLens detector (Figure 4-3d) and secondary electrons detector (Figure 4-3e). As can be seen, the filaments exhibit a granular texture and are perfectly deposited layer-by-layer.
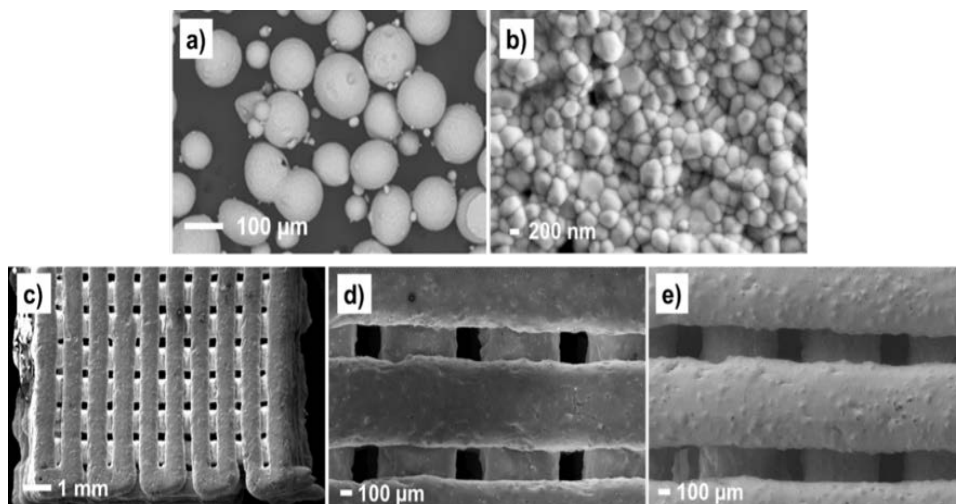
Figure 4-3: SEM micrographs of (a) 3Y-TZP powder; (b) zirconia paste after robocasting and sintering; (c) 3D-printed zirconia filaments and macropores created by the robocasting architecture; (d,e) high magnification micrographs with a detail of 3 well-arranged filaments. All images were taken with an InLens detector, with the exception of Figure (e) where the secondary electrons detector (SE) was employed to better visualize the surface texture of the filaments.

The PICN pieces, with the zirconia scaffold voids filled by the copolymer adhesive, were polished and the infiltrated polymer was analyzed by ATR-FTIR spectroscopy, comparing the main chemical bonds of cured copolymer with the pristine monomers (Figure 4-4); the O–H stretching appearing at ~3400 cm^{-1} belongs to the Bis-GMA units. This compound also produces O–H bending vibrations but the latter couple with other vibrations and produce complex bands in the fingerprint region, coinciding with that of ester and ether groups (1000–1200 cm^{-1}). The spectra of monomers also show a sharp absorption band, corresponding to the C=C stretching wavenumber at 1635 cm^{-1}, which has been reduced in the copolymer spectrum, evidencing successful radical copolymerization. The presence of aromatic rings from the Bis-GMA monomer also manifests in the region between 900 and 800 cm^{-1}. Moreover, the extensive presence of methylene groups can be confirmed by the absorption band at 1452 cm^{-1}, corresponding to scissoring frequencies [36,37]. The intensity of functional groups associated with the Bis-GMA and TEGDMA units depends on the copolymer ratio.
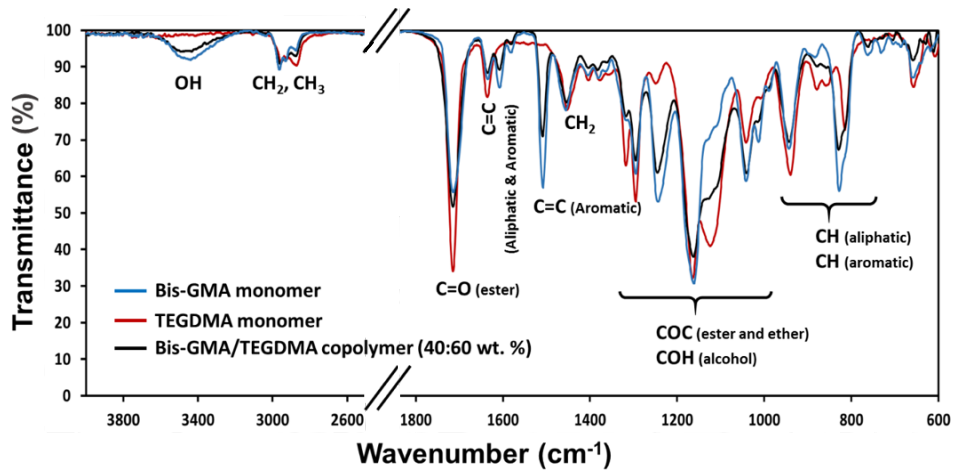
Figure 4-4: FTIR spectra of Bis-GMA/TEGDMA copolymer in the PICN sample, after curing at 110 °C, and the respective monomers used for the copolymer synthesis.

4.3.2   Mechanical Tests

In previous Chapter 3.3.3 it was demonstrated that 3D-printed zirconia with 50% zirconia infill and PICN (3D-printed zirconia 50% infill, reinforced with Bis-GMA/TEGDMA copolymer) exhibit different mechanical resistance to compression forces. In this work, the reasons for such distinct behavior have been elucidated by recording the deformation of filaments in real-time during compression tests, using an infrared camera.

As explained in previous Chapters, the PICN material is intended to be used in the dentistry field, combining biocompatible ceramic and polymer adhesive. The dental implants are subjected to direct compression and abrasion forces with teeth. Therefore, it is important to evaluate its hardness and mechanical response under compression forces. Vickers hardness tests were conducted on the 50% infill scaffold and the polymer-infiltrated one. The Vicker's hardness of the hollow scaffolds (50% infill) was 1414 ± 176 HV10 whereas, for the PICN scaffolds, it was lower (1078 ± 49 HV10). The lower hardness of the PICN sample can be explained by its higher flexibility and resistance to breaking under pressure, due to the filling of the zirconia macropores with Bis GMA/TEGDMA copolymer, which is a softer material. In

summary, the filled macropores transform a rigid and brittle ceramic into a more compliant and softer material. Lin et. al. [38] have reported Vicker's hardness values of 14.5–24.6 HV 0.1, for different compositions of Bis-GMA, TEGDMA, and urethane dimethacrylate 3D printed 100% infill samples.

Other authors have reported different grades of "dense" polymer-infiltrated ceramics varying from 59 to 72% [39]. The hardness (HV5) decreased by a factor of 3.1 GPa to 6.1 GPa for 72% infill and 59% infill, respectively, compared to the 100% dense ceramic (6.41 GPa). Obviously, the absolute values cannot be compared to those obtained in the present work, due to different architectures and polymer-ceramic compositions. However, the tendency is the reduction of hardness in all cases. Thus, it is expected that the copolymer filling can absorb part of the load applied to the rigid zirconia filaments, reducing the intrinsic hardness of the ceramic. The hypothesis of the copolymer acting as a "safety cushion", preventing crack propagation and securing the desired material flexibility, was supported by the response recorded using an infrared camera (Figure 4-5). Here, three types of 3D-printed samples were evaluated: 50% zirconia infill (Figure 4-5a–c, video 50%); 100% zirconia infill (Figure 4-5d–f, video 100%); and PICN (Figure 4-5g–i, video PICN). The videos can be accessed and downloaded at the following link: https://www.mdpi.com/1996-1944/14/19/5513 as supplementary information to our work, from which this chapter has been adapted [40].
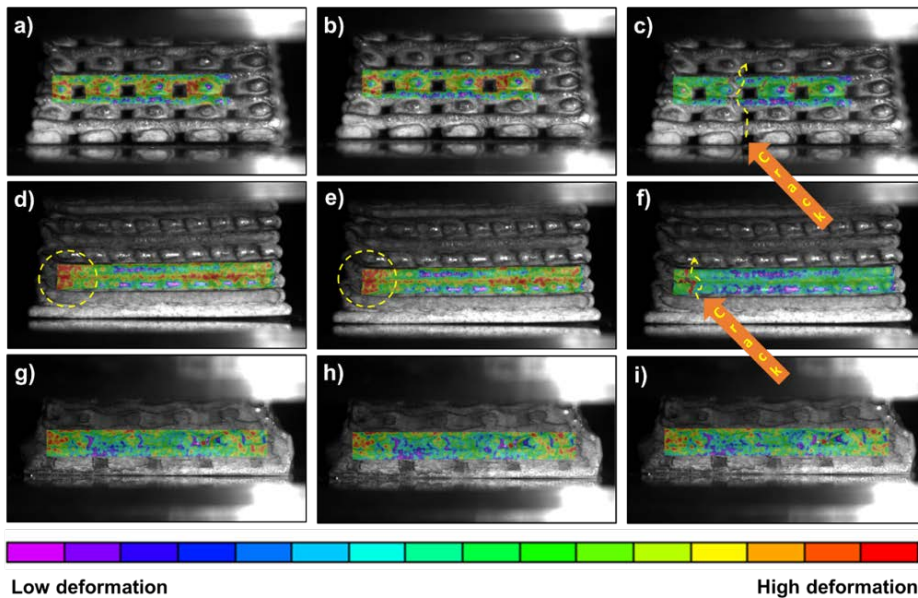
Figure 4-5: Digital images progress of deformation in the 3D-printed scaffolds, under a compression experiment: (a–c) 50% infill of 3D-printed zirconia, (d–f) 100% infill, (g–i) PICN sample (50% infill of 3D-printed zirconia with infiltrated copolymer). Dashed yellow arrows indicate the direction of filaments breaking, orange arrows indicate the crack propagation and yellow dashed circles show the zone with high deformation under compression, characterized by a deep red color.

The breaking of the first filament and crack propagation starts at 0.55 kN in the case of zirconia scaffolds with macropores (video 50%). Failure initiates in a filament at the bottom of the cubic piece and extends to the top face very quickly (Figure 4-5c). As expected, the 100% infill 3D-printed sample was found to be more resistant than the 50% infill one. In this case, the deformation is distributed along filaments placed in the middle of the sample, being one of the edges, indicated by the red color and highlighted by circles in Figure 4-5d,e, the zone subjected to higher stresses. The cracking and, soon afterward, the complete breaking of the samples with 50% and 100% infill is indicated with an orange arrow in Figure 4-5c,f. For the latter percentage, complete breaking occurs under 1.4 kN of compression force.

As can be seen in Figure 4-5g–i, for the same test with the PICN sample, the copolymer holds up the filaments and reduces the amount of stress applied to the sample. With the images and the video recorded (video PICN) for the piece cross-

section, it is possible to visualize that the blue zones (low deformation) are located in the interface of the zirconia filaments and polymer adhesive. Such observations of the compression-induced cracks indicate that the polymer network causes lower crack deflection than the 100% infill ceramic material (video 100%). Moreover, the 3D-printed sample with infiltrated polymer achieves values of maximum strength that are twice those observed for pieces without polymer (Table 4-2), without breaking (i.e., it resists compression forces higher than 1 kN). Table 4-2 summarizes the stress-strain mechanical properties until complete breakdown. Altogether, these findings led to the conclusion that a PICN hybrid material can be a good candidate to replace pure zirconia implants in the near future.

Table 4-2: Stress-strain data from the compression tests.

Sample	σ_{max}[1] (MPa)	σ_{break} (MPa)	$\varepsilon_{compression}$[2] (%)
3D-printed zirconia 50% infill	86	51	4.1
3D-printed zirconia 100% infill	124	124	5.2
PICN	102	102	5.2

Notes: [1] σ = strength, ε = percentage of compression resistance until breaking or with a maximum of compression force. [2] Maximum compression percentage until the sample's breaking.

4.3.3   In Vitro Human Cell Adhesion and Proliferation

In a previous Chapter 3.3.4, it was shown that *Escherichia coli* and *Streptococcus salivarius* bacteria are not able to proliferate on the 3D-printed PICN scaffolds with Bis-GMA/TEGDMA acrylate adhesive in 7 days. This is an important issue since bacterial infections can cause the rejection of dental implants due to their spread to the jawbone and other structures of the oral cavity, causing a risk of peri-implantitis. In this study, the cell viability of the new system to support the bone and surrounding tissue integration of the new ceramic–organic material was explored. Figure 4-6 shows the percentages of viability for adhesion and proliferation of the

bone-derived epithelial cells (MG-63 cells) that were seeded on the 3D scaffolds. Low adhesion percentages of 41 ± 5% and 35 ± 7%, respectively, are shown in zirconia scaffolds (3Y-TZP) and in zirconia scaffolds with a silane coating (γ-MPS) (Figure 4-6a). These percentages were significantly lower ($p < 0.05$) than those measured for cell adhesion of PICN samples, i.e., 68 ± 12%. Although, this percentage is high, a significant part of the cells seeded in the well-drained area toward the plate surface, suggesting that a block with a larger surface area on the upper face could improve the percentage of adhesion and retention of the cells in the 3D scaffold.
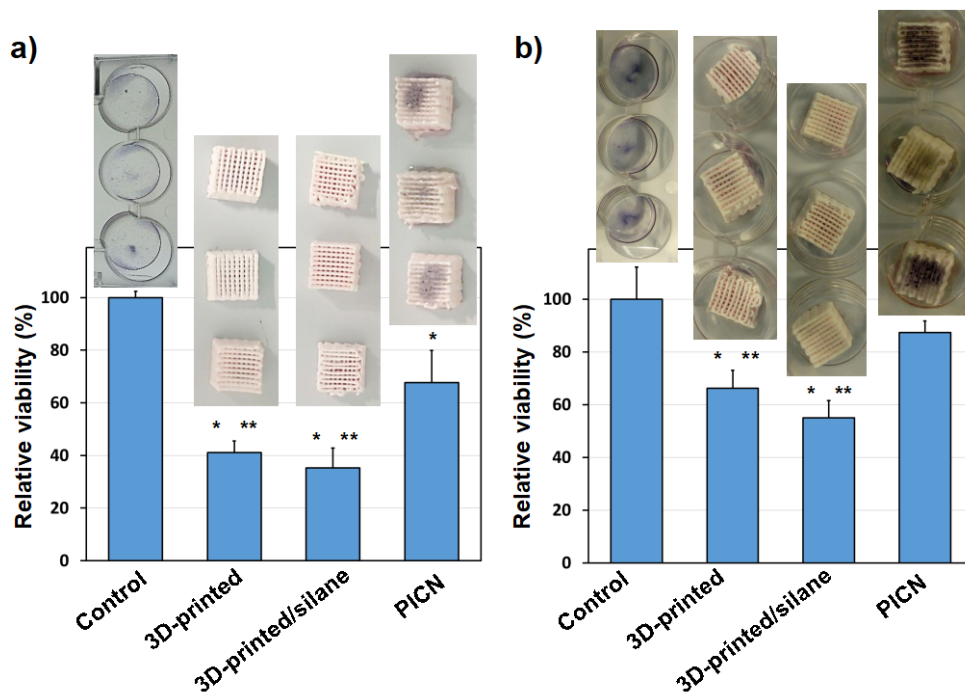
*Figure 4-6: Viability of osteogenic MG-63 cells in the 3D scaffolds. Quantification of cellular adhesion (a) and proliferation (b). Above each bar, images of the MTT reaction by viable cells, appearing as diffuse or dark spots, are shown. * p < 0.05 vs. control, ** p < 0.05 vs. copolymer (ANOVA–Tukey's test).*

The proliferation results indicate that the three types of 3D scaffolds prepared were compatible with cell growth (Figure 4-6b). The percentages of cell viability at 7 days of culture were 66 ± 7% and 55 ± 7%, for zirconia scaffolds (3Y-TZP) and

zirconia scaffolds with a silane coating (γ-MPS). However, they were significantly lower than the control (p < 0.05). In this same direction, cell proliferation is noticeable in the 3D scaffolds coated with silane and copolymer (PICN), where the percentage of viability was 87 ± 5%, which was not different from the control. Qualitative support of the above findings and statement is given in Figure 4-6, which shows digital photographs of the 3D scaffolds with viable cells visualized as dots or diffused dark coloration on the surface of the scaffolds. It is quite pronounced in the zirconia scaffold with a silane coating and Bis-GMA/TEGDMA copolymer. It can be concluded that the best results, regarding both adhesion and cell proliferation, were obtained for PICN samples.

Several works have demonstrated the viability of zirconia material towards human-osteoblast cells [14], [39], [41]. Carinci et al. [42] were able to express various genes from an osteoblast-like cell line (MG-63) cultured on zirconium oxide discs, proving that the ceramic surface is able to promote important cell functions, such as immunity, vesicular transport, and cell cycle regulation. On the contrary, silane compounds do not significantly affect cellular adhesion and viability, they are preferably used as a coupling agent for active biomolecules, like the polysaccharides and proteins used as coatings for implants [43], [44].

As described in more detail in the following Chapter 6, a catechol-ethylene glycol dimethacrylate copolymer adhered to Y-TZP zirconia discs was tested with MG-63 cells, finding relative viability of 100% and 93% for cell adhesion (24 h) and cell proliferation (7 days), respectively. In the present study, the relative viability of MG-63 cells was 87 ± 5% (Figure 4-6b), thus validating the prompt biocompatibility of the acrylate copolymer.

Therefore, the insertion of acrylate copolymers on zirconia has demonstrable advantages for bioactivity, since they can induce the cell adhesion essential for subsequent bone proliferation. The PICN samples studied also display a good correlation regarding structural integrity and biocompatibility. Future work needs to

be performed in order to focus on its application in clinical practice. In this sense, mechanical properties, together with cell viability and reduced bacteria proliferation as explained in Chapter 3.3.4, should be proved in complex 3D-printed geometry that is used for dental implants.

4.4 Conclusions

Here, the successful obtaining of a stable and mechanically resistant PICN 3D-printed scaffold with a biocompatible copolymer acrylate inside the structure macropores was described. The superior cohesion of 3Y-TZP particles in the ceramic layer-by-layer filaments, after sintering, together with the very stable zigzag ceramic configuration, strategically designed to create the 50% infill cubic structures, led to the obtaining of promising hybrid material for dental applications.

For the first time, it was possible to demonstrate that the copolymer infiltrated among the ceramic filaments, created by CAD/CAM design, acts as a mechanical stabilizer and adhesion promoter at the same time.

The compression-testing, combined with the *in situ* observation of cracking phenomena with an infrared camera, led to the conclusion that PICN samples have a larger capability to resist higher deformation than 50% infill ceramic scaffolds. Moreover, the presence of the polymer also aids in decreasing the ceramic hardness, both properties being desirable for using zirconia material in dentistry.

The results of MG-63 cell adhesion and proliferation of PICN, compared to 3D-printed zirconia without copolymer adhesive, are also a positive point for future biomedical applications.

4.5 References

[1]   C. M. Abraham, "A Brief Historical Perspective on Dental Implants, Their Surface Coatings and Treatments," *The Open Dentistry Journal*, vol. 8, no. 1, pp. 50–55, 2014, doi: 10.2174/1874210601408010050.

[2]   L. Carlsson, T. Röstlund, B. Albrektsson, T. Albrektsson, and P.-I. Brånemark, "Osseointegration of titanium implants," *Acta Orthopaedica Scandinavica*, vol. 57, no. 4, pp. 285–289, 2009, doi: 10.3109/17453678608994393.

[3]   M. Stefanic, K. Krnel, I. Pribosic, and T. Kosmac, "Rapid biomimetic deposition of octacalcium phosphate coatings on zirconia ceramics (Y-TZP) for dental implant applications," *Applied Surface Science*, vol. 258, no. 10, pp. 4649–4656, Mar. 2012, doi: 10.1016/j.apsusc.2012.01.048.

[4]   A. Jonhson, P. Sinthuprasirt, H. Fathi, and S. Pollington, "Current Glass-Ceramic Systems Used in Dentistry," in *Current Trends on Glass and Ceramic Materials*, S. H. Nandyala and J. Dos Santos, Eds. Sharjak: Bentham Science Publishers, 2013, pp. 49–72.

[5]   M. S. Zafar, M. A. Fareed, S. Riaz, M. Latif, S. R. Habib, and Z. Khurshid, "Customized therapeutic surface coatings for dental implants," *Coatings*, vol. 10, no. 6, pp. 1–37, 2020, doi: 10.3390/coatings10060568.

[6]   L. C. Trincă *et al.*, "Osseointegration evaluation of ZrTi alloys with hydroxyapatite-zirconia-silver layer in pig's tibiae," *Applied Surface Science*, vol. 487, pp. 127–137, Sep. 2019, doi: 10.1016/j.apsusc.2019.05.003.

[7]   A. N. Cranin, P. A. Schnitman, M. Rabkin, T. Dennison, and E. J. Onesto, "Alumina and zirconia coated vitallium oral endosteal implants in beagles," *Journal of Biomedical Materials Research*, vol. 9, no. 4, pp. 257–262, 1975, doi: 10.1002/jbm.820090429.

[8]   R. S. Brum *et al.*, "Polymer coatings based on sulfonated-poly-ether-ether-ketone films for implant dentistry applications," *Journal of Materials Science: Materials in Medicine*, vol. 29:132, no. 8, p. 1 of 9, 2018, doi: 10.1007/s10856-018-6139-0.

[9]   L. C. Natale *et al.*, "Development of calcium phosphate/ethylene glycol dimethacrylate particles for dental applications," *Journal of Biomedical Materials Research - Part B Applied Biomaterials*, vol. 107, no. 3, pp. 708–715, Apr. 2019, doi: 10.1002/jbm.b.34164.

[10]   R. Gautam, R. D. Singh, V. P. Sharma, R. Siddhartha, P. Chand, and R. Kumar, "Biocompatibility of polymethylmethacrylate resins used in dentistry," *Journal of Biomedical Materials Research B: Applied Biomaterials*, vol. 9999B, pp. 1–7, 2012, doi: 10.1002/jbm.b.32673.

[11]   D. Rokaya, V. Srimaneepong, J. Sapkota, J. Qin, K. Siraleartmukul, and V. Siriwongrungson, "Polymeric materials and films in dentistry: An overview,"

Journal of Advanced Research, vol. 14, pp. 25–34, 2018, doi: 10.1016/j.jare.2018.05.001.

[12]   M. Hisbergues, S. Vendeville, and P. Vendeville, "Zirconia: Established facts and perspectives for a biomaterial in dental implantology," *Journal of Biomedical Materials Research - Part B Applied Biomaterials*, vol. 88, no. 2, pp. 519–529, 2009, doi: 10.1002/jbm.b.31147.

[13]   Z. Özkurt and E. Kazazoğlu, "Zirconia dental implants: A literature review," *Journal of Oral Implantology*, vol. 37, no. 3, pp. 367–376, 2011, doi: 10.1563/AAID-JOI-D-09-00079.

[14]   K. Sivaraman, A. Chopra, A. I. Narayan, and D. Balakrishnan, "Is zirconia a viable alternative to titanium for oral implant? A critical review," *Journal of Prosthodontic Research*, vol. 62, no. 2, pp. 121–133, 2018, doi: 10.1016/j.jpor.2017.07.003.

[15]   F. H. Schünemann *et al.*, "Zirconia surface modifications for implant dentistry," *Materials Science and Engineering C*, vol. 98, no. July 2018, pp. 1294–1305, 2019, doi: 10.1016/j.msec.2019.01.062.

[16]   B. Al-Amleh, K. Lyons, and M. Swain, "Clinical trials in zirconia: a systematic review.," *J Oral Rehabil*, vol. 37, no. 8, pp. 641–652, 2010, doi: 10.1111/j.1365-2842.2010.02094.x.

[17]   L. Kolgeci, E. Mericske, A. Worni, P. Walker, J. Katsoulis, and R. Mericske-Stern, "Technical Complications and Failures of Zirconia-Based Prostheses Supported by Implants Followed Up to 7 Years: A Case Series," *The International Journal of Prosthodontics*, vol. 27, no. 6, pp. 544–552, 2014, doi: 10.11607/ijp.3807.

[18]   R. B. Osman, M. V. Swain, M. Atieh, S. Ma, and W. Duncan, "Ceramic implants (Y-TZP): Are they a viable alternative to titanium implants for the support of overdentures? A randomized clinical trial," *Clinical Oral Implants Research*, vol. 25, no. 12, pp. 1366–1377, Dec. 2014, doi: 10.1111/clr.12272.

[19]   F. Nejatidanesh, M. Abbasi, G. Savabi, M. Bonakdarchian, R. Atash, and O. Savabi, "Five year clinical outcomes of metal ceramic and zirconia-based implant-supported dental prostheses: A retrospective study," *Journal of Dentistry*, vol. 100, no. June, 2020, doi: 10.1016/j.jdent.2020.103420.

[20]   F. Zarone, M. I. Di Mauro, G. Spagnuolo, E. Gherlone, and R. Sorrentino, "Fourteen-year evaluation of posterior zirconia-based three-unit fixed dental

prostheses: A Prospective clinical study of all ceramic prosthesis," *Journal of Dentistry*, vol. 101, no. March, 2020, doi: 10.1016/j.jdent.2020.103419.

[21]   H. N. Chia and B. M. Wu, "Recent advances in 3D printing of biomaterials," *Journal of Biological Engineering*, vol. 9, no. 1, pp. 1–14, 2015, doi: 10.1186/s13036-015-0001-4.

[22]   L. C. Hwa, S. Rajoo, A. M. Noor, N. Ahmad, and M. B. Uday, "Recent advances in 3D printing of porous ceramics: A review," *Current Opinion in Solid State and Materials Science*, vol. 21, no. 6, pp. 323–347, 2017, doi: 10.1016/j.cossms.2017.08.002.

[23]   M. Juneja, N. Thakur, D. Kumar, A. Gupta, B. Bajwa, and P. Jindal, "Accuracy in dental surgical guide fabrication using different 3-D printing techniques," *Additive Manufacturing*, vol. 22, no. May, pp. 243–255, 2018, doi: 10.1016/j.addma.2018.05.012.

[24]   D. Zhang, E. Peng, R. Borayek, and J. Ding, "Controllable Ceramic Green-Body Configuration for Complex Ceramic Architectures with Fine Features," *Advanced Functional Materials*, vol. 29, no. 12, pp. 1–12, 2019, doi: 10.1002/adfm.201807082.

[25]   A. C. Branco *et al.*, "Suitability of 3D printed pieces of nanocrystalline zirconia for dental applications," *Dental Materials*, vol. 36, no. 3, pp. 442–455, 2020, doi: 10.1016/j.dental.2020.01.006.

[26]   D. Zhang *et al.*, "A 3D-printing method of fabrication for metals, ceramics, and multi-materials using a universal self-curable technique for robocasting," *Materials Horizons*, vol. 7, no. 4, pp. 1083–1090, 2020, doi: 10.1039/c9mh01690b.

[27]   Ľ. Hodásová *et al.*, "Polymer infiltrated ceramic networks with biocompatible adhesive and 3D-printed highly porous scaffolds," *Additive Manufacturing*, vol. 39, no. November 2020, p. 101850, Mar. 2021, doi: 10.1016/j.addma.2021.101850.

[28]   S. N. White, V. G. Miklus, E. A. McLaren, L. A. Lang, and A. A. Caputo, "Flexural strength of a layered zirconia and porcelain dental all-ceramic system," *Journal of Prosthetic Dentistry*, vol. 94, no. 2, pp. 125–131, Aug. 2005, doi: 10.1016/j.prosdent.2005.05.007.

[29]   D. Ziskind, M. Hasday, S. R. Cohen, and H. D. Wagner, "Young's modulus of peritubular and intertubular human dentin by nano-indentation tests,"

Journal of Structural Biology, vol. 174, no. 1, pp. 23–30, Apr. 2011, doi: 10.1016/j.jsb.2010.09.010.

[30]   J. Li *et al.*, "Mechanical performance of polymer-infiltrated zirconia ceramics," *Journal of Dentistry*, vol. 58, pp. 60–66, 2017, doi: 10.1016/j.jdent.2017.01.008.

[31]   S. Wille, K. Sieper, and M. Kern, "Wear resistance of crowns made from different CAM/CAD materials," *Dental Materials*, pp. 1–7, 2021, doi: 10.1016/j.dental.2021.03.017.

[32]   T. Mosmann, "Rapid colorimetric assay for cellular growth and survival: Application to proliferation and cytotoxicity assays," *Journal of Immunological Methods*, vol. 65, no. 1–2, pp. 55–63, Dec. 1983, doi: 10.1016/0022-1759(83)90303-4.

[33]   S. Zinelis, A. Thomas, K. Syres, N. Silikas, and G. Eliades, "Surface characterization of zirconia dental implants," *Dental Materials*, vol. 26, no. 4, pp. 295–305, 2010, doi: 10.1016/j.dental.2009.11.079.

[34]   J. A. Muñoz-Tabares, E. Jiménez-Piqué, J. Reyes-Gasga, and M. Anglada, "Microstructural changes in ground 3Y-TZP and their effect on mechanical properties," *Acta Materialia*, vol. 59, no. 17, pp. 6670–6683, 2011, doi: 10.1016/j.actamat.2011.07.024.

[35]   T. Maridurai, D. Balaji, and S. Sagadevan, "Synthesis and characterization of yttrium stabilized zirconia nanoparticles," *Materials Research*, vol. 19, no. 4, pp. 812–816, 2016, doi: 10.1590/1980-5373-MR-2016-0196.

[36]   A. C. Karmaker, A. T. Dibenedetto, and A. J. Goldberg, "Extent of conversion and its effect on the mechanical performance of Bis-GMA/PEGDMA-based resins and their composites with continuous glass fibres," *Journal of Materials Science: Materials in Medicine*, vol. 8, no. 6, pp. 369–374, 1997, doi: 10.1023/A:1018584917296.

[37]   M. Teotia, M. Chauhan, P. Choudhary, and R. K. Soni, "Photocured characteristics of fast photocurable acrylic formulations and investigations by differential photo calorimeter," *Journal of Thermal Analysis and Calorimetry*, vol. 137, no. 1, pp. 133–141, 2019, doi: 10.1007/s10973-018-7907-2.

[38]   C. H. Lin, Y. M. Lin, Y. L. Lai, and S. Y. Lee, "Mechanical properties, accuracy, and cytotoxicity of UV-polymerized 3D printing resins composed of Bis-EMA,

UDMA, and TEGDMA," *Journal of Prosthetic Dentistry*, vol. 123, no. 2, pp. 349–354, 2020, doi: 10.1016/j.prosdent.2019.05.002.

[39]   A. Coldea, M. v. Swain, and N. Thiel, "Mechanical properties of polymer-infiltrated-ceramic-network materials," *Dental Materials*, vol. 29, no. 4, pp. 419–426, 2013, doi: 10.1016/j.dental.2013.01.002.

[40]   Ľ. Hodásová, C. Alemán, L. J. del Valle, L. Llanes, G. Fargas, and E. Armelin, "3D-printed polymer-infiltrated ceramic network with biocompatible adhesive to potentiate dental implant applications," *Materials*, vol. 14, no. 19, pp. 1–14, 2021, doi: 10.3390/ma14195513.

[41]   Y. Josset, Z. Oum'Hamed, A. Zarrinpour, M. Lorenzato, J. J. Adnet, and D. Laurent-Maquin, "In vitro reactions of human osteoblasts in culture with zirconia and alumina ceramics.," *J Biomed Mater Res*, vol. 47, no. 4, pp. 481–493, Dec. 1999, doi: 10.1002/(sici)1097-4636(19991215)47:4<481::aid-jbm4>3.0.co;2-y.

[42]   F. Carinci *et al.*, "Zirconium oxide: Analysis of MG63 osteoblast-like cell response by means of a microarray technology," *Biomaterials*, vol. 25, no. 2, pp. 215–228, 2004, doi: 10.1016/S0142-9612(03)00486-1.

[43]   C. Tonda-Turo *et al.*, "Comparative analysis of gelatin scaffolds crosslinked by genipin and silane coupling agent," *International Journal of Biological Macromolecules*, vol. 49, no. 4, pp. 700–706, 2011, doi: 10.1016/j.ijbiomac.2011.07.002.

[44]   K. Fang *et al.*, "Immobilization of chitosan film containing semaphorin 3A onto a microarc oxidized titanium implant surface via silane reaction to improve MG63 osteogenic differentiation," *International Journal of Nanomedicine*, vol. 9, no. 1, pp. 4649–4657, 2014, doi: 10.2147/IJN.S68895.

05

Polymer infiltrated ceramic networks with biocompatible adhesive and 3D-printed highly porous scaffold:

Part 3

Functionalization with antibacterial bio-based silver nanoparticles, antimicrobial and cell viability screening

Abstract

This chapter focuses on the further functionalization of surfaces of 3D-printed PICN, where antimicrobial modification is explored. The antimicrobial properties of the polymer-ceramic composites were achieved by coating them with non-cytotoxic and environmentally safe silver nanoparticles embedded in a phenolated lignin matrix (Ag@PL NPs). Enzymatically phenolated lignin was used as a bio-based reducing agent, to obtain these silver nanoparticles. Ag@PL NPs dispersed in silane (γ-MPS) solution were then deposited on the surface of PICN samples. The presence of the NPs and their proper attachment to the surface were analyzed with spectroscopic methods (FTIR, Raman), and X-ray photoelectron spectroscopy (XPS). Homogeneous distribution and particle size (13.4 ± 3.2 nm) were observed by transmission electron microscopy (TEM) images. The functionalized samples were tested against Gram-positive (*S. aureus*) and Gram-negative (*P. aeruginosa*) bacteria, validating their antimicrobial efficiency. The bacterial reduction of *S. aureus* and *P. aeruginosa* was 90 % and 73 %, respectively, in comparison with the pristine surface of PICN. Based on the obtained data, the functionalized PICN could be used in dentistry, as it shows a high reduction of bacteria in comparison with not-functionalized PICN and also presents high biocompatibility as demonstrated with human fibroblast (BJ-5ta) and keratinocytes (HaCaT) cells.

5.1   Introduction

In recent years, yttria-doped zirconia has gained a lot of attention as yttrium oxide (Y_2O_3) prevents crack propagation in sintered zirconia ceramics [1]–[3]. However, there are still certain drawbacks of the material that prevent its use as a one-piece biomedical prosthesis, like in dental implants, which are composed of titanium screws, polymeric adhesives, and ceramic crown parts [4], [5]. The most important concerns are related to the high brittleness and high Young's modulus of zirconia, which is incompatible with that of alveolar bones [6]; and also its high surface roughness and porosity [7], which are ideal for bacteria growth if compared to titanium implants [8] for example. In Chapter 3, we have successfully combined biocompatible adhesive copolymer with 3D-printed yttria-stabilized tetragonal zirconia scaffolds (3Y-TZP) with 50 % infilled macropores to palliate crack propagation in 3D-printed polymer-infiltrated-ceramic-network (PICN) scaffolds under compression forces (Chapter 4.3.2). Moreover, the hybrid materials conserve their biocompatibility promoting the growth and proliferation of MG-63 osteoblast cells on their surface.

The developed PICN was inspired by the natural composition of teeth, comprised of inorganic and organic components [9], [10]. The infiltration of polyacrylate adhesives in a macro-porous ceramic 3D-printed material was expected to prolong the lifespan of the implant since the polymer adhesive corrects the brittleness problem of the ceramic material [11], [12]. Improvement of 3D-printing techniques has made the design and production fast and easy, providing products of high-end quality [13]– [18]. As was discussed in Chapters 3 and 4, the main advantage is that the design of the pore size and distribution can be controlled with CAD/CAM processes and, therefore, adjusted according to the necessity of the application, which is not possible using traditional sintering methods of compact ceramic structures [19]. PICN sample itself does not apparently promote the growth of bacteria but does not

have antimicrobial properties usually desirable in the biomedical field to prevent biofilm formation [20]. Microbial infections are a continuous threat to human health, primarily with the alarming increase of multi-drug resistant bacteria. An important percentage of these infections are acquired at healthcare facilities (e.g., hospitals and nursing homes) [21]. The incidence of biofilm formation in biomedical implants and devices is a great concern due to the difficulty to treat both the infection and the resulting surgery complications. In fact, bacterial adhesion and subsequent biofilm formation are the major cause of their failure. Thus, there is an urgent need of developing alternative antimicrobial devices, prostheses, and implants to face healthcare-associated infections.

Considering the wide spectrum of antibacterial properties of silver, it has become one of the most popular antibacterial agents. However, in the long-term, the devices containing silver can release Ag^+, which might have cytotoxic effects. Silver nanoparticles receive significant attention, as the form of nanoparticles exhibits much higher reactivity in comparison with bulk material [22], [23], which is a great advantage in treating bacterial infections. AgNPs release metal ions that cause changes in the membrane permeability [24] and/or induce oxidative stress [25], leading to cell death. In addition, metal ions catalyze reactions that produce reactive oxygen species (ROS), causing the oxidation of important cell structures like lipids and DNA [26], [27].

In order to decrease the cytotoxicity associated with metals, different biocompatible natural polymers have been used to produce hybrid metal-polymer NPs [23]. For instance, chitosan was used to produce biocompatible hybrid Ag@chitosan NPs that effectively killed the Gram-positive and Gram-negative bacteria [28].

Lignin gains sizeable attention as a renewable resource for the production of low molar mass compounds or value-added materials [29], [30]. However, the

processability is usually limited due to the low reactivity of lignin. Many efforts have been made to improve the reactivity of lignin, such as methylation (hydroxymethylation), demethylation, amination, and phenolation. The phenolation of lignin is commonly achieved by a chemical method in which lignin is treated with phenol under acidic conditions, leading to the condensation of phenol with lignin side chains [31]. Recently, the green phenolation of lignin was achieved enzymatically using the laccase/mediator system [32]. The highly reactive phenolated lignin (PL) can be used as a reducing agent for metals to synthesize metal NPs in an environmentally friendly route [33].

In this work, we propose the use of bio-based silver phenolated lignin nanoparticles (Ag@PL NPs) to impart antimicrobial activity for ceramic materials with 3D-printed PICN scaffold architecture. Such hybrid material (ceramic and acrylate polymer adhesive) is used in dentistry applications [34]– [36]. The non-shedding surfaces of crowns, teeth, fixed partial dentures, or endosseous implants facilitate the formation of thick biofilms [37]. Due to the high surface tension of methacrylate copolymer adhered to the zirconia platforms, antimicrobial nanoparticle adsorption by the dip-coating process does not work properly. Thus, the surface of PICN samples has been activated with Ag@PL NPs with the help of chemical etching and silane solution adhesion promoters. Therefore, covalent bonds have been achieved with sol-gel technology, employing 3-(trimethoxysilyl)propyl methacrylate (γ-MPS) as an anchoring molecule, and stable antimicrobial PICN scaffolds were obtained for the first time.

5.2   Experimental procedure

5.2.1   Materials

The 3Y-TZP (3 mol% yttria-stabilized tetragonal zirconia polycrystal) powder was supplied by SEPR Saint-Gobain ZirPro (France) under the commercial name CY3Z-R. Protobind 6000 sulfur-free lignin (Mw = 1000 g·mol^{-1}) was purchased from Green Value (Switzerland). The Pluronic® F-127 hydrogel; γ-MPS (3-(trimethoxysilyl) propyl methacrylate); Bis-GMA (bisphenol A glycerolate dimethacrylate); TEGDMA (triethylene glycol dimethacrylate) and BPO (benzoyl peroxide, Luperox®A75,), gallic acid, tannic acid, 3',5'-dimethoxy-4'-hydroxyacetophenone (acetosyringone), silver nitrate, phosphate buffered saline (PBS), Nutrient Broth (NB) and Dulbecco's Modified Eagle's Medium (DMEM) were all purchased from Sigma-Aldrich. AlamarBlue cell viability reagent was purchased from Invitrogen, Life Technologies Corporation (Spain). Laccase enzyme from *Miceliophtora termophila* (Novozym 51003) was provided by Novozymes (Denmark). The enzymatic activity of laccase was 1322 U mL^{-1}, where the amount of enzyme converting 1 μmol of ABTS to its cation radical (ε_{436} = 29 300 M^{-1} cm^{-1}) in 5 mM Britton Robinson buffer with pH 5 at 40 °C. Two bacterial strains *Staphylococcus aureus* (*S. aureus*; ATCC 25923) and *Pseudomonas aeruginosa* (*P. aeruginosa*; ATCC 10145) and human fibroblast (ATCC-CRL-4001, BJ-5ta) and keratinocyte (HaCaT cell line) cells were received from the American Type Culture Collection (ATCC LGC Standards, Spain). In all the experiments water was purified by the Milli-Q plus system (Millipore) with 18.2 MΩ·cm^{-1}resistivity prior to its use.

5.2.2   Synthesis of silver phenolated lignin nanoparticles (Ag@PL NPs)

Ag@PL NPs were synthesized in the laboratory of Molecular and Industrial Biotechnology Group (GMBI, UPC), using phenolated lignin to reduce silver ions as previously described (Figure 5-1 a) [32], [33]. Briefly, lignin was enzymatically phenolated with tannic acid and gallic acid using the laccase/mediator method. Lignin (10 g·L^{-1}) was dispersed in sodium acetate buffer (50 mM, pH 5) where the mediator, acetosyringone, was previously dissolved (1.5 g·L^{-1}). To initiate the

oxidative reaction. laccase at a final concentration of 13.22 U·mL^{-1} (diluted with The PL was separated by centrifugation for 20 min at 4000g from the non-reacted phenolic compounds and freeze-dried. Figure 5-1 b outlines the reaction between the phenolic compounds and lignin. The phenolic content of lignin was analyzed spectrophotometrically as was previously described [33]. The resulting PL was dissolved in water (10 g·L^{-1}), and the pH was adjusted to 8 with 1M NaOH. Afterward, the solution was mixed with 4 mg·mL^{-1}of AgNO$_3$ (lignin:silver ratio = 3:2) and sonicated at 60 °C for 2 h and 50 % amplitude (Sonics and Materials instrument, Ti-horn, 20 kHz). The NPs were purified by centrifugation at 18000g for 40 min. The non-reacted lignin molecules were removed by centrifuging at 500g for 10 min and the resulting pellet was re-suspended in Milli-Q water. The disaggregation of NPs was achieved by low-intensity ultrasonication before usage.
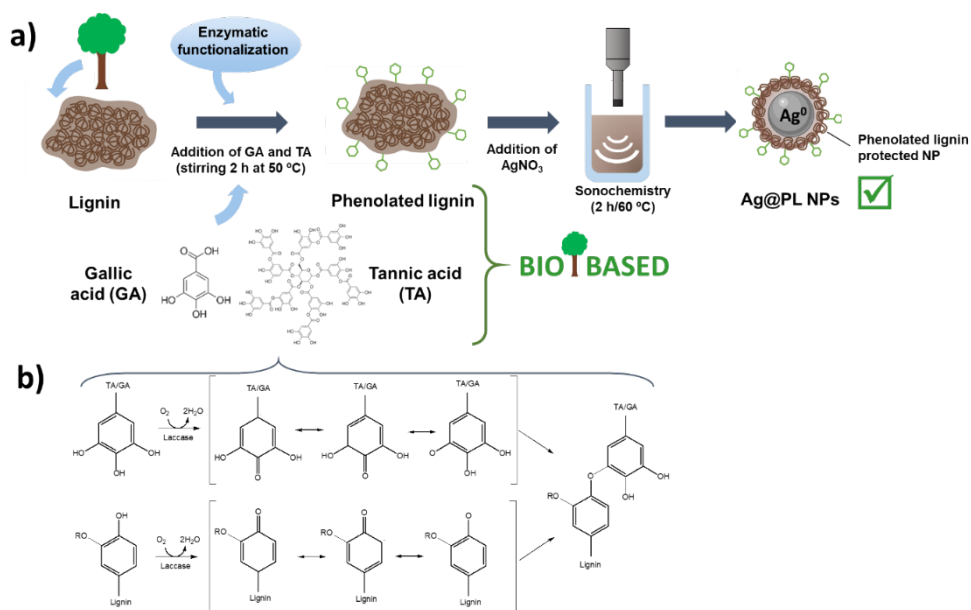
Figure 5-1: Schematic representation of: (a) Ag@PL NPs synthesis and disaggregation of particles with sonochemistry technology before incorporation to PICN scaffolds, and (b) simplified chemical reactions between gallic- and tannic acids and lignin to obtain phenolated lignin compounds.

5.2.3   Deposition of Ag@PL NPs in 3D-printed PICN scaffolds (Ag@PL NPs/PICN)

The detailed procedure of highly porous zirconia scaffolds (PICN) 3D-printing with 3D Dima Elite dispenser (Nordson Dima, Netherlands) equipped with DimaSoft CAD/CAM software, and their impregnation with methacrylate copolymer (Bis-GMA/TEGDMA), were described in Chapter 3.2 and Figure 5-2 a summarizes such a procedure.
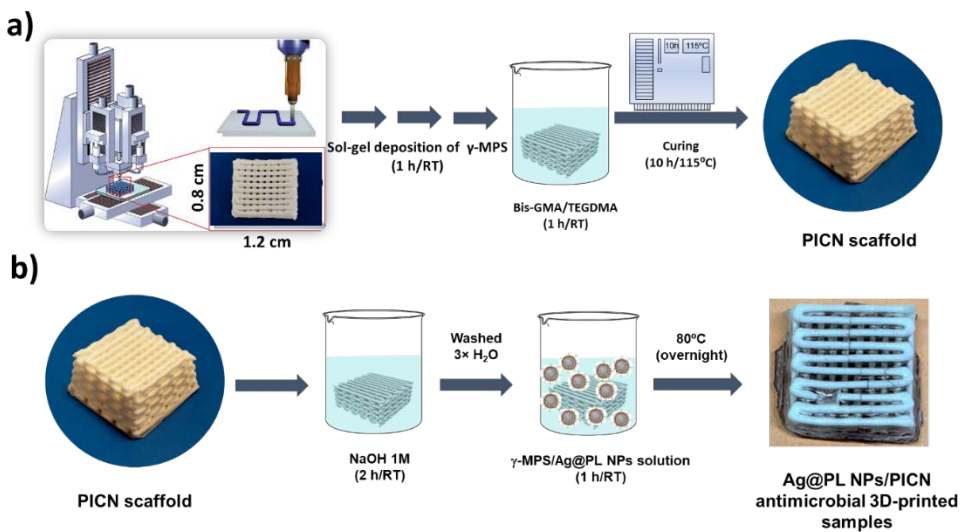
Figure 5-2: Illustration of the design and fabrication process of antimicrobial 3D-printed PICN samples: (a) 3D-printing of 3Y-TZP filaments with 50 % of macropores and infilled with Bis-GMA/TEGDMA copolymer to generate the filled cubic PICN shape, and (b) PICN surface activation with NaOH and posterior adsorption of Ag@PL antimicrobial NPs promoted by sol-gel synthesis (☐-MPS in ethanol: H2O solution). In (a) the printer's drawing has been adapted from the references, with permissions [56], [57].

After the choice of the properly infiltrated 3D samples, PICN scaffolds were superficially activated by dip-coating in an aqueous solution of NaOH (1M) for 2 h at room temperature (r.t.), creating hydroxyls and carboxylate groups for a further anchoring of Ag@PL NPs (Figure 5-2 b). Then, those samples were washed three times with distilled water, and immediately moved to another vessel containing γ-MPS/Ag@PL NPs solution (24 mmol of liquid silane in 100

mL of 3:1 ethanol:Ag@PL NPs water solution, where the concentration of Ag@PL NPs in water was 2.2 µg·mL^{-1}, volume ratio).

The solution was stirred with a magnetic stirrer for 1 h at room temperature before 1 h long PICN immersion. PICN samples were then cured in a drying oven at 80 °C overnight. The absence of particle agglomeration and the homogenous distribution over the polymer and the zirconia filaments were checked by optical microscopy (OLYMPUS BX51).

5.2.4   Characterization techniques

Spectroscopy techniques were used for the chemical characterization of the different steps of obtaining Ag@PL NPs/PICN obtaining. Fourier Transform Infrared Spectroscopy (FTIR) analysis to distinguish the main absorption bands of the functionalized composite was performed by a Jasco 4100 spectrophotometer, which is equipped with an attenuated total reflection accessory with a diamond crystal (Specac model MKII Golden Gate Heated Single Reflection Diamond ATR). In total, 64 scans in the range between 4000 and 600 cm^{-1} were obtained for each sample with a resolution of 4 cm^{-1}. Raman spectroscopy was carried out with a Renishaw dispersive Raman microscope spectrometer (model InVia Qontor, GmbH, Germany) and data were analyzed with Renishaw WiRE software. The spectrometer equipment includes a Leica DM2700 M optical microscope, a thermos electrically cooled charge-coupled device (CCD) detector, and a spectrograph scattered light with 2400 lines mm^{-1} or 1200 lines mm^{-1} of the grating. Experiments were performed with a 785 nm excitation source and with a nominal laser power between 1 mW and 100 mW output power. The exposure time was 10 s, the laser power was adjusted to 1 % of its nominal output power and each spectrum was collected with three accumulations. All Raman spectra were collected in a spectral range from 600 to 4000 cm^{-1} with the same measurement parameters.

The distribution and size of freshly synthesized Ag@PL NPs were evaluated by a Philips TECNAI 10 transmission electron microscope (TEM), manufactured by Philips Electron Optics (Eindhoven, Holland) at an accelerating voltage of 100kV. The particle size was measured with ImageJ software from TEM images and the average particle size was determined based on 100 particle size measurements. Scanning electron microscopy (SEM) was carried out using a Focused Ion Beam Zeiss Neon40 scanning electron microscope equipped with an energy dispersive X-ray analysis (EDX) spectroscopy system and operating at 5 kV. EDX was used to check the presence of Ag atoms on the sample surface. To avoid sample charging problems the cubic structures were attached to a double-side adhesive carbon disc and sputter-coated with a thin layer of carbon.

X-ray photoelectron spectroscopy (XPS) analyses were performed to observe whether the Ag NPs were well adhered to the PICN surfaces, *i.e.,* to prove their conjugation with the ceramic-polymeric scaffold. Assays were performed on a SPECS system equipped with an Al anode XR50 source operating at 150 mW and a Phoibos MCD-9 detector. The pressure in the analysis chamber was always below 6×10^{-9} mbar. The pass energy of the hemispherical analyzer was set at 25 eV and the energy step was set at 0.1 eV. Data processing was performed with the Casa XPS program (Casa Software Ltd., UK). High-resolution XPS spectra were acquired by Gaussian/Lorentzian curve, fitting after S-shape background subtraction, for the following elements: C 1s, O 1s, Si 2p, and Ag 3d. As the internal reference, C 1s peak with a binding energy of 284.8 eV was used.

5.2.5   Antibacterial assays

To assess the antibacterial activity of the Ag@PL NPs/PICN, an adhesion assay towards Gram-positive *S. aureus* and Gram-negative *P. aeruginosa* was carried out. The adhesion of bacteria onto PICN without NPs was used as a reference to better observe the antibacterial effect of Ag@PL NPs. Prior to the

tests, the materials were sterilized under UV light for 30 min, and sterilized tweezers were used to manipulate the samples during the whole process. The bacteria were grown in NB overnight at 37 ºC. A dilution of the inoculum was prepared until the optical density measured at a wavelength of 600 nm (OD_{600}) was of 0.01 (corresponding to $10^5 - 10^6$ CFU/mL). Ag@PL NPs/PICN and PICN samples of 2.0 ± 0.2 g were incubated overnight with 2 mL of bacterial suspension in a 24-well plate at 37 ºC. The differences in the weight of the samples were compensated by adjusting the volume of bacterial suspensions. Then, samples were sequentially washed three times by immersion in 2 mL of sterile PBS to remove the non-adhered bacteria. Finally, the samples were immersed in 2 mL of fresh PBS and the bacterial cells were detached from the Ag@PL NPs/PICN by vortexing for 1 min and sonication for 20 min in an ultrasonic bath (SONIC 6MX Ultrasonic bath, 37 kHz). After removing the materials from the bacterial suspensions, the number of bacteria adhered to the Ag@PL NPs/PICN samples was estimated using the dilution method and plate counting, obtaining the number of colony-forming units (CFU). Results are expressed in a logarithm of number of bacteria, log (CFU·mL^{-1}). The percentage of reduction of adhered bacteria was calculated using PICN as a reference (Eq. 1):

$$\text{Adhesion reduction } (\%) = \left(\frac{A-B}{A}\right) \times 100 \qquad \text{(Equation 1)}$$

where A is the number of bacteria adhered to PICN, and B is the number of bacteria adhered to Ag@PL NPs/PICN. Bacterial suspensions incubated in absence of the materials, either subjected to vortexing and ultrasound, were used as control.

5.2.6   Biocompatibility assays

The biocompatibility of the Ag@PL NPs/PICN and PICN samples was assessed using an indirect method by growing the cells in a medium that was previously

incubated with zirconia samples. Prior to the tests, Ag@PL NPs/PICN and PICN samples (2 g) were incubated in 2 mL DMEM for 24 h or 7 days at 37 ºC. Then, 100 µL of this medium was placed in a 96-well tissue culture-treated polystyrene plate where $6 \cdot 10^4$ cells per well were previously seeded. After incubation at 37 °C in humidified atmosphere of 5 % CO_2 for 24 h, the medium was withdrawn and the cell viability was assessed by incubating the cells with 100 µL of AlamarBlue (10 % v/v in DMEM) for 4 h at 37 ºC. The percentage of cell viability was estimated using the fluorescence values (λ_{ex} = 550 nm, λ_{em} = 590 nm) of the wells containing only cells and AlamarBlue reagent as reference (growth control). Wells containing only AlamarBlue reagent were used as the blank group. The percentage of cell viability was estimated as follows:

$$\text{Cell viability (\%)} = \frac{(\text{Fluorescence}_{\text{sample}} - \text{Fluorescence}_{\text{blank}})}{(\text{Fluorescence}_{\text{growth control}} - \text{Fluorescence}_{\text{blank}})} \times 100$$

(Equation 2)

Cell viability was also evaluated by fluorescence microscopy using the Live/Dead Viability/Cytotoxicity kit (Thermo Fisher Scientific) which stains the live cells in green and in red the dead ones. After removing the culture medium from the wells, 20 µL of staining solution (0.1 % Calcein AM and 0.1 % Ethidium homodimer-1 in PBS) was added. The samples were then incubated in dark for 20 min and later observed with fluorescence microscopy using a 10× objective lens.

5.3   Results and discussions

5.3.1   Functionalization of PICN with Ag@PL NPs antimicrobial particles

The complete characterization of Ag NPs protected with PL was previously introduced by Tzanov and co-workers [33]. The Ag@PL NPs used in this work were prepared following the same procedure and the particle size diameter

measured by TEM was like that previously reported (13.4 ± 3.2 nm) (Figure 5-3 a-d). The activation of 3D-printed PICN with Ag@PL NPs was only possible by quenching the copolymer film surface with NaOH (1M) and, subsequently, anchoring the protected NPs by using sol-gel technology, as described in Section 2.3. Other tested methodologies (e.g. plasma activation and a mixture of Ag@PL NPs with Bis-GMA/TEGDMA monomers prior to copolymerization) failed and no silver atoms could be found on the surface of the cubic structure. Although the small size of the particles makes their observation in the SEM micrographs difficult, Ag atoms were detected by EDX analyses (Figure 5-3 e-f) on the top surface of the PICN 3D-printed structures attached by applying sol-gel technology.
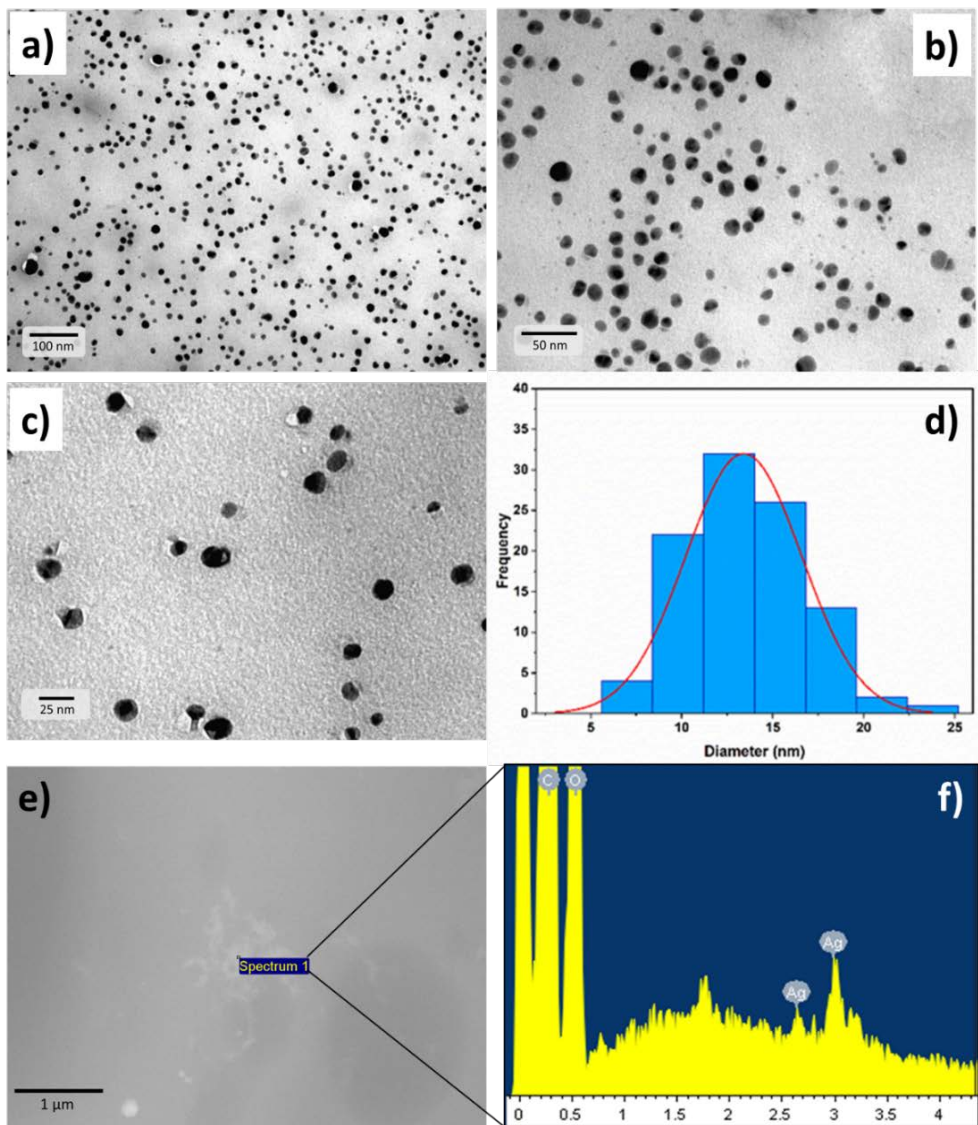
Figure 5-3: (a-c) TEM images of Ag@PL NPs at different magnifications before PICN attachment; (d) nanoparticles distribution by size and frequency; and (e-f) SEM micrograph and EDX spectrum of aggregated Ag@PL NPs above 3D-printed PICN scaffolds. The nanoparticle distribution and size in TEM were analyzed with ImageJ software and it was derived from imaging 100 particles.

Thus, successful adhesion of the bactericide particles was proved by SEM-EDX and, additionally, by optical microscopy (Figure 5-4).
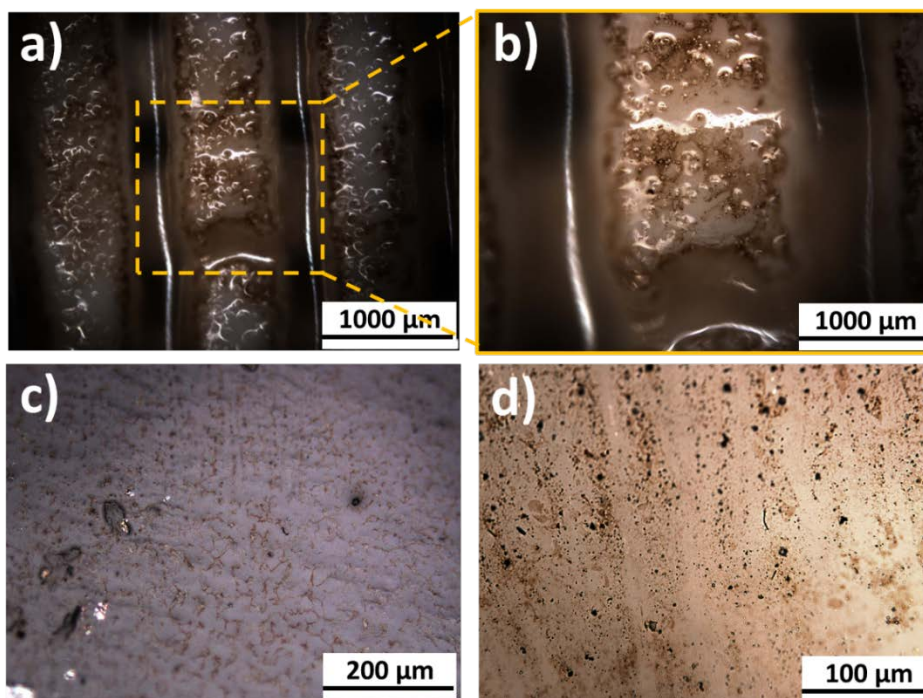
Figure 5-4: Optical micrographs of the surface of PICN filaments showing the adsorption of the Ag@PL NPs: (a-b) top (5× magnification); (c) valley (20× magnification); and (d) valley (50× magnification).

As can be seen in Figure 5-4 (a-b), the natural roughness of the zirconia filaments facilitates the incorporation of the Ag@PL NPs promoted by the sol-gel mixture. A closer inspection outside the top of the filaments (valleys shown in Figure 5-4a) revealed also the homogenous distribution of the Ag@PL NPs inside the methacrylate copolymer film, accused by the dark color particles seen in Figure 5-4 c-d. It should be noted that the optical microscopy only allows for observation of even distribution of the lignin macromolecules, based on what the homogeneity of Ag@Pl NPs distribution was expected.

The high roughness of the 3Y-TZP filaments, after the sintering process at high temperatures, prevents the correct measurement of this property, and it also difficulties the measurements of the hydrophobicity/hydrophilicity

properties of the film, before and after the NPs incorporation.

The characterization of the hybrid material was not an easy task because both the adhesive (acrylate copolymer) and the AgNPs have organic groups very similar in their structures (alcohol, aromatic, aliphatic, and ethers).

Lignin is a complex chemical compound constituting up to a third of the dry mass of plants, depending on the species. This natural biopolymer has a high content of aromatic rings and hydroxyl groups, which were evidenced in the FTIR spectra (Figure 5-5a). The broad and intense band at ~3400 cm^{-1} in Ag@PL NPs corresponds to the high number of hydroxyl groups in the lignin structure. The broadening of such absorption band on the surface of 3D-printed Ag@PL NPs/PICN samples proves the successful incorporation of the NPs promoted by alkali activation. Moreover, C=C vibrations from aromatic rings of both Bis-GMA monomer (copolymer) and lignin are reflected by sharp bands at ~1600 and 1509 cm^{-1}. The peak at 2920 cm^{-1} also includes methylene and methyl bonds of the copolymer and the nanoparticles. However, the most relevant absorption bands that were identified, also in the hybrid material (Ag@PL NPs/PICN), are those associated with the presence of ester and ether linkages at 1712 cm^{-1} (C=O) and at 1100-1160 cm^{-1} (C-O), respectively, from Bis-GMA and TEGDMA units, and also phenolated lignin. Lignin contains C=O groups from unconjugated carbonyl groups (~1705 – 1720 cm^{-1}) and in phenolated lignin the intensity of this peak increases due to the presence of tannic acid and gallic acid (Figure 5-1 b), which also have C=O groups [38]–[42]. Then, the high density of organic groups with low polarity (C=C, =C-H) led us to use Raman spectroscopy to ascertain the presence of other linkages. Figure 5-5 b represents the Raman spectra for PICN and PICN modified with Ag@PL NPs. Clearly, the absorption bands of C=C aromatic (~1600 cm^{-1}) are more intense than C=O (1729 cm^{-1}), while C-H (Ar) is clearly observed at 3072 cm^{-1} due to the complete absence of hydroxyl absorption bands [43], [44]. Moreover, silver nanoparticles' lattice

vibrational modes are also identified at 250 cm^{-1} and at ~1900 cm^{-1} in the region of metal carbonyls, which would suggest an interaction between AgNPs and lignin matrix and stability of the complex [45], [46].
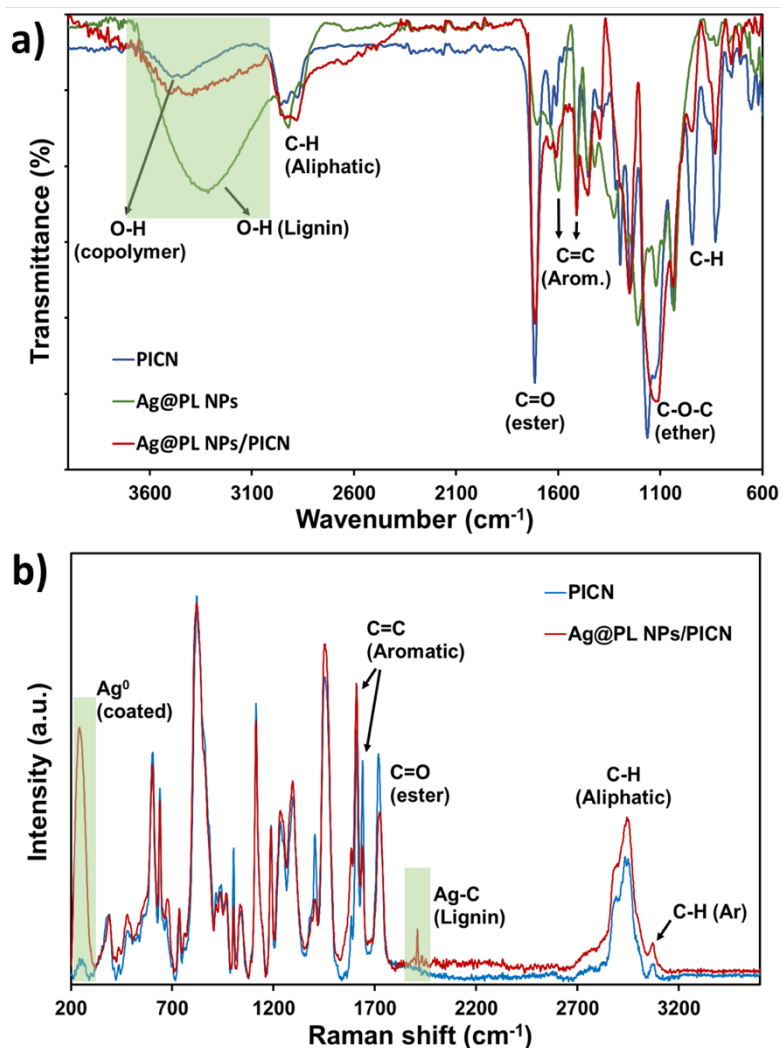
Figure 5-5: (a) FTIR spectra of 3D-printed PICN, dry Ag@PL NPs, and Ag@PL NPs/PICN samples. (b) Raman spectra of PICN and Ag@PL NPs/PICN. The most relevant absorption bands are highlighted in both cases.

Although the spectroscopy characterization confirms the well-assembled AgNPs to the methacrylate adhesive, the nature of such bonding interactions can only be approached by XPS. The survey spectra (Figure 5-6 a) show atoms of C 1s (~285 eV) and O 1s (~530 eV) for all samples, whereas Ag 3d (374 eV and

368 eV) are only present in the pure Ag@PL NPs and Ag@PL NPs/PICN samples. Moreover, the Si 2p binding energies (102 eV) are identified either in PICN or PICN surface modified with the antibacterial particles, as expected, since the copolymer infiltration to the pores of 3D-printed zirconia is also optimized by sol-gel technology, as demonstrated in Chapter 3.

Particularly interesting is the absence of Zr 3d atoms (183 eV) in the survey spectrum of PICN, belonging to the ceramic structure, confirming the well-covered surface of all samples. High-resolution spectra (Figure 5-6 b-e) from C, O, and Si elements confirmed the covalent bonding nature of such atoms with the help of a silanization reaction. Therefore, after silanization, C-O-Si (288 eV, Figure 5-6 b), O-Si (531 eV, Figure 5-6 c), and Si-O-Si and Si-O-C (103 eV and 102 eV Figure 5-6 d) appear in the PICN functionalized surface. Furthermore, the incorporation of Ag@PL NPs in PICN scaffolds is able to maintain the active metallic condition after the sol-gel process of application, showing similar values of binding energies related to the Ag element (374 eV and 368 eV for Ag 3d 3/2 and Ag 3d 5/2, respectively) Figure 5-6 e).

Afterward, the evaluation of the antimicrobial and biocompatibility of the whole system was carried out with Gram-negative and Gram-positive bacteria, and with two cell lines, keratinocyte and fibroblast.
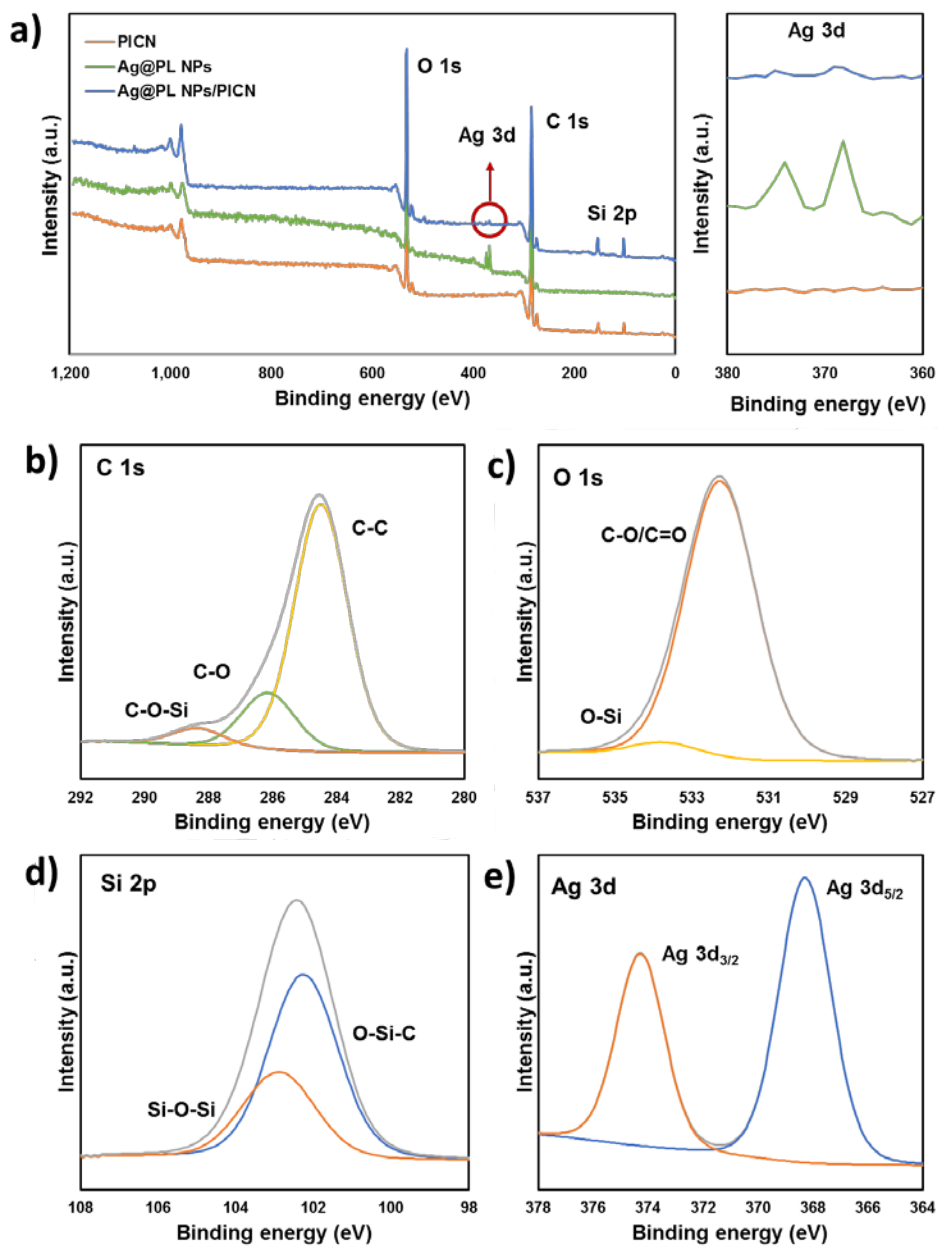
Figure 5-6: (a) XPS survey spectra of PICN, dry Ag@PL NPs, and Ag@PL NPs/PICN samples. (b-e) High resolution spectra of Ag@PL NPs/PICN sample: C 1s (b); O 1s (c); Si 2p (d) and Ag 3d (e).

5.3.2 Effect of the presence of Ag@PL NPs in the antimicrobial properties of PICN scaffolds

There are about 5 billion bacteria in the human oral cavity. The antimicrobial effects of silver nanoparticles are well-known [47], [48]. If PICN scaffolds are intended for future dentistry applications, which was the focus of the research at its preliminary stage, the antibacterial activity of the Ag@PL NPs/PICN should be assessed. For this study, two clinically relevant pathogens (the Gram-positive *S. aureus* and the Gram-negative *P. aeruginosa*), also present in our oral cavity, were chosen. The initial antibacterial activity was assessed by counting the number of bacteria adhered to the surface of Ag@PL NPs/PICN in comparison to that adhered to PICN surfaces (used as control) (Figure 5-7 and Table 5-1).
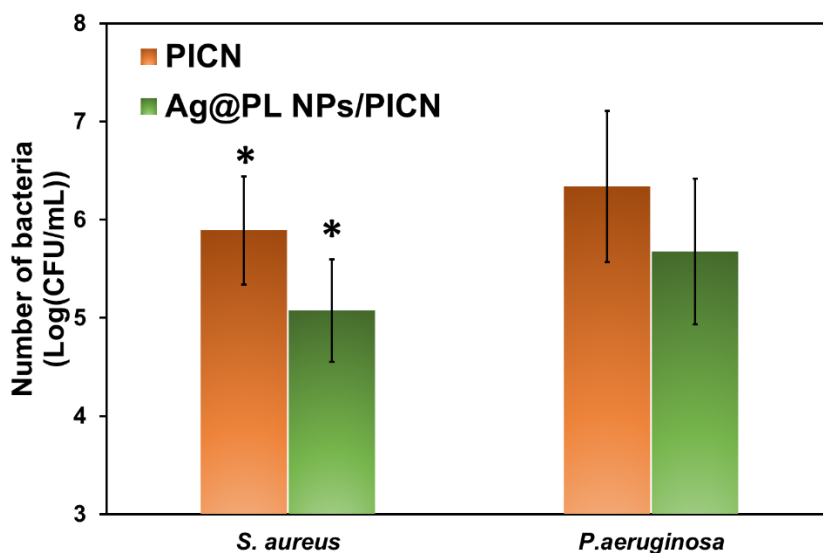
Figure 5-7: The number of bacteria (S. aureus and P. aeruginosa) adhered onto 3D-printed PICN and Ag@PL NPs/PICN scaffolds, expressed in the logarithm of viable bacteria, log(CFU/mL). Results marked with stars are confidence level where p < 0.05, using the Student's T-test. The log (CFU/ml) values can be consulted in Table 5-1.

The number of *S. aureus* adhered onto non-functionalized PICN was 5.89 ± 0.55 log while it was reduced to 5.07 ± 0.52 log for Ag@PL NPs/PICN, corresponding to about 90 % reduction (calculated from CFU/mL) of bacteria

adhered. In the case of *P. aeruginosa*, the number of bacteria decreased from 6.34 ± 0.77 log to 5.68 ± 0.74 log, which corresponds to about 73 % reduction (calculated from CFU/mL) with respect to the non-functionalized PICN surface. Both percentages were calculated by using equation 1 (Section 5.2.5).

Table 5-1: Number of bacteria in log(CFU/mL) adhered to PICN and Ag@PL NPs/PICN. Control refers to bacteria incubated in absence of the materials.

Sample	*S. aureus*	*P. aeruginosa*
PICN	5.89	6.34
Ag@PL NPs/PICN	5.07	5.68
Control	5.81	6.75

The antibacterial effect of Ag NPs is attributed to both their attachment to bacterial cells and the release of Ag^+ ions. Some studies showed that Ag NPs were more effective against Gram-negative bacteria, which was ascribed to their thinner peptidoglycan layer in comparison with Gram-positive bacteria [47]– [49].

In the present work, Ag@PL NPs/PICN were more effective against the Gram-positive bacteria. It should be noted that we have reported higher adhesion of Gram-negative bacteria to PICN scaffolds (without Ag@PL NPs) in our previous Chapter 3.3.4. Moreover, Ag@PL NPs incorporated into polyurethane (PU) foams exhibit high antibacterial activity against *P. aeruginosa* and *S. aureus*, reaching over 4.6 and 5.6 log reduction, respectively [33]. Their higher antibacterial capacity in the foam materials in comparison with Ag@PL NPs/PICN hybrid materials may be due to their different NPs loads. In order to obtain antibacterial PICN materials, we chose an Ag@PL NPs concentration based on previous work, in which the totality of the NPs was incorporated in the foam. However, the efficiency of the deposition of Ag@PL NPs was not 100 %, so the final content of NPs in the materials was lower than expected. This may explain the lower antibacterial activity of PICN scaffolds in comparison with the

PU foams. Other factors that play an important role in bacteria proliferation are the hydrophilicity and roughness of sample surfaces.

Unfortunately, as explained above (chapter 5.3.1), we were unable to measure such properties. However, the samples without and with Ag@PL NPs were prepared with similar conditions and in the same solid substrate (3D-printed). Therefore, it is expected that these factors are similar for both samples and would not greatly affect the results obtained.

5.3.3 Effect of the presence of Ag@PL NPs in the biocompatibility properties of PICN scaffolds

The biocompatibility of implants is a crucial criterion for their biomedical application. In the case of silver-containing implants, the release of Ag may cause cytotoxicity, which is attributed to the generation of ROS, destabilization of the cell membrane, and inactivation of essential enzymes [50], [51]. The cell viability of pure PICN and Ag@PL NPs/PICN samples was assessed *in vitro* employing two different cell models, HaCaT and BJ5ta, which are immortalized cell lines from adult human skin with keratinocyte and fibroblast-like morphology, respectively. The culture media previously pre-incubated with Ag@PL NPs/PICN and PICN samples for 24 h or 7 days was used to grow the cells for 24 h, while a fresh medium which has not been in contact with the samples was used to grow control cells. Figure 5-8 and 5-9 a display quantitative results, which correspond to the average of three independent replicas for each system, and they are expressed in terms of cell viability relative to control cells. Furthermore, the microscopy images of the cell viability study showing the cells stained with AlamarBlue can be seen in Figure 5-8 b and 5-9 b.
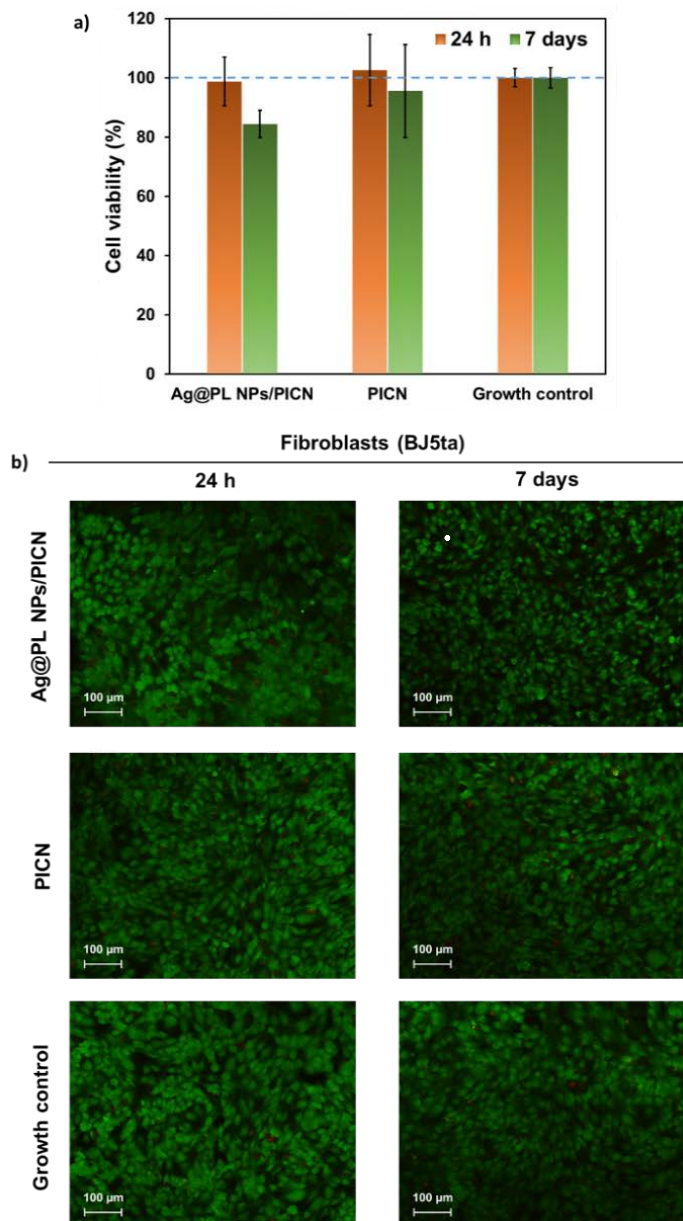
Figure 5-8: (a) Cell viability and proliferation (%) of human fibroblast-like (BJ5ta) incubated with medium previously exposed to Ag@PL NPs/PICN and PICN samples for 24 h or 7 days. The control is related to the media without the 3D-printed pieces. (b) Microscopy images of live/death assay of human fibroblasts incubated with medium exposed to Ag@PL NPs/PICN and PICN for 24h and 7 days. The assay stains (AlamarBlue) the live cells in green and the dead ones in red. One representative image of each experimental group (three replicates) was chosen. Growth control refers to cells incubated with fresh medium.
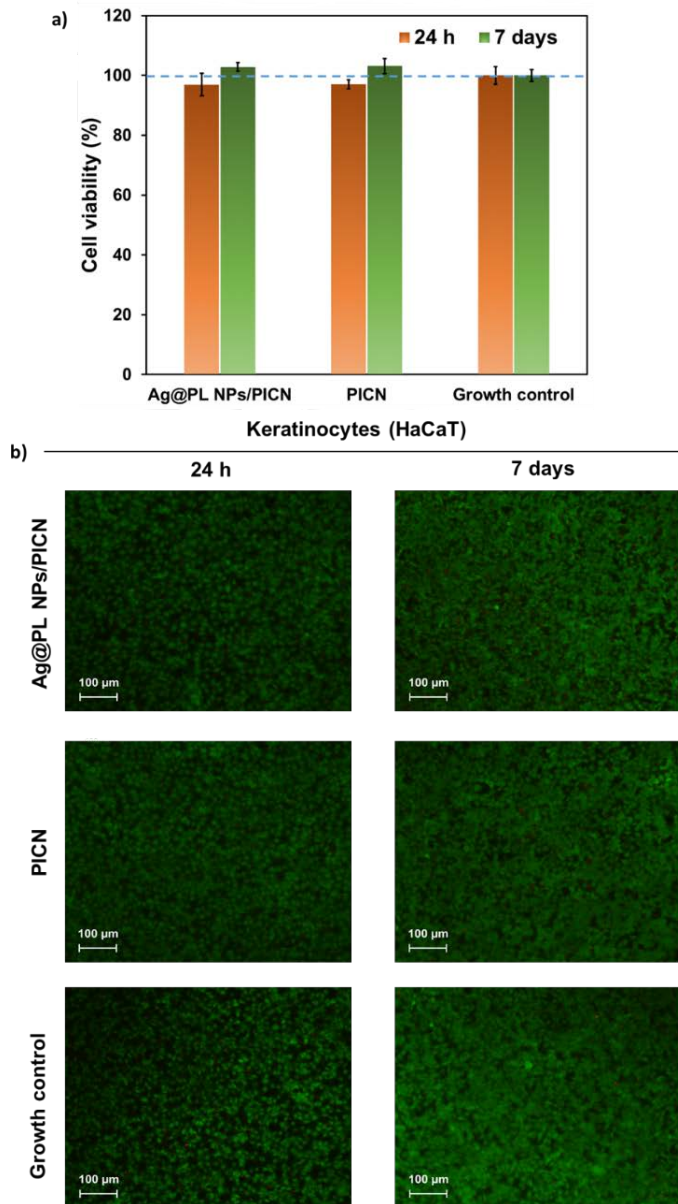
Figure 5-9: (a) Cell viability and proliferation (%) of human keratinocyte cells (HaCaT) incubated with medium previously exposed to Ag@PL NPs/PICN and PICN samples for 24 h or 7 days. The control is related to the media without the 3D-printed pieces. (b) Microscopy images of live/death assay of human fibroblasts and keratinocytes incubated with medium exposed to Ag@PL NPs/PICN and PICN for 24h and 7 days. The assay stains (AlamarBlue) the live cells in green and the dead ones in red. One representative image of each experimental group (three replicates) was chosen. Growth control refers to cells incubated with fresh medium.

As shown, the number of viable cells is similar to that of the control, for both cell lines (BJ5ta and HaCaT). This behavior was maintained for Ag@PL NPs/PICN, indicating that the functionalization with Ag@PL NPs does not have a major impact

on the viability of the cells. Even after 7 days, the media incubated with Ag@PL NPs/PICN only slightly decreased the viability of the cell lines down to 97 %, in the case of fibroblast cells (Figure 5-8 a). After 7 days of incubation of Ag@PL NPs/PICN

in the medium, a certain amount of Ag@PL NPs was probably released from the scaffold to medium. Once in contact with the fibroblast cells, the released NPs slightly affected the cell viability (reduction to 84 %), as can be seen in the same plot. While the viability of keratinocyte cells (HaCaT) was slightly higher for both Ag@PL NPs/PICN and PICN than for the control (Figure 5-9 a). Therefore, the opposite behavior was found for keratinocytes cells. On the other hand, the fact that HaCaT cells systematically exhibit higher proliferation than BJ5ta cells has been attributed to the high capacity of the former to differentiate and proliferate in vitro [52]. Overall, cell viability results for both PICN and Ag@PL NPs/PICN samples were higher than 80 % in all cases, independently of the cell line, which is an acceptable value for biomedical applications [53], [54] [55]. The high cell viability values found did not decrease when PICN scaffolds were functionalized with antimicrobial NPs, indicating that neither PICN nor Ag@PL NPs induce cytotoxic effects in vitro against keratinocytes and fibroblasts-like cells. This important conclusion is supported by representative microscopy images of BJ5ta and HaCaT, in which we can appreciate the cells growth (Figure 5-8 b and Figure 5-9 b). As it can be seen, the live/dead staining represented in the images is consistent with the viabilities displayed in Figure 5-8 a – Figure 5-9 a, most of the cells remain alive after 24h and 7 days of incubation. Thus, the high cell viability has been associated with the biocompatibility of the control and studied substrates.

5.4   Conclusions

In the present work, a successful reduction of Gram-positive and Gram-negative bacteria above the PICN surfaces functionalized with silver nanoparticles has been achieved. Enzymatically-phenolated lignin has been used as a reducing agent to obtain stable and biocompatible silver NPs. The challenge of attaching Ag@PL NPs to the surface has been overcome by combining the Ag@PL NPs with silane (γ-MPS) as a coupling agent between the zirconia surface and the polymer structure.

The permanent attachment of the NPs has been proven by multiple techniques described above, including X-ray photoelectron spectroscopy, where a clear peak of Ag 3d binding energy is present in the functionalized samples. Moreover, the results show the Ag@PL NPs/PICN structure's capacity to avoid bacteria's adhesion onto their surfaces, which is attributed to the bactericidal effect of silver in form of NPs, without detriment to the viability of human cell lines. Therefore, such a hybrid scaffold has demonstrated to be a promising biomaterial for applications in one-, and two-piece implants, crowns, or abutment screws, among other dentistry tools.

5.5   References

[1]   C. Gautam, J. Joyner, A. Gautam, J. Rao, and R. Vajtai, "Zirconia based dental ceramics: structure, mechanical properties, biocompatibility and applications," *Dalton Transactions*, vol. 45, no. 48, pp. 19194–19215, Dec. 2016, doi: 10.1039/C6DT03484E.

[2]   K. Srigurunathan, R. Meenambal, A. Guleria, D. Kumar, J. M. D. F. Ferreira, and S. Kannan, "Unveiling the Effects of Rare-Earth Substitutions on the Structure, Mechanical, Optical, and Imaging Features of ZrO2 for Biomedical Applications," *ACS Biomaterials Science and Engineering*, vol. 5, no. 4, pp. 1725–1743, 2019, doi: 10.1021/acsbiomaterials.8b01570.

[3] A. C. Branco *et al.*, "Suitability of 3D printed pieces of nanocrystalline zirconia for dental applications," *Dental Materials*, vol. 36, no. 3, pp. 442–455, 2020, doi: 10.1016/j.dental.2020.01.006.

[4] F. Nejatidanesh, M. Abbasi, G. Savabi, M. Bonakdarchian, R. Atash, and O. Savabi, "Five year clinical outcomes of metal ceramic and zirconia-based implant-supported dental prostheses: A retrospective study," *Journal of Dentistry*, vol. 100, no. June, 2020, doi: 10.1016/j.jdent.2020.103420.

[5] F. Zarone, M. I. di Mauro, G. Spagnuolo, E. Gherlone, and R. Sorrentino, "Fourteen-year evaluation of posterior zirconia-based three-unit fixed dental prostheses: A Prospective clinical study of all ceramic prosthesis," *Journal of Dentistry*, vol. 101, no. March, 2020, doi: 10.1016/j.jdent.2020.103419.

[6] D. Ziskind, M. Hasday, S. R. Cohen, and H. D. Wagner, "Young's modulus of peritubular and intertubular human dentin by nano-indentation tests," *Journal of Structural Biology*, vol. 174, no. 1, pp. 23–30, Apr. 2011, doi: 10.1016/j.jsb.2010.09.010.

[7] S. Zinelis, A. Thomas, K. Syres, N. Silikas, and G. Eliades, "Surface characterization of zirconia dental implants," *Dental Materials*, vol. 26, no. 4, pp. 295–305, 2010, doi: 10.1016/j.dental.2009.11.079.

[8] C. M. Abraham, "A Brief Chronological Review of Dental Implant History," *The Open Dentistry Journal*, vol. 8, pp. 50–55, 2014.

[9] W. Li and J. Sun, "Effects of ceramic density and sintering temperature on the mechanical properties of a novel polymer-infiltrated ceramic-network zirconia dental restorative (filling) material," *Medical Science Monitor*, vol. 24, pp. 3068–3076, 2018, doi: 10.12659/MSM.907097.

[10] A. Coldea, M. v. Swain, and N. Thiel, "Mechanical properties of polymer-infiltrated-ceramic-network materials," *Dental Materials*, vol. 29, no. 4, pp. 419–426, 2013, doi: 10.1016/j.dental.2013.01.002.

[11] L. C. Hwa, S. Rajoo, A. M. Noor, N. Ahmad, and M. B. Uday, "Recent advances in 3D printing of porous ceramics: A review," *Current Opinion in Solid State and Materials Science*, vol. 21, no. 6, pp. 323–347, 2017, doi: 10.1016/j.cossms.2017.08.002.

[12] A. Jonhson, P. Sinthuprasirt, H. Fathi, and S. Pollington, "Current Glass-Ceramic Systems Used in Dentistry," in *Current Trends on Glass and*

Ceramic Materials, S. H. Nandyala and J. dos Santos, Eds. Sharjak: Bentham Science Publishers, 2013, pp. 49–72.

[13]   G. B. Brown, G. Fräns Currier, O. Kadioglu, and J. P. Kierlb, "Accuracy of 3-dimensional printed dental models reconstructed from digital intraoral impressions," *American Journal of Orthodontics and Dentofacial Orthopedics*, vol. 154, pp. 733–739, 2018, doi: 10.1016/j.ajodo.2018.06.009.

[14]   B. Vandenberghe, "The digital patient – Imaging science in dentistry," *Journal of Dentistry*, vol. 74, no. February, pp. S21–S26, 2018, doi: 10.1016/j.jdent.2018.04.019.

[15]   D. Zhang *et al.*, "A 3D-printing method of fabrication for metals, ceramics, and multi-materials using a universal self-curable technique for robocasting," *Materials Horizons*, vol. 7, no. 4, pp. 1083–1090, 2020, doi: 10.1039/c9mh01690b.

[16]   A. Dawood, B. M. Marti, V. Sauret-Jackson, and A. Darwood, "3D printing in dentistry," *British Dental Journal*, vol. 219, no. 11, pp. 521–529, 2015, doi: 10.1038/sj.bdj.2015.914.

[17]   R. B. Osman, A. J. van der Veen, D. Huiberts, D. Wismeijer, and N. Alharbi, "3D-printing zirconia implants; a dream or a reality? An in-vitro study evaluating the dimensional accuracy, surface topography and mechanical properties of printed zirconia implant and discs," *Journal of the Mechanical Behavior of Biomedical Materials*, vol. 75, no. June, pp. 521–528, 2017, doi: 10.1016/j.jmbbm.2017.08.018.

[18]   B. S. Unnikrishnan, G. U. Preethi, M. Joseph, Manu, J. S. Melo, T. T. Sreelekha, and A. Tripathi, "Dental Implants," in *3D Printing in Medicine*, 1st ed., D. Thomas and D. Singh, Eds. Woodhead Publishing, 2019, pp. 168–208. doi: 10.33029/9704-5163-2-pri-2019-1-240.

[19]   J. Li *et al.*, "Mechanical performance of polymer-infiltrated zirconia ceramics," *Journal of Dentistry*, vol. 58, pp. 60–66, 2017, doi: 10.1016/j.jdent.2017.01.008.

[20]   Y. Wang, H. Hua, H. Liu, M. Zhu, and X. X. Zhu, "Surface Modification of ZrO2Nanoparticles and Its Effects on the Properties of Dental Resin Composites," *ACS Applied Bio Materials*, vol. 3, no. 8, pp. 5300–5309, 2020, doi: 10.1021/acsabm.0c00648.

[21]   J. Sjollema *et al.*, "In vitro methods for the evaluation of antimicrobial surface designs," *Acta Biomaterialia*, vol. 70. pp. 12–24, 2018. doi: 10.1016/j.actbio.2018.02.001.

[22]   E. Lizundia *et al.*, "Synergic Effect of Nanolignin and Metal Oxide Nanoparticles into Poly(l-lactide) Bionanocomposites: Material Properties, Antioxidant Activity, and Antibacterial Performance," *ACS Applied Bio Materials*, vol. 3, no. 8, pp. 5263–5274, 2020, doi: 10.1021/acsabm.0c00637.

[23]   A. P. Richter *et al.*, "An environmentally benign antimicrobial nanoparticle based on a silver-infused lignin core," *Nature Nanotechnology*, vol. 10, no. 9, pp. 817–823, 2015, doi: 10.1038/nnano.2015.141.

[24]   W. K. Jung, H. C. Koo, K. W. Kim, S. Shin, S. H. Kim, and Y. H. Park, "Antibacterial activity and mechanism of action of the silver ion in Staphylococcus aureus and Escherichia coli," *Applied and Environmental Microbiology*, vol. 74, no. 7, pp. 2171–8, Apr. 2008, doi: 10.1128/AEM.02001-07.

[25]   S. Gurunathan, J. W. Han, A. Abdal Dayem, V. Eppakayala, and J. H. Kim, "Oxidative stress-mediated antibacterial activity of graphene oxide and reduced graphene oxide in Pseudomonas aeruginosa," *International Journal of Nanomedicine*, vol. 7, pp. 5901–5914, Nov. 2012, doi: 10.2147/IJN.S37397.

[26]   B. Halliwell and J. M. C. Gutteridge, "Role of free radicals and catalytic metal ions in human disease: An overview," *Methods in Enzymology*, vol. 186, no. C, pp. 1–85, Jan. 1990, doi: 10.1016/0076-6879(90)86093-B.

[27]   J. A. Imlay and S. Linn, "DNA damage and oxygen radical toxicity," *Science Science*, vol. 240, no. 4857, pp. 1302–1309, Jun. 1988, doi: 10.1126/science.3287616.

[28]   A. Francesko, M. Cano Fossas, P. Petkova, M. M. Fernandes, E. Mendoza, and T. Tzanov, "Sonochemical synthesis and stabilization of concentrated antimicrobial silver-chitosan nanoparticle dispersions," *Journal of Applied Polymer Science*, vol. 134, no. 30, p. 45136, Aug. 2017, doi: 10.1002/app.45136.

[29]   Ľ. Hodásová *et al.*, "Lignin, potential products and their market value," *Wood research*, vol. 60, no. 6, pp. 973–986, 2015.

[30]   H. Shokrani *et al.*, "Green Polymer Nanocomposites for Skin Tissue Engineering," 2022, doi: 10.1021/acsabm.2c00313.

[31]   X. Jiang, J. Liu, X. Du, Z. Hu, H. M. Chang, and H. Jameel, "Phenolation to Improve Lignin Reactivity toward Thermosets Application," *ACS Sustainable Chemistry and Engineering*, vol. 6, no. 4, pp. 5504–5512, 2018, doi: 10.1021/acssuschemeng.8b00369.

[32]   E. Aracri, C. Díaz Blanco, and T. Tzanov, "An enzymatic approach to develop a lignin-based adhesive for wool floor coverings," *Green Chemistry*, vol. 16, no. 5, p. 2597, 2014, doi: 10.1039/c4gc00063c.

[33]   A. G. Morena, I. Stefanov, K. Ivanova, S. Pérez-Rafael, M. Sánchez-Soto, and T. Tzanov, "Antibacterial polyurethane foams with incorporated lignin-capped silver nanoparticles for chronic wound treatment," *Industrial and Engineering Chemistry Research*, vol. 59, no. 10, pp. 4504–4514, 2020, doi: 10.1021/acs.iecr.9b06362.

[34]   K. Li, H. Kou, J. Rao, C. Liu, and C. Ning, "Fabrication of enamel-like structure on polymer-infiltrated zirconia ceramics," *Dental Materials*, vol. 37, no. 4, pp. e245–e255, 2021, doi: 10.1016/j.dental.2021.01.002.

[35]   S. Wille, K. Sieper, and M. Kern, "Wear resistance of crowns made from different CAM/CAD materials," *Dental Materials*, pp. 1–7, 2021, doi: 10.1016/j.dental.2021.03.017.

[36]   M. v. Swain, A. Coldea, A. Bilkhair, and P. C. Guess, "Interpenetrating network ceramic-resin composite dental restorative materials," *Dental Materials*, vol. 32, no. 1, pp. 34–42, 2016, doi: 10.1016/j.dental.2015.09.009.

[37]   M. Hisbergues, S. Vendeville, and P. Vendeville, "Review zirconia: Established facts and perspectives for a biomaterial in dental implantology," *Journal of Biomedical Materials Research - Part B Applied Biomaterials*, vol. 88, no. 2, pp. 519–529, 2009, doi: 10.1002/jbm.b.31147.

[38]   Z. Tian, L. Zong, R. Niu, X. Wang, Y. Li, and S. Ai, "Recovery and characterization of lignin from alkaline straw pulping black liquor: As feedstock for bio-oil research," *Journal of Applied Polymer Science*, vol. 132, no. 25, pp. 1–9, 2015, doi: 10.1002/APP.42057.

[39]   Y. Xue, X. Qiu, Z. Liu, and Y. Li, "Facile and Efficient Synthesis of Silver Nanoparticles Based on Biorefinery Wood Lignin and Its Application as

the Optical Sensor," *ACS Sustainable Chemistry and Engineering*, vol. 6, no. 6, pp. 7695–7703, 2018, doi: 10.1021/acssuschemeng.8b00578.

[40] X. Liang *et al.*, "Thermal kinetics of a lignin-based flame retardant," *Polymers (Basel)*, vol. 12, no. 9, 2020, doi: 10.3390/POLYM12092123.

[41] B. Jiang, Y. Zhang, L. Gu, W. Wu, H. Zhao, and Y. Jin, "Structural elucidation and antioxidant activity of lignin isolated from rice straw and alkali-oxygen black liquor," *International Journal of Biological Macromolecules*, vol. 116, pp. 513–519, 2018, doi: 10.1016/j.ijbiomac.2018.05.063.

[42] H. Mou, J. Huang, W. Li, X. Wu, Y. Liu, and H. Fan, "Study on the chemical modification of alkali lignin towards for cellulase adsorbent application," *International Journal of Biological Macromolecules*, vol. 149, pp. 794–800, 2020, doi: 10.1016/j.ijbiomac.2020.01.229.

[43] A. Ertani, S. Nardi, O. Francioso, D. Pizzeghello, A. Tinti, and M. Schiavon, "Metabolite targeted analysis and physiological traits of zea mays L. In response to application of a leonardite-humate and lignosulfonate-based products for their evaluation as potential biostimulants," *Agronomy*, vol. 9, no. 8, pp. 1–18, 2019, doi: 10.3390/agronomy9080445.

[44] E. Melro, A. Filipe, D. Sousa, B. Medronho, and A. Romano, "Revisiting lignin: A tour through its structural features, characterization methods and applications," *New Journal of Chemistry*, vol. 45, no. 16, pp. 6986–7013, 2021, doi: 10.1039/d0nj06234k.

[45] T. Gong, Z. Y. Hong, C. H. Chen, C. Y. Tsai, L. de Liao, and K. V. Kong, "Optical Interference-Free Surface-Enhanced Raman Scattering CO-Nanotags for Logical Multiplex Detection of Vascular Disease-Related Biomarkers," *ACS Nano*, vol. 11, no. 3, pp. 3365–3375, 2017, doi: 10.1021/acsnano.7b00733.

[46] Y. Cai, X. Piao, W. Gao, Z. Zhang, E. Nie, and Z. Sun, "Large-scale and facile synthesis of silver nanoparticles: Via a microwave method for a conductive pen," *RSC Advances*, vol. 7, no. 54, pp. 34041–34048, 2017, doi: 10.1039/c7ra05125e.

[47] J. S. Kim *et al.*, "Antimicrobial effects of silver nanoparticles," *Nanomedicine: Nanotechnology, Biology, and Medicine*, vol. 3, no. 1, pp. 95–101, 2007, doi: 10.1016/j.nano.2006.12.001.

[48]   T. C. Dakal, A. Kumar, R. S. Majumdar, and V. Yadav, "Mechanistic basis of antimicrobial actions of silver nanoparticles," *Frontiers in Microbiology*, vol. 7, no. NOV, pp. 1–17, 2016, doi: 10.3389/fmicb.2016.01831.

[49]   A. Barapatre, K. R. Aadil, and H. Jha, "Synergistic antibacterial and antibiofilm activity of silver nanoparticles biosynthesized by lignin-degrading fungus," *Bioresources and Bioprocessing*, vol. 3, no. 1, 2016, doi: 10.1186/s40643-016-0083-y.

[50]   A. Avalos, A. I. Haza, D. Mateo, and P. Morales, "Cytotoxicity and ROS production of manufactured silver nanoparticles of different sizes in hepatoma and leukemia cells," *Journal of Applied Toxicology*, vol. 34, no. 4, pp. 413–423, Apr. 2014, doi: 10.1002/jat.2957.

[51]   J. Zhang, F. Wang, S. S. K. Yalamarty, N. Filipczak, Y. Jin, and X. Li, "Nano Silver-Induced Toxicity and Associated Mechanisms," *International Journal of Nanomedicine*, vol. 17, no. April, pp. 1851–1864, 2022, doi: 10.2147/IJN.S355131.

[52]   N. Schürer, A. Köhne, V. Schliep, K. Barlag, and G. Goerz, "Lipid composition and synthesis of HaCaT cells, an immortalized human keratinocyte line, in comparison with normal human adult keratinocytes," *Exp Dermatol*, vol. 2, no. 4, pp. 179–185, 1993, doi: 10.1111/J.1600-0625.1993.TB00030.X.

[53]   A. Francesko *et al.*, "Bottom-up Layer-by-Layer Assembling of Antibacterial Freestanding Nanobiocomposite Films," *Biomacromolecules*, vol. 19, no. 9, pp. 3628–3636, 2018, doi: 10.1021/acs.biomac.8b00626.

[54]   G. Ferreres, A. Bassegoda, J. Hoyo, J. Torrent-Burgués, and T. Tzanov, "Metal-Enzyme Nanoaggregates Eradicate Both Gram-Positive and Gram-Negative Bacteria and Their Biofilms," *ACS Applied Materials and Interfaces*, vol. 10, no. 47, pp. 40434–40442, 2018, doi: 10.1021/acsami.8b14949.

[55]   I. INTERNATIONAL STANDARD, "Biological evaluation of medical devices-Part 5: Tests for in vitro cytotoxicity," ISO 10993-5:2009, 2009

[56]   J. E. Smay, G. M. Gratson, R. F. Shepherd, J. Cesarano, and J. A. Lewis, "Directed colloidal assembly of 3D periodic structures," *Advanced Materials*, vol. 14, no. 18, pp. 1279–1283, 2002, doi: 10.1002/1521-4095(20020916)14:18<1279::AID-ADMA1279>3.0.CO;2-A.

[57]   D. Therriault, R. F. Shepherd, S. R. White, and J. A. Lewis, "Fugitive inks for direct-write assembly of three-dimensional microvascular networks," *Advanced Materials*, vol. 17, no. 4, pp. 395–399, 2005, doi: 10.1002/adma.200400481.

06

Atmospheric pressure plasma liquid assisted deposition of polydopamine/acrylate copolymer on zirconia (Y-TZP) ceramics: a biocompatible and adherent nanofilm

Abstract

Chapter 6 of this thesis describes the potential of polydopamine-ethylene glycol dimethacrylate copolymer coating, to promote cell adhesion and antibiofilm formation. This coating has been used on stainless steel in the past with excellent results, however, the application to zirconia has not been described. Thus, this fact makes it an interesting addition to the possibilities of zirconia surface modifications for dentistry. In the case of this study, ultra-smooth yttria-stabilized zirconia discs with an average roughness of 2.08 ± 0.08 nm were used. The nanometric coating (250 nm) was deposited on the surface by liquid-assisted atmospheric-pressure plasma-induced polymerization (LA-APPiP). The successful covalent bonding of the copolymer with the zirconia surface, thanks to the previous activation of the substrate with oxygen plasma, was proved by X-ray photoelectron spectroscopy (XPS). Based on the results, the LA-APPiP technique seems to be an excellent method to produce homogenous films without the need of employing solvents and further purification steps. To complete the study, it was observed that the zirconia discs with the biocompatible coating allow the uniform growth of human osteoblast-like MG-63 cells, after 7 days of cell culture.

6.1   Introduction

The use of bioceramic materials in dentistry and medicine has been increasing in the last decades due to the facile modulation of their dynamic properties and the simplicity of the required fabrication processes [1]. For instance, 3D-printing technology is gaining force for ceramic tools production and has partially replaced the conventional cold isostatic pressing and sintering process [2]–[5], as was also discussed in Chapters 3 and 4. Among ceramic compounds, yttria-stabilized tetragonal zirconia polycrystal (Y-TZP) has shown great promise in many applications, such as hip joint replacement, dental implants, and long-span bridges [6]–[8]. Moreover, Y-TZP biomedical implants offer important advantages, which can be summarized as follows: (i) high affinity to bone tissue; (ii) biocompatible and non-carcinogenic properties; (iii) proved nucleation site service for calcium-based mineral growth, essential for bone restoration; (iv) avoidance of bluish discoloration, usually observed in titanium prosthesis; and (v) light-weight when compared to metal implants and not prone to corrode if compared to other metals as well.

Particularly, in the dental industry, there is a significant interest in producing surface treatments on zirconia-based substrates to achieve enhanced fibroblast adherence, decrease biofilm formation, and focus on therapeutic aims [9]–[11]. The objective is to improve osseointegration and antimicrobial activity in order to reduce the percentage of biomaterial rejections once implanted [12]–[15]. In addition to traditional surface pre-treatments, like chemical etching, grit blasting or machining, laser ablation, UV-light radiation [10], [14], [16]–[18], and coating deposition by using dip-coating methods, as the sol-gel technology [19]–[21], there is nowadays a plethora of friendly and advantageous bottom-up approaches that lead to the obtaining of hybrid materials of great interest. In this sense, atmospheric plasma technology has proved to be a time- and resource-efficient one-step process able to control the hydrophobicity of solid

surfaces and useful to completely eradicate the use of solvents and co-additives in the preparation of organic and inorganic cladding hybrid systems [17], [22]–[24].

In this work, for the first time, organically modified Y-TZP discs containing polydopamine and acrylate biocompatible polymer were successfully prepared by applying liquid-assisted atmospheric-pressure plasma-induced polymerization (LA-APPiP). The nanocoating was designed to contain polydopamine molecules [25]–[27], which promote surface adhesion due to catecholamine groups [28] and biominerals formation [29], [30], such as calcium phosphates and hydroxyapatites, that are responsible for the rapid osseointegration of medical implants [31], [32]. Moreover, the acrylate polymer, ethylene glycol dimethacrylate (EGDMA), exhibits biocompatibility, and insignificant cytotoxicity, and is extendedly used in the dental field as an adhesive between the titanium screw and the ceramic crown of a dental implant [33], [34]. EGDMA as a monomer is a base for synthesizing other ethylene glycol dimethacrylates, where a higher number of ethylene glycol functional groups increases the hydrophilicity of such polymers [34]. It is also often used as a viscosity controller in copolymer formations with Bis-GMA, as it has a lower molecular weight [35]. TEGDMA, the viscosity controller monomer used in previous chapters is also a derivative of the EGDMA compound. An in-depth discussion on acrylate monomers can be found in Chapter 1.3.1.

Regarding dopamine units/derivatives, for instance, Lee and co-workers [36] have demonstrated the enhanced biocompatibility of the zirconia surface modified with 3,4-dihydroxy-L-phenylalanine (L-DOPA) films. Those authors employed an aqueous base solution (dip-coating method) for the zirconia surface modification. The chemical structure of the coating and the film topography were evaluated by X-ray photoelectron spectroscopy (XPS) and atomic force microscopy (AFM), respectively. Additionally, hybrid organic-

inorganic surface materials are usually fabricated by layer-by-layer (LbL) assembly [37]. However, such technology is being disused due to both: i) the high amount of raw material and solvents resources needed; and ii) the long synthesis process, which is not fully cost-effective and environmentally compliant for market applications.

LA-APPiP is a powerful alternative for Y-TZP surface functionalization based on the abovementioned drawbacks. Moreover, the dopamine and the monomers supplied for the copolymer preparation are not only commercially available but also relatively inexpensive reagents. Therefore, the novelty of the present work relies on the first-time successful covalent deposition of polydopamine-co-polymethacrylate films on the surface of a ceramic substrate by applying atmospheric plasma deposition. Such technology offers the possibility of fast polymer formation and it is scalable for future commercial uses.

The physical and chemical changes on the Y-TZP surface were approached, before and after oxygen-plasma pre-treatment, and after the nanocoating polymerization by LA-APPiP. The precise characterization of the hybrid material surface chemistry is of paramount importance since its properties determine the possible practical applications in the biomedical field. As the substrate material, zirconia is widely used in dentistry, for the cell viability and adhesion properties evaluation, MG-63 osteoblast cells were cultured with the samples used in the present study. MG-63 cells are one of the most employed osteoblast-like cells used for *in vitro* biocompatibility approach with biomedical materials, for example, stainless steel, titanium, zirconia, and methacrylate adhesives used in the dentistry field.[10], [19], [38]–[40]

6.2 Experimental section

6.2.1 Materials

AMES Group supplied yttria-stabilized zirconia (Y-TZP) rods. The fine-grained zirconia was stabilized with a 2.5% molar of Y_2O_3. The chemical composition of such sintered raw material is: ZrO_2 (94.55 %); Y_2O_3 (5.2 %); and Al_2O_3 (0.25 %). The zirconia discs (diameter of 8.00 mm and thickness of 2.00 ± 0.01 mm) were cut from rods with IsoMet 4000 linear precision saw from Buehler using a diamond cutting disc, polished until mirror grade with diamond polishing discs using Phoenix 4000 polisher machine from Buehler manufacturer. Then, the samples were cleaned in an ultrasonic bath, first with distilled water (3 times, 5 min/time), then with ethanol absolute (3 times, 5 min/time). The samples were stored in a desiccator until use.

Ethylene glycol dimethacrylate (EGDMA, 98%) was purchased from Sigma-Aldrich and used as received. The monomer methyl-DOPA methacrylamide (DOMAm), methyl 3-(3,4-dihydroxyphenyl)-2-(2-methylprop-2-enamido)propa-noate), was kindly provided by Symbiose Biomaterials, Belgium.

Human osteoblast-like MG-63 cells were obtained from American Type Culture Collection (ATCC, USA) for the cell viability study, and Dulbecco's phosphate buffered saline (DPBS) was obtained from Gibco (NY, USA). Milli-Q water was used for the sample's stability coating determination.

6.2.2 Zirconia surface cleaning and activation by atmospheric plasma

Before coating, the disc samples were exposed to Ar/O2 (5% v/v O2) plasma mixture (1.6 W·cm-2, 20 SLM) for 10 consecutive repeats of 48 s/each repetition, to clean and activate the exposed surface in the same plasma deposition setup described in Section 6.2.3 and illustrated in Figure 6-1.

To assess the effect of the plasma cleaning on the surface of the discs, the standard protocol (SP) was modified by doubling the time (DT) of exposure or by doubling the power (DP) of the plasma treatment.
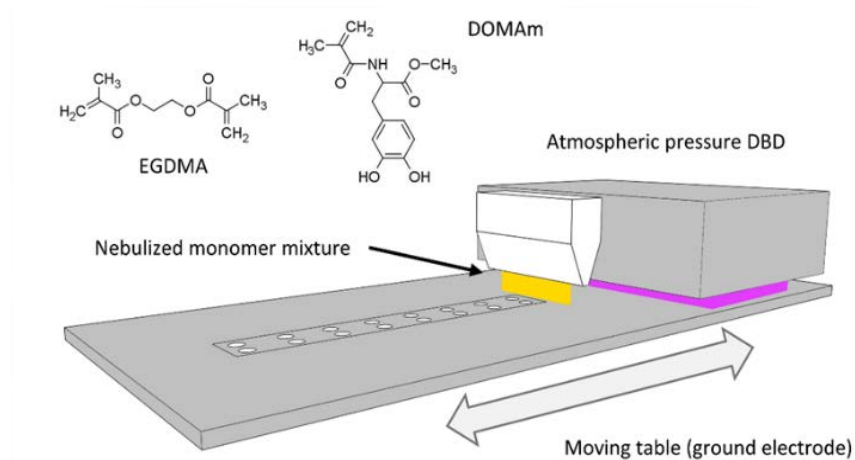
Figure 6-1: . Illustration of dielectric barrier discharge (DBD) deposition setup used to coat the zirconia discs by the Liquid-Assisted Atmospheric Pressure Plasma-induced Polymerization (LA-APPiP) of EGDMA and DOMAm mixtures. A disc holder was inserted in the moving table to keep a constant gap in-between the high voltage electrodes and the table surface.

6.2.3   Plasma deposition of Poly(EGDMA-co-DOMAm) by LA-APPiP

The LA-APPiP of mixtures of EGDMA and DOMAm was reported elsewhere [22]. The experimental setup is schematically shown in Figure 6-1. The coating deposition proceeded by spraying a very thin liquid layer over the surface of the discs using a stream of very fine droplets of the liquid mixture (0.007 mmol·mL-1, DOMAm) in nitrogen (4 SLM, 99.999%) produced using a venturi-based nebulization system (VITO) connected to a 3D printed lineal nozzle. The thin liquid layer was then plasma-induced polymerized by two-subsequent brief expositions, only for a few seconds, to an atmospheric-pressure direct dielectric discharge (DBD) plasma, generated by 10 kHz sinusoidal electrical excitation (SOFTAL "corona generator 7010R") providing 1.6 W·cm^{-2} and using argon (20 SLM, 99.999%) as plasma gas. The moving table, where the ceramic disc samples (up to 24 units) and a piece of the silicon wafer (as control) were placed, acted as the ground electrode and allowed to repeat the 8 s deposition process until a coating thickness of approximately 250 nm on the silicon control by

spectroscopic ellipsometry (VASE-32, J. A. Woollam Co. U.S.) was attained after 150 repeats. The new nanometric film was named as pPoly(EGDMA-co-DOMAm), where "p" means plasma process.

6.2.4 Zirconia surface and pPoly(EGDMA-co-DOMAm) characterization

Several surface characterization techniques were implemented to study the proposed hypothesis. The chemical structure of the plasma polymerized nanocoating (pPoly(EGDMA-co-DOMAm)) was evaluated by X-ray photoelectron spectroscopy (XPS) and Raman techniques. The XPS equipment used was a Kratos Axis-Ultra DLD instrument using an Al Kα source (1486.6 eV) with a pass energy of 20 eV and an energy resolution of 0.5 eV. A flooding gun was used to reduce the charging effect on the surface of the sample. Photoelectron emission take-off angle was established at 0° concerning the surface normal. The C 1s peak with a binding energy of 285 eV was used as the internal reference. The atomic percentage of each element was determined by dividing the peak area of the most intense XPS signal by the corresponding sensitivity factor and by expressing it as a fraction of the sum of all normalized peak areas. High-resolution XPS spectra were acquired by Gaussian/Lorentzian curve fitting after S-shape background subtraction for the following elements: C 1s, O 1s, N 1s, and Zr 3d. Special attention was paid to the analysis of the plasma cleaned sample by transferring it to the XPS equipment immediately after surface treatment.

Raman spectra were acquired in a back-scattering geometry using a Renishaw dispersive Raman microscope spectrometer (model InVia Reflex, GmbH, Germany) and a Renishaw WiRE software. The spectra were acquired with an excitation wavelength of 532 nm line of an Nd:YAG laser. The exposure time was 5 s for each accumulation (×20) at a power of 24 mW. An X50 long working distance objective was used to focus the laser beam on the sample

surface. All Raman spectra were collected in a spectral range from 600 to 4000 cm^{-1} with the same measurement parameters.

Water contact angle (WCA) measurements were taken in a drop shape analyzer (Kruss DSA100). Static WCA values were determined using the sessile water drop method at room temperature and constant relative humidity. Droplet images were recorded 10 seconds after drop deposition. The contact angle value was extracted from the 2 µL droplet shape and determined using a numerical fit based on the Laplace-Young model in the Advance software (Kruss). Due to the reduced size of the disc surface (approximately 50 mm^2), only one droplet was deposited on each sample. The values reported for the discs after the ST plasma treatment and coated with the polymer coating are the average of 3 different disc samples. The topography of the surface was analyzed using atomic force microscopy (AFM), employing a Molecular Imaging PicoSPM with NanoScope IV controller under ambient conditions. The tapping mode was operated at constant deflection and the scan speed was 1 Hz for all measurements. Various places on the sample were analyzed using 50 × 50 µm^2 windows, which correspond to the pictures presented in this work. The Profilmonline software was used to analyze and calculate root-mean-square roughness (Rq) and roughness average (Ra).

Scanning electron microscopy (SEM) was employed for pPoly(EGDMA-co-DOMAm topography analysis. The equipment used is a Focused Ion Beam Zeiss Neon 40 instrument, commercialized by Carl Zeiss (Germany), coupled to a secondary electron beam detector (SE). In order to avoid electron discharge, samples were carbon-coated using Mitek K950 Sputter Coater before analysis. The accelerating voltage for obtaining morphology micrographs was 2 kV.

The coating stability was tested by immersing Y-TZP/pPoly(EGDMA-co-DOMAm) discs in a buffer solution (0.01M PBS, pH 7.4)) for 7 days. The experiment was performed at room temperature and the discs were cleaned

with Milli-Q water and dried in a vacuum before weighing. The weight of the samples was determined before and after 24 h of solution exposure until 7 days, by using a Sartorius CPA26P Microbalance (5 g × 2 µg / 5-21 g × 10 µg). Three replicates were tested. No weight variation was observed. According to the conditions described previously, Raman spectroscopy was used to certify the nanocoating composition after immersion tests.

6.2.5   In vitro biocompatibility assays

The MG-63 cells were cultured in Dulbecco's modified Eagle's medium (DMEM with 4500 mg/L of glucose, 110 mg/L of sodium pyruvate, and 2 mM of L-glutamine) supplemented with 10 % fetal bovine serum (FBS), 50 U/cm^3 penicillin, 50 mg/mL streptomycin and L-glutamine 2 mM at 37 ºC in a 10 % humidified atmosphere of 5% CO_2 and 95% air. Culture media were changed every two days. For sub-culture, cell monolayers were rinsed with PBS and detached by incubating them with 0.25 % trypsin/EDTA for 2-5 min at 37 ºC. The incubation was stopped by re-suspending the vials in 5 mL of fresh medium. The cell concentration was determined by counting them with a Neubauer camera and using 4 % trypan blue as dye vital.

The zirconia discs with pPoly(EGDMA-co-DOMAm) copolymer were placed in tissue culture plates (TCPs) of 24-wells and fixed to the bottom of the plate, with a small drop of silicone (Silbione® Med Adh 4300 RTV, Bluestar Silicones France SAS, Lyon, France). Then, the system was sterilized by exposure to UV light for 15 min. The MG-63 cells were seeded in each TCP well by using the following criteria: (i) for cell adhesion analysis, 100 µL of a suspension containing 2×10^4 cells/well were added to each well, and (ii) for cell proliferation analysis 5×10^4 cells/well were used. After seeding the cells, the plates were incubated for 60 minutes to allow the cell attachment to the material surface. Afterward, 1 mL of culture medium was then added to each well. Quantification of viable cells was

performed after 24 h and 7 days to evaluate the cellular adhesion and proliferation, respectively. The control was performed by cell culture on the TCP well, without pPoly(EGDMA-co-DOMAm) decorated discs.

The percentage of cells that adhered and proliferated was determined through the MTT (3-(4,5-dimethylthiazol-2-yl)-2,5-diphenyltetrazolium bromide) assay [41]. After 24 h or 7 days, 50 µL of MTT (3 mg/mL) was added to each well in the plates and incubated for 4 h. After that, samples were washed twice with PBS and the specimens were deposited on a new plate. Next, 1 mL of dimethyl sulfoxide (DMSO) was added and the absorbance was measured at 570 nm in a microplate reader (Biochrom EZ-Read 400) after 15 min of gentle stirring. Three replicas were evaluated and the corresponding values were averaged.

To obtain images of the morphology of the cells after the adhesion and proliferation assays, samples were fixed overnight with 2.5 % formaldehyde in PBS at 4 °C and then washed five times with PBS. Samples were stained for fluorescence microscopy. Specifically, actin was labeled with green-fluorescent Alexa Fluor Atto-488 phalloidin dye, and the nucleus was labeled with DAPI (4',6-diamidino-2-phenylindole). Then, the samples were observed in a confocal laser scanning microscope (LSM 900 Zeiss) and photographed with a camera controlled by ZEN 2.6 software (blue edition) (Carl-Zeiss Microscopy GmbH, Jena, Germany).

6.3   Results and discussion

6.3.1   Atmospheric-pressure plasma deposition of poly(EGDMA-co-DOMAm) in zirconia substrates activated by oxygen plasma

Previous works demonstrated the applicability of the LA-APPiP deposition method to obtain biocomposites for biomedical applications [22], [23]. In such studies, the surfaces explored were mainly stainless steel, titanium, and silicon

wafer-substrates. For example, the method allowed the fast deposition of pine hole-free polymeric coatings functionalized with catechol and quinone groups that were used for the bioactivation of the coating by controlled covalent immobilization of enzymes and biosurfactant proteins. In the present study, for the first time, polydopamine/acrylate copolymer derivative has been used to cover a ceramic substrate used in dentistry applications to improve the biocompatibility of ceramic. The process involved a preliminary step of plasma cleaning of the zirconia material to create active sites and modify the surface wettability and, subsequently, chemical polymerization of the biocompatible copolymer and the growth of osteoblastic cells for the evaluation of its *in vitro* biocompatibility response.

The disc's topmost surface chemical composition was analyzed by XPS after each step of the deposition process. The presence of the coating on the zirconia disc after plasma deposition is clearly evidenced by the increase in the signals generated from the organic components (C 1s, O 1s, and N 1s, Table 6-1). Despite the thickness determined by ellipsometry (250 ± 17 nm), which was much higher than the deep of electron beam penetration (< 10 nm) of the XPS equipment, the peaks attributed to the substrate (Zr 3d) were still detected in the coated sample, even though with much lower intensities than those of pristine and cleaned samples. The change in intensity could be related to the topography of the nanocoating, with peak-to-valley distances larger than the average thickness measured by ellipsometry, rather than to the presence of pine-holes in the plasma polymer layer.

Table 6-1: XPS atomic composition of the zirconia disc sample coated with pPoly(EGDMA-co-DOMAm) by atmospheric plasma deposition.

Element	Atomic concentration (%)
C 1s	63.0
O 1s	30.7
N 1s	1.4
Zr 3d	4.3
Y 3d	0.6

XPS core level data was acquired for Zr 3d, O 1s, C 1s, and N 1s (Figure 6-2). The deconvolution of Zr $3d_{3/2}$, Zr $3d_{5/2}$, and O 1s XPS peaks did not show significant changes in the ZrO_2 environment in the pristine zirconia and after oxygen plasma cleaning (Figure 6-2a). On the contrary, a clear reduction of the contribution associated with the Zr–O bond in O 1s deconvoluted peaks (528.6-529.4 eV) was obtained (Figure 6-2b). Moreover, the standard protocol for surface cleaning and activation of the zirconia disc successfully induced a reduction of the atmospheric organic contaminants present on the surface of the pristine discs (Figure 6-2 c-d). As expected, the organic character of the plasma polymer deposited layer was evidenced by a significant shift of C 1s and O 1s peaks intensities to higher binding energies and the occurrence of new components, such as C=O/N–C=O (287.7 eV), C–O/C–OH (286.5 eV) and C–COO/C–N (285.6 eV) in C 1s high-resolution spectrum of pPoly(EGDMA-co-DOMAm). Therefore, the contributions of the ester, amide, and catechol groups were successfully detected. The C/O ratio of 2.1 was slightly lower than the theoretical value of 2.5. In addition to the contribution of the oxygen from the ceramic, the formation of oxygen-containing polar groups is commonly attributed to polymers exposed to plasmas.

Otherwise, the detection of nitrogen from DOMAm's amide groups (400.3 eV, Figure 6-2d) was more efficient after cleaning the pristine zirconia surface with oxygen plasma.

The stability of the coating was studied by immersing zirconia discs in PBS buffer and further evaluation of the weight loss and the chemical structure composition by gravimetry and Raman analysis, respectively. Although the high hydrophilicity of pPoly(EGDMA-co-DOMAm) coatings (Section 6.3.2) would induce the polymer detachment by water absorption, the film adhered well to the zirconia surface and no delamination was observed, even after 7 days of immersion in the solution. Three replicates were analyzed by gravimetry and the film weight remained constant, confirming the efficiency of the plasma deposition.
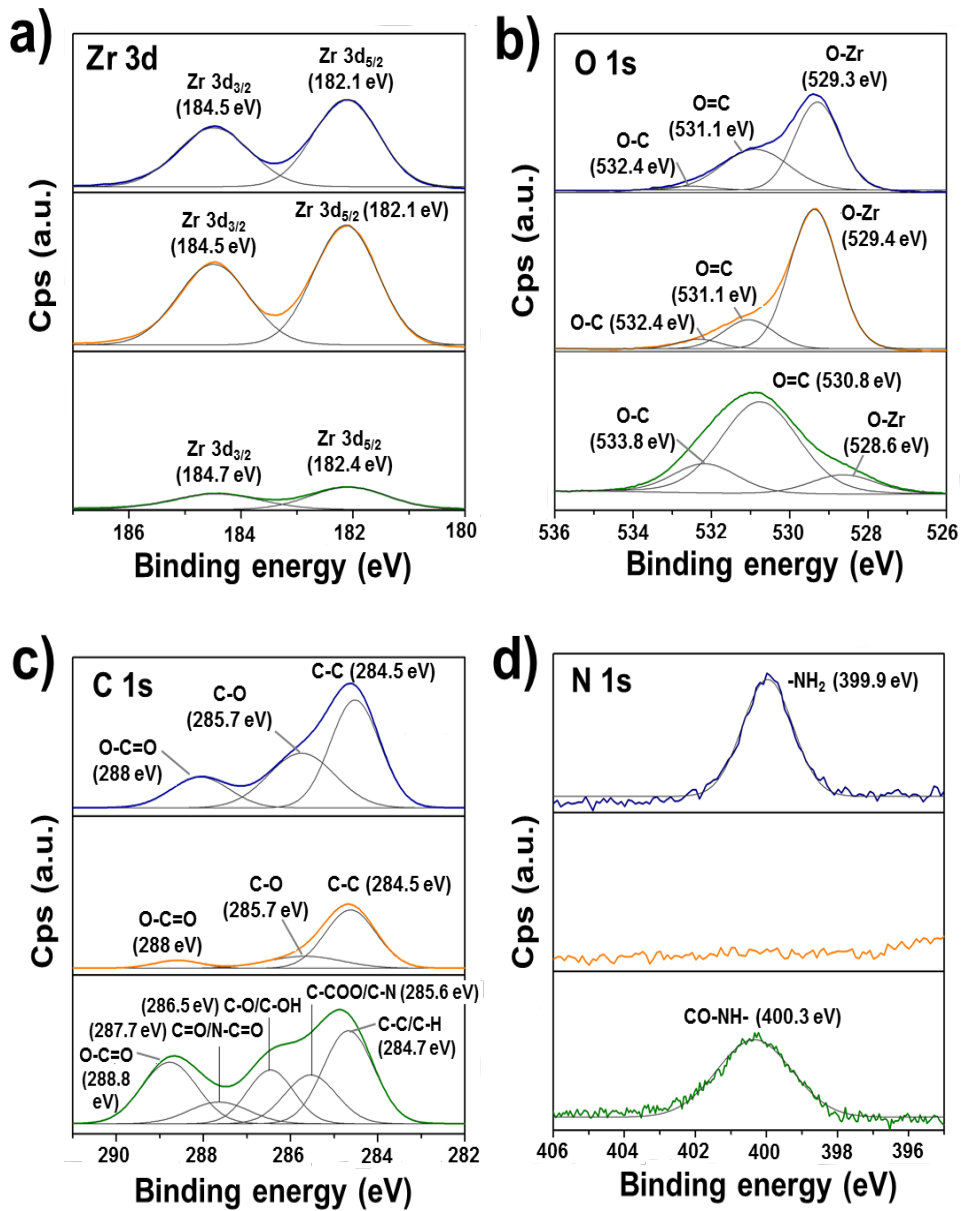
Figure 6-2: XPS high-resolution spectra of the zirconia surface before and after oxygen plasma treatment and coated with pPoly(EGDMA-co-DOMAm): a) Zr 3d, b) O 1s, c) C 1s, and d) N 1s. From bottom to top for all the tested elments: pristine sample, plasma-cleaned sample, and coated sample.

Raman spectra (Figure 6-3) taken from two different zones after one week (Figure 6-3) was comparable with that of samples freshly prepared. As can be seen, the main absorption bands appear in the range of 4000-1200 cm^{-1} (Raman region of 100-1200 cm^{-1} is not shown due to the substrate interference). The first broad and very strong absorption band at 2800-2950 cm^{-1} corresponds to C–H stretching (–CH$_2$– and CH$_3$ groups) and is confirmed by a fingerprint band at 1449 cm^{-1} (scissoring and asymmetric bending), which intensity is usually proportional to the number of methylene in the copolymer chain. Polar groups were also identified, showing low-intensity bands at 1552 cm^{-1} (–CH from aromatic rings) and at 1638 cm^{-1} and 1734 cm^{-1} (C=O). The two late peaks belong to amide II (-CONH-, DOMAm), which is much less intense than amide I, and to the ester group (–COO–, EGDMA), respectively. The absorption bands from catechol groups of PDA usually appear at ~1350 cm^{-1} and ~1580 cm^{-1} (stretching and deformation, respectively) [30]. Both absorption bands exhibit much lower intensity than the EGDMA groups (Figure 6-3). Furthermore, the weak and broad band observed at 3540 cm^{-1}, which corresponds to –OH stretching from catechol rings, confirms the presence of the DOMAm component. Our results are consistent with previous work, in which authors demonstrated the covalent linkage of hydroxyl groups from PDA with ZrO$_2$ molecules [37]. Thus, a lower intensity of catechol and hydroxyl groups from DOMAm in our system supposedly indicates a successful covalent bond of pPoly(EGDMA-co-DOMAm) with the substrate through aromatic and hydroxyl contributions.
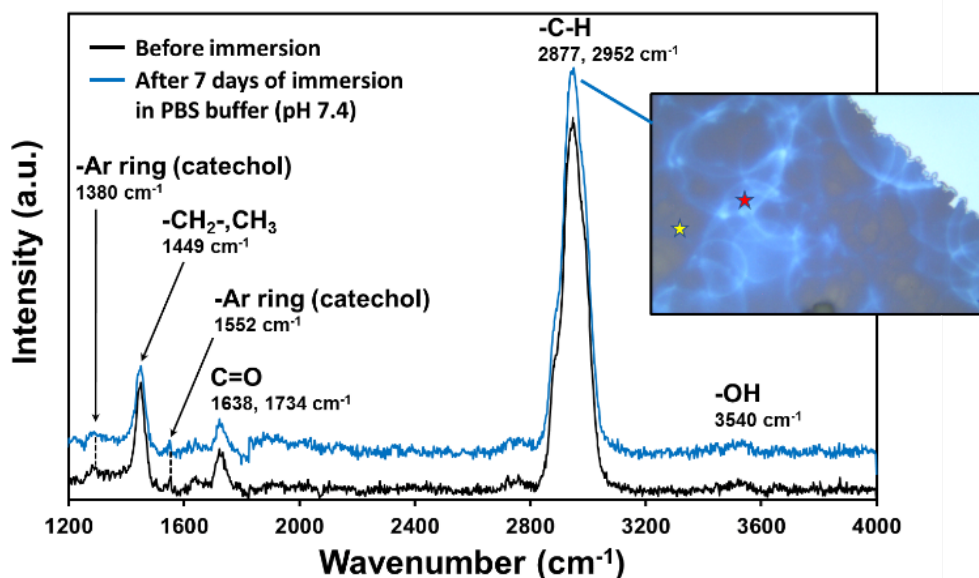
Figure 6-3: Raman spectra of zirconia disc coated with pPoly(EGDMA-co-DOMAm) nanometric film before and after immersion of samples in PBS buffer solution for 7 days. The inset represents the optical microscopy of the coating showing two zones analyzed after 1 week. The spectra of both points, indicated by yellow and red stars, are similar and only one of them has been plotted.

6.3.2 Wettability and AFM investigations of zirconia/pPoly(EGDMA-co-DOMAm) surface

The osseointegration of an implant is highly dependent on the following surface context: (i) wettability, (ii) roughness, and (iii) substrate chemical nature. First, the wettability of the samples was evaluated by comparing different surface treatments (Figure 6-4). The pristine Y-TZP disc has hydrophilic interaction with water molecules, having a static WCA of 72.7º ± 2.0º (Figure 6-4 a). After oxygen plasma treatment (5 %v/v O_2 in Ar) using a standard protocol (480 s at 1.6 W·cm^{-2}), the hydrophilicity increased by 70 % (21.3º ± 1.5º Figure 6-4 b1) with respect to the pristine sample, revealing the positive effect of the appearance of Zr–O species with charges (ZrO-, ZrOH-), and radical (Zr–O˙)

groups induced by plasma.

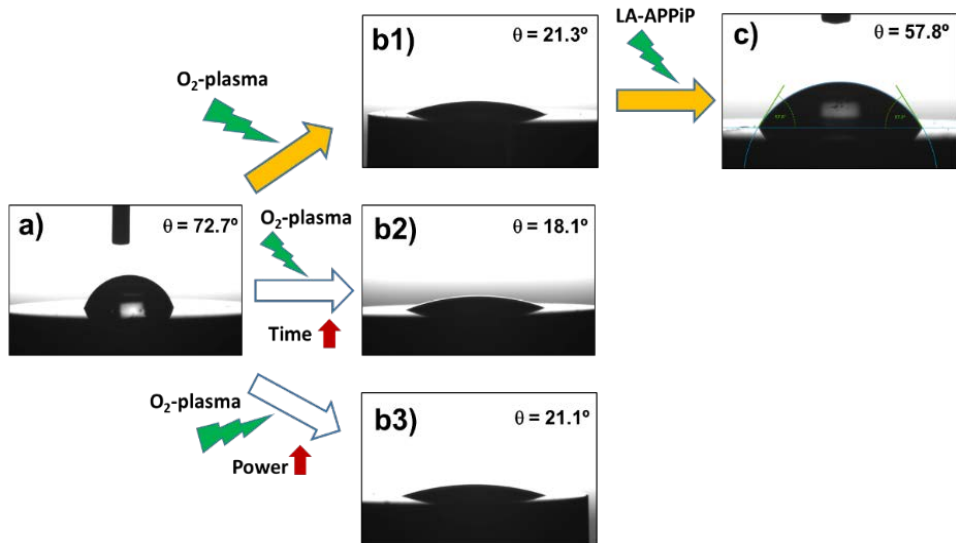*Figure 6-4: Variability of water contact angle, after oxygen plasma treatment and polymer deposition: (a) pristine zirconia disc; (b) zirconia disc after cleaning with oxygen plasma: b1) 480 s + 1.6 W·cm⁻² plasma power (Standard protocol, SP); b2) 960 s + 1.6 W·cm⁻² plasma power (Double time, DT); b3) 480 s + 3.2 W·cm⁻² plasma power (Double power, DP); and c) zirconia/pPoly(EGDMA-co-DOMAm) disc. Filled arrows indicate the final route followed to prepare samples for biocompatibility assays.*

Kalyoncuoglu et al. [42] also demonstrated the superhydrophilic behavior of polished zirconia substrates after O_2-plasma, Ar-plasma, and CF_4-plasma attack with a reduction of WCA of about 87 %. On the contrary, an increase of O_2-plasma time cleaning, by applying two sets of plasma discharges and maintaining the plasma powder constant (DT protocol, 960 s at 1.6 W·cm⁻¹ (Figure 6-4 b2), or an increase of power force maintaining the time constant (DP protocol; 480 s at 3.2 W·cm⁻¹) (Figure 6-4 b3), do not affect the ceramic surface wettability. Thus, an almost unappreciated lowering of WCA values was observed (18.1º ± 1.9º and 21.1 ± 1.5º, respectively, for DT and DP plasma cleaning). Once the copolymer is generated by the LA-APPiP method, the WCA enhances (57.8º ± 2.2º, Figure 6-4 c), even though, as expected, it is still hydrophilic due to the polar chemical nature of the dopamine and acrylate monomers structure (Figure 6-1) [22], [23].

Having checked that the new polymeric coating is stable in biological solution

and is well-adhered, AFM studies were performed to evaluate the roughness and topography properties of Y-TZP/pPoly(EGDMA-co-DOMAm) biocomposite. Figure 6-5 shows the evolution of the substrate interface after each cleaning step and after the polymerization process carried out by the LA-APPiP method.

Compared to laser-texturing ablation methods [14], [43], [44], which also help to enhance the wettability of the zirconia surface for cell adhesion, the O_2-plasma surface treatment can be considered a "gentle" treatment. The zirconia surface can be considered "ultra-smooth" even after the application of double power discharge and increased plasma time, with a roughness average (Ra) from 1.6 nm to 7.3 nm (Table 6-2: root-mean-square roughness (Rq) and roughness average (Ra) values as obtained by AFM after different oxygen-plasma pre-treatment conditions and after plasma polymerization) and comparable to the pristine surface (Figure 6-5). Thus, the plasma cleaning does not affect the microstructure features of the zirconia surface. After the LA-APPiP of EGDMA and DOMAm, the Ra increased by a factor of 3.9 with respect to the plasma cleaned or polished zirconia (79.9 $\pm$ 13.7 nm). The nanometric polymer layer is homogeneously distributed in an area of 50×50 μm^2 of the substrate, as can be seen in Figure 6-5c.

Table 6-2: Root-mean-square roughness (Rq) and roughness average (Ra) values as obtained by AFM after different oxygen-plasma pre-treatment conditions and after plasma polymerization.

Plasma treatment	Rq (nm)	Ra (nm)
Pristine sample (polished)	2.63 $\pm$ 0.14	2.08 $\pm$ 0.08
Standard protocol (SP)	2.21 $\pm$ 0.25	1.62 $\pm$ 0.15
Double time protocol (DT)	9.13 $\pm$ 1.32	7.28 $\pm$ 1.17
Double power protocol (DP)	2.72 $\pm$ 0.17	2.09 $\pm$ 0.11
pPoly(EGDMA-co-DOMAm) (plasma polymerized coating)	94.61 $\pm$ 13.93	79.85 $\pm$ 13.71

The formation of a wrinkle-like topography might be attributed to the dynamic deposition (layer-after-layer) of well-adherent crosslinked polymeric layers from very thin liquid layers [45]. The difference between the first layers and the consecutive ones generates surface stress due to a mismatch of their elastic properties, being the initial layers less elastic due to their adhesion to the much more rigid zirconia surface. The results altogether support the previous statement of a well-adherent biocompatible pPoly(EGDMA-co-DOMAm) nanometric film.

Therefore, the best route used for the final zirconia/pPoly(EGDMA-co-DOMAm) discs preparation was that expressed as a), b1), and c) in Figure 6-5. The O_2-plasma cleaning has been demonstrated to be a crucial preliminary step for the obtaining of well-adhered covalently bonded pPoly(EGDMA-co-DOMAm) copolymer film on zirconia surfaces.
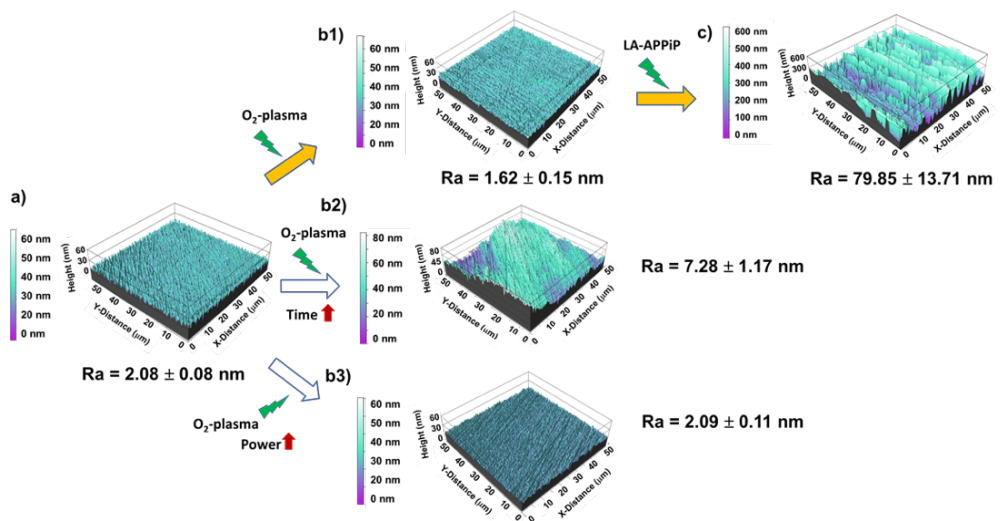
Figure 6-5: AFM topography images (50 µm x 50 µm) and roughness averages (Ra) of zirconia discs with different pretreatments and after polymer deposition: (a) pristine zirconia disc; (b) zirconia disc after cleaning with oxygen plasma: b1) 480 s + 1.6 W·cm⁻² plasma power (Standard protocol, SP); b2) 960 s + 1.6 W·cm⁻² plasma power (Double time, DT); b3) 480 s + 3.2 W·cm⁻² plasma power (Double power, DP); and c) zirconia/pPoly(EGDMA-co-DOMAm) disc. Filled arrows indicate the final route followed to prepare samples for biocompatibility assays.

6.3.3   In vitro biocompatibility

In this study, two different materials, a zirconia substrate and a nanocoating of a biocompatible copolymer, with different surface properties (as shown before), have been investigated for their biocompatibility with MG-63 human cells. The greater value of roughness leads to better wettability of the surface and better bonding properties of the material with other systems.

The response of PDA self-polymerized on plastics, titanium, and ceramic substrates (including zirconia) with enhanced osteoblastic adhesion towards cells has been extensively investigated using *in vitro* assays [8], [28], [29], [36]. However, deep research on the effect of PDA and derivatives synthesized by atmospheric plasma was never approached, to the best of our knowledge. As expected, the adhesion and proliferation were different. Figure 6-6 demonstrates that the pPoly(EGDMA-co-DOMAm) copolymer surfaces support adhesion and proliferation of osteogenic MG-63 cells, having better adherent cells of fibroblast type than the previously investigated PICN samples. The macroscopic image of the pPoly(EGDMA-co-DOMAm) copolymer discs seeded with MG-63 cells onto the material surface (Figure 6-6 a) shows the reaction of viable cells with the MTT reagent. The reaction corresponds to the conversion of the MTT reagent into a dark blue formazan salt. Dehydrogenase enzymes mediate such reactions from mitochondria and lysosomes in viable cells. In this way, the stain of the discs is similar to the stain observed on the culture plates, which correspond to the control. These salts can then be dissolved in some organic solvents, e.g., DMSO, and allow quantification of viable cells (as described in the experimental section). Also, the viability of the cells on the surface of the material and in the total well of the culture plate was quantitatively determined. The latter measurement indicates the possible cytotoxicity effects induced by the release of the material or its products (i.e. monomer, dissolvent, etc) to the culture medium. Figure 6-6 b shows that the

cell adhesion evaluated after 24 h of culture on the surface of the pPoly(EGDMA-co-DOMAm) copolymer was similar to the control, and it is also shown that the material does not have any cytotoxic effect when adhesion is evaluated in the total well (cells attached to the material plus cells attached to the plate). Cell proliferation (Figure 6-6 c), which is evaluated after 7 days of culture, reflects the capacity of cell division to increase the number of cells and material colonization. Results show that the pPoly(EGDMA-co-DOMAm) copolymer allows cell growth and colonization on its surface. Moreover, it was also demonstrated that in prolonged time (7 days), the samples lack any cytotoxic effect.
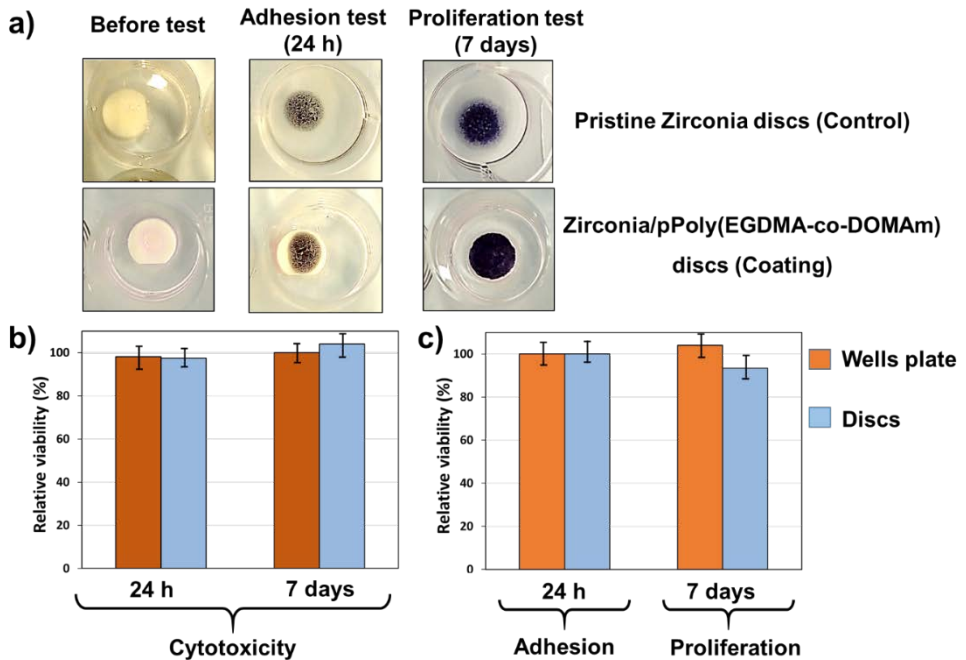
Figure 6-6: Viability of osteogenic MG-63 cells with zirconia/pPoly(EGDMA-co-DOMAm) decorated discs: (a) optical microscopy images of TCP wells plate with pristine and zirconia/pPoly(EGDMA-co-DOMAm)discs, before and after MG-63 cells incubation; (b) cytotoxicity evaluation after 24 h and 7 days; and (c) adhesion of MG-63 cells after 24h and cells proliferation after 7 days, respectively.

Fluorescence microscopy images of MG-63 cells are shown in Figure 6-7. The cells in extension on the surface of the material are clearly observed during adhesion and cells in higher density during growth. High magnification micrographs show that in both cases the cells extend their cytoplasm-shaped

filopodia to adhere to the surface and promote cell migration in the cell adhesion and establish contacts between cells. These results prove that the catechol/acrylate copolymer has biocompatible characteristics in vitro and allows the adhesion and growth of osteogenic MG-63 cells.
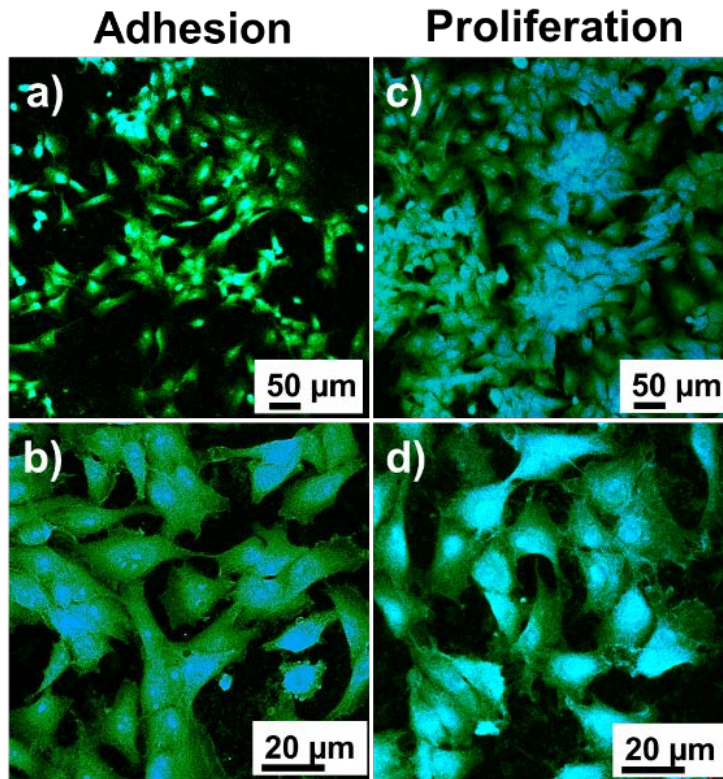
Figure 6-7: Fluorescence optical images of osteogenic MG-63 cells adhered to zirconia/pPoly(EGDMA-co-DOMAm)discs: (a-b) Low and high magnification images of the adhered cells, after 24h of incubation, respectively; and (c-d) Low and high magnification images of cells proliferation, after 7 days of incubation, respectively. MG-63 cells were stained with phalloidin dye, in which the nucleus is represented as blue color, and the cytoplasmic actin filaments are marked as green color

6.4 Conclusions

For the first time, a Poly(EGDMA-co-DOMAm) copolymer coating has been successfully covalently bonded to a ceramic substrate. The employment of atmospheric plasma to activate the zirconia surface and the liquid-assisted polymerization of polydopamine and ethylene glycol dimethacrylate monomers

by plasma (called LA-APPiP) resulted in a fast and friendly way to obtain a very smooth and stable nanometric film. The new ceramic coating has enhanced human cell proliferation and adhesion, after 24 h and 7 days of incubation, respectively; when compared to the pristine zirconia samples.

Such results open new insights for continuing the investigations of applying the LA-APPiP method to replace less friendly approaches, like layer-by-layer deposition, sol-gel technologies, or adsorption methods, for the obtaining of thin films in solid substrates; which usually expend a lot of solvents and purification steps. LA-APPiP can be extended to other materials surfaces, such as polymers, metals, and other ceramic compounds, and can be easily scalable for industrial applications. However, it could not be used for the polymerization of 3D-printed zirconia substrates, like PICN production, due to the difficulty to achieve plasma energy among the zirconia filaments.

6.5   References

[1]   M. F. Kunrath, "Customized dental implants: Manufacturing processes, topography, osseointegration and future perspectives of 3D fabricated implants," *Bioprinting*, vol. 20, no. August, p. e00107, 2020, doi: 10.1016/j.bprint.2020.e00107.

[2]   J. Schweiger, D. Bomze, and M. Schwentenwein, "3D Printing of Zirconia– What is the Future?," *Current Oral Health Reports*, vol. 6, no. 4, pp. 339– 343, 2019, doi: 10.1007/s40496-019-00243-4.

[3]   L. C. Hwa, S. Rajoo, A. M. Noor, N. Ahmad, and M. B. Uday, "Recent advances in 3D printing of porous ceramics: A review," *Current Opinion in Solid State and Materials Science*, vol. 21, no. 6, pp. 323–347, 2017, doi: 10.1016/j.cossms.2017.08.002.

[4]   G. B. Brown, G. Fräns Currier, O. Kadioglu, and J. P. Kierlb, "Accuracy of 3-dimensional printed dental models reconstructed from digital intraoral impressions," *American Journal of Orthodontics and Dentofacial Orthopedics*, vol. 154, pp. 733–739, 2018, doi: 10.1016/j.ajodo.2018.06.009.

[5]   M. Juneja, N. Thakur, D. Kumar, A. Gupta, B. Bajwa, and P. Jindal, "Accuracy in dental surgical guide fabrication using different 3-D printing techniques," *Additive Manufacturing*, vol. 22, no. May, pp. 243–255, 2018, doi: 10.1016/j.addma.2018.05.012.

[6]   A. Jonhson, P. Sinthuprasirt, H. Fathi, and S. Pollington, "Current Glass-Ceramic Systems Used in Dentistry," in *Current Trends on Glass and Ceramic Materials*, S. H. Nandyala and J. Dos Santos, Eds. Sharjak: Bentham Science Publishers, 2013, pp. 49–72.

[7]   S. Roedel, J. Mesquita-Guimarães, J. C. M. Souza, F. S. Silva, M. C. Fredel, and B. Henriques, "Production and characterization of zirconia structures with a porous surface," *Materials Science and Engineering C*, vol. 101, no. February, pp. 264–273, 2019, doi: 10.1016/j.msec.2019.03.087.

[8]   F. H. Schünemann *et al.*, "Zirconia surface modifications for implant dentistry," *Materials Science and Engineering C*, vol. 98, no. July 2018, pp. 1294–1305, 2019, doi: 10.1016/j.msec.2019.01.062.

[9]   M. S. Zafar, M. A. Fareed, S. Riaz, M. Latif, S. R. Habib, and Z. Khurshid, "Customized therapeutic surface coatings for dental implants," *Coatings*, vol. 10, no. 6, pp. 1–37, 2020, doi: 10.3390/coatings10060568.

[10]   G. Soon, B. Pingguan-Murphy, K. W. Lai, and S. A. Akbar, "Review of zirconia-based bioceramic: Surface modification and cellular response," *Ceramics International*, vol. 42, no. 11, pp. 12543–12555, 2016, doi: 10.1016/j.ceramint.2016.05.077.

[11]   S. L. Aktuğ, S. Durdu, E. Yalçın, K. Çavuşoğlu, and M. Usta, "Bioactivity and biocompatibility of hydroxyapatite-based bioceramic coatings on zirconium by plasma electrolytic oxidation," *Materials Science and Engineering C*, vol. 71, pp. 1020–1027, 2017, doi: 10.1016/j.msec.2016.11.012.

[12]   M. Stefanic, K. Krnel, I. Pribosic, and T. Kosmac, "Rapid biomimetic deposition of octacalcium phosphate coatings on zirconia ceramics (Y-TZP) for dental implant applications," *Applied Surface Science*, vol. 258, no. 10, pp. 4649–4656, Mar. 2012, doi: 10.1016/j.apsusc.2012.01.048.

[13]   L. C. Trincă *et al.*, "Osseointegration evaluation of ZrTi alloys with hydroxyapatite-zirconia-silver layer in pig's tibiae," *Applied Surface Science*, vol. 487, pp. 127–137, Sep. 2019, doi: 10.1016/j.apsusc.2019.05.003.

[14]   A. Carvalho, L. Cangueiro, V. Oliveira, R. Vilar, M. H. Fernandes, and F. J. Monteiro, "Femtosecond laser microstructured Alumina toughened Zirconia: A new strategy to improve osteogenic differentiation of hMSCs," *Applied Surface Science*, vol. 435, pp. 1237–1245, 2018, doi: 10.1016/j.apsusc.2017.11.206.

[15]   Z. Huang, Z. Wang, C. Li, K. Yin, D. Hao, and J. Lan, "Application of implants: Study in implants plasma-spray ed zirconia coating in dental," *Journal of Oral Implantology*, vol. 44, no. 2, pp. 102–108, 2018, doi: 10.1563/aaid-joi-D-17-00020.

[16]   B. S. Yilbas, "Laser treatment of zirconia surface for improved surface hydrophobicity," *Journal of Alloys and Compounds*, vol. 625, pp. 208–215, 2015, doi: 10.1016/j.jallcom.2014.11.069.

[17]   C. G. Moura *et al.*, "Effect of laser surface texturing on primary stability and surface properties of zirconia implants," *Ceramics International*, vol. 43, no. 17, pp. 15227–15236, 2017, doi: 10.1016/j.ceramint.2017.08.058.

[18]   Y. C. Liu, J. P. Hsieh, Y. C. Chen, L. L. Kang, C. S. Hwang, and S. F. Chuang, "Promoting porcelain–zirconia bonding using different atmospheric pressure gas plasmas," *Dental Materials*, vol. 34, no. 8, pp. 1188–1198, 2018, doi: 10.1016/j.dental.2018.05.004.

[19]   C. Caravaca *et al.*, "Direct silanization of zirconia for increased biointegration," *Acta Biomaterialia*, vol. 46, no. 2016, pp. 323–335, 2016, doi: 10.1016/j.actbio.2016.09.034.

[20]   B. Chen *et al.*, "Effectiveness of pre-silanization in improving bond performance of universal adhesives or self-adhesive resin cements to silica-based ceramics: Chemical and in vitro evidences," *Dental Materials*, vol. 35, no. 4, pp. 543–553, 2019, doi: 10.1016/j.dental.2019.01.010.

[21]   J. P. Matinlinna, C. Y. K. Lung, and J. K. H. Tsoi, "Silane adhesion mechanism in dental applications and surface treatments: A review," *Dental Materials*, vol. 34, no. 1, pp. 13–28, 2018, doi: 10.1016/j.dental.2017.09.002.

[22]   U. Czuba *et al.*, "Atmospheric Plasma Deposition of Methacrylate Layers Containing Catechol/Quinone Groups: An Alternative to Polydopamine Bioconjugation for Biomedical Applications," *Advanced Healthcare Materials*, vol. 7, no. 11, pp. 1–11, 2018, doi: 10.1002/adhm.201701059.

[23]   U. Czuba *et al.*, "Anti-biofouling activity of Ranaspumin-2 bio-surfactant immobilized on catechol-functional PMMA thin layers prepared by atmospheric plasma deposition," *Colloids and Surfaces B: Biointerfaces*, vol. 178, no. February, pp. 120–128, 2019, doi: 10.1016/j.colsurfb.2019.02.049.

[24]   C. Ma *et al.*, "Atmospheric-pressure plasma assisted engineering of polymer surfaces: From high hydrophobicity to superhydrophilicity," *Applied Surface Science*, vol. 535, no. June 2020, p. 147032, 2021, doi: 10.1016/j.apsusc.2020.147032.

[25]   H. Lee, S. M. Dellatore, W. M. Miller, and P. B. Messersmith, "Mussel-inspired surface chemistry for multifunctional coatings," *Science (1979)*, vol. 318, no. 5849, pp. 426–430, Oct. 2007, doi: 10.1126/science.1147241.

[26]   H. Lee, J. Rho, and P. B. Messersmith, "Facile conjugation of biomolecules onto surfaces via mussel adhesive protein inspired coatings," *Advanced Materials*, vol. 21, no. 4, pp. 431–434, Jan. 2009, doi: 10.1002/adma.200801222.

[27]   J. H. Ryu, P. B. Messersmith, and H. Lee, "Polydopamine Surface Chemistry: A Decade of Discovery," *ACS Applied Materials and Interfaces*, vol. 10, no. 9, pp. 7523–7540, 2018, doi: 10.1021/acsami.7b19865.

[28]   L. Wang *et al.*, "Bi-functional titanium-polydopamine-zinc coatings for infection inhibition and enhanced osseointegration," *RSC Advances*, vol. 9, no. 6, pp. 2892–2905, Jan. 2019, doi: 10.1039/c8ra09112a.

[29]   L. Jia *et al.*, "Polydopamine-assisted surface modification for orthopaedic implants," *Journal of Orthopaedic Translation*, vol. 17, pp. 82–95, Apr. 2019, doi: 10.1016/j.jot.2019.04.001.

[30]   H. Wang, C. Lin, X. Zhang, K. Lin, X. Wang, and S. G. Shen, "Mussel-Inspired Polydopamine Coating: A General Strategy To Enhance Osteogenic Differentiation and Osseointegration for Diverse Implants," *ACS Applied Materials & Interfaces*, vol. 11, no. 7, pp. 7615–7625, Feb. 2019, doi: 10.1021/acsami.8b21558.

[31]   J. S. Al-Sanabani, A. A. Madfa, and F. A. Al-Sanabani, "Application of calcium phosphate materials in dentistry," *International Journal of Biomaterials*, vol. 2013, no. 876132, pp. 1–12, 2013, doi: 10.1155/2013/876132.

[32]   G. Revilla-López, A. M. Rodríguez-Rivero, L. J. Del Valle, J. Puiggalí, P. Turon, and C. Alemán, "Biominerals Formed by DNA and Calcium Oxalate or Hydroxyapatite: A Comparative Study," *Langmuir*, vol. 35, no. 36, pp. 11912–11922, 2019, doi: 10.1021/acs.langmuir.9b01566.

[33]   M. Cadenaro *et al.*, "The role of polymerization in adhesive dentistry," *Dental Materials*, vol. 35, no. 1, pp. e1–e22, 2019, doi: 10.1016/j.dental.2018.11.012.

[34]   L. C. Natale *et al.*, "Development of calcium phosphate/ethylene glycol dimethacrylate particles for dental applications," *Journal of Biomedical Materials Research - Part B Applied Biomaterials*, vol. 107, no. 3, pp. 708–715, 2019, doi: 10.1002/jbm.b.34164.

[35]   A. Szczesio-Wlodarczyk, J. Sokolowski, J. Kleczewska, and K. Bociong, "Ageing of dental composites based on methacrylate resins-A critical review of the causes and method of assessment," *Polymers (Basel)*, vol. 12, no. 4, 2020, doi: 10.3390/POLYM12040882.

[36]   Y. T. Liu, T. M. Lee, and T. S. Lui, "Enhanced osteoblastic cell response on zirconia by bio-inspired surface modification," *Colloids and Surfaces B: Biointerfaces*, vol. 106, pp. 37–45, 2013, doi: 10.1016/j.colsurfb.2013.01.023.

[37]   J. Ou, J. Wang, Y. Qiu, L. Liu, and S. Yang, "Mechanical property and corrosion resistance of zirconia/polydopamine nanocomposite multilayer films fabricated via a novel non-electrostatic layer-by-layer assembly technique," *Surface and Interface Analysis*, vol. 43, no. 4, pp. 803–808, Apr. 2011, doi: 10.1002/sia.3631.

[38]   L. Fleischmann, A. Crismani, F. Falkensammer, H. P. Bantleon, X. Rausch-Fan, and O. Andrukhov, "Behavior of osteoblasts on TI surface with two different coating designed for orthodontic devices," *Journal of Materials Science: Materials in Medicine*, vol. 26, no. 1, pp. 1–9, Nov. 2015, doi: 10.1007/s10856-014-5335-9.

[39]   U. Czuba *et al.*, "Atmospheric Plasma Deposition of Methacrylate Layers Containing Catechol/Quinone Groups: An Alternative to Polydopamine Bioconjugation for Biomedical Applications," *Advanced Healthcare Materials*, vol. 7, no. 11, pp. 1–11, 2018, doi: 10.1002/adhm.201701059.

[40]   J. V. Wandiyanto *et al.*, "The Fate of Osteoblast-Like MG-63 Cells on Pre-Infected Bactericidal Nanostructured Titanium Surfaces," *Materials*, vol. 12, no. 10, p. 1575, May 2019, doi: 10.3390/ma12101575.

[41]   T. Mosmann, "Rapid colorimetric assay for cellular growth and survival: Application to proliferation and cytotoxicity assays," *Journal of Immunological Methods*, vol. 65, no. 1–2, pp. 55–63, Dec. 1983, doi: 10.1016/0022-1759(83)90303-4.

[42]   U. T. Kalyoncuoglu, B. Yilmaz, S. G. Koc, Z. Evis, P. U. Arpaci, and G. Kansu, "Investigation of surface structure and biocompatibility of chitosan-coated zirconia and alumina dental abutments," *Clinical Implant Dentistry and Related Research*, vol. 20, no. 6, pp. 1022–1029, 2018, doi: 10.1111/cid.12665.

[43]   X. Jing, Z. Pu, S. Zheng, F. Wang, and H. Qi, "Nanosecond laser induced microstructure features and effects thereof on the wettability in zirconia," *Ceramics International*, vol. 46, no. 15, pp. 24173–24182, 2020, doi: 10.1016/j.ceramint.2020.06.197.

[44]   A. Daskalova *et al.*, "Effect of surface modification by femtosecond laser on zirconia based ceramics for screening of cell-surface interaction," *Applied Surface Science*, vol. 513, no. January, p. 145914, 2020, doi: 10.1016/j.apsusc.2020.145914.

[45]   C. M. González-Henríquez, F. E. Rodriguez-Umanzor, M. A. Sarabia-Vallejos, C. A. Terraza, E. Martínez-Campos, and J. Rodriguez-Hernandez, "Innovative procedure for precise deposition of wrinkled hydrogel films using direct inkjet printing," *Materials and Design*, vol. 194, p. 108959, 2020, doi: 10.1016/j.matdes.2020.108959.

07

Conclusions
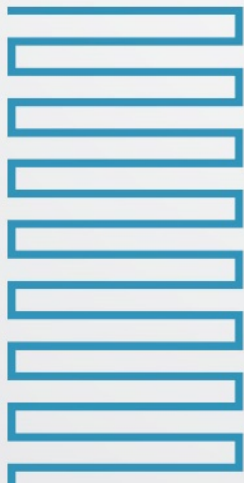
7. Conclusions

The last chapter of this thesis draws general conclusions based on the results presented in previous chapters.

The idea of a combination of polymer-infiltrated ceramic networks (PICN) with direct ink writing additive manufacturing has proven to be successful. Carefully adjusted parameters of designed porosity (50 %) of 3Y-TZP scaffolds and Bis-GMA/TEGDMA copolymer ratio (40:60, respectively) resulted in the development of a manufacturing protocol with great reproducibility. The challenging task of copolymer adhesion to the surface of inert sintered zirconia was overcome by applying γ-MPS organosilane as a coupling agent. The proper adhesion was not only observed by multiple characterization techniques, but also by the density of infiltration, which reached more than 87%.

As one of this thesis's main goals was to optimize the mechanical properties of 3Y-TZP, a study of the behavior of PICN samples under compression force was evaluated. Based on traditional testing, but also observed by the infrared camera, it was concluded that the PICN samples can resist higher deformation in comparison with empty porous scaffolds or 3D-printed scaffolds with zero designed porosity. Moreover, a decrease in overall hardness was observed in PICN samples giving them properties more similar to natural teeth than pure 3Y-TZP. Therefore, the methacrylate copolymer adhesive actuated as a shock absorber, as planned.

In the last part of this thesis, the surface modification of zirconia with a proven cell adhesion promoter like polydopamine was studied. Polydopamine and ethylene glycol dimethacrylate copolymer were for the first time applied to the zirconia surface by the liquid-assisted plasma polymerization, a solvent-free polymer deposition technology to various surfaces. The absence of solvents is

advantageous and avoids subsequent purification steps and was proven to successfully deposit the desirable nanometric film. However, this method is unfeasible for the scope of infiltration of 3D-printed zirconia structures with macropores due to the lack of energy to overpass the ceramic filaments. Then, for 3D-printed scaffolds chemical copolymerization activated by catalysts is recommended.

As the developed 3D-printed scaffolds have complex structures, the necessity of antimicrobial properties determination was met, revealing that although the produced PICN itself does not possess antimicrobial properties, it does not support the excessive growth of bacteria. However, this is an important parameter to avoid infections, and therefore future failure of the dental material. The application of silver nanoparticles embedded in bio-based lignin matrix (Ag@PL NPs) to the surface of PICN proved to be stable and confirmed the reduction in antimicrobial growth on the functionalized PICN.

For every new material for biomedical application, biocompatibility is another key parameter. In the present thesis, we approached different cell lines to study the cell viability of PICN cubic scaffolds, PICN cubic scaffolds functionalized with antibacterial nanoparticles, and flat zirconia discs (non-complex geometry) functionalized with a biocompatible coating based on polydopamine and acrylates. Either PICN scaffolds (without Ag@PL NPs) or the zirconia samples covered with the biocompatible film showed positive results in both, adhesion and proliferation studies, with MG-63 human osteoblasts. However, the presence of polydopamine units in the methacrylate coating generated by plasma polymerization seems to potentiate cell growth compared to Bis-GMA/TEGDMA copolymer-filled samples. Thus, future studies can drive more researchers to implement this new polymer (poly(EGDMA-co-DOMAm)) for infiltration of macroporous 3D-printed zirconia samples intended to be used in dentistry applications.

At the same time, the biocompatibility assay of 3D-printed PICN scaffolds with Ag@PL NPs showed that the viability of human cell lines was slightly reduced concerning the sample without nanoparticles, however, was much better for human keratinocyte cells in comparison with human fibroblasts. So, an indirect cell viability test would be recommended to ensure that Ag atoms have not been delivered to the media.

Overall, a new approach to PICN materials was introduced and successfully manufactured using fast-developing additive manufacturing technology. The new composite material was characterized in depth in the aspects of becoming a desired material for the dental industry. The produced PICN was further functionalized to overcome the challenges of biomedical devices and their failure.

The future aspects of utilization of such material lie in further improvement of the surface functionalization to improve the biocompatibility of the hybrid system. Another future goal could also include the exchange of filing materials and potential applications in different areas than the biomedical fields.